Complex molecules on surfaces: In-situ electrospray deposition and photoelectron spectroscopy



Robert H. Temperton

Supervisor: Dr James N. O'Shea

School of Physics

This dissertation is submitted for the degree of
Doctor of Philosophy

October 2017

Abstract

Furthering our understanding of next generation hight harvesting devices has the potential to revolutionise energy storage and production. This thesis discusses the use of surface science techniques, principally soft X-ray photoelectron spectroscopies, to study two types of molecular solar cell: dye sensitised solar cells and organic photovoltaic devices. Much of this work relies on electrospray deposition, which is becoming a well established technique allowing the in-situ deposition of fragile, non-volatile molecules in high vacuum environments. This thesis explores the potential use of electrospray deposition to build model photovoltaic devices, including bi-layer and bulk heterojucntion structures, to extend the use of the technique beyond the simple "molecule on a surface" type of experiment that have previously dominated the high-vacuum electrospray deposition literature.

Firstly this thesis presents the development of two instruments that aim to aid the characterisation of electrospray. A novel ultra-fast exposure microscopy system is presented that used a pulsed laser and purpose-designed cell containing a fluorescent dye to produce short (>20 ns) incoherent light pulses. Images of electrospray ionisation, highlighting the capabilities of the imaging system, are presented. Preliminary images showing the unusual behaviour when the liquid properties are severely changed by adding a high concentration of salt are also presented. We also include some proof-of-concept data, collected using a home-built image charge detection instrument, to measure velocity distributions of molecular ions that are landing on the surface. This instrument has led the way to a more refined image charge detection instrument that will be of great benefit to future studies.

A series of three experiments are presented that highlight the capability and suitability of high vacuum deposition to produce the types of structures used in molecular photovoltaic devices. Time of flight secondary ion mass spectrometry was used to image a bi-layer structure, produced using electrospray from two molecules dissolved in the same solvent, showing there is little mixing between the layers. These structures are challenging to make using processes like spin casting where solvent compatibility results in mixing of the films. Two electrospray sources

were used to co-deposit two molecules simultaneously from immiscible solvents, which is again not possible using standard techniques. Finally a complex polymer blend was deposited using electrospray, from a single solution, and analysed using X-ray photoelectron spectroscopy (XPS) finding evidence of preferential deposition of one species.

Bi-isonicotionic acid (the ligand of many popular organometallic photo-sensitisers) has been deposited onto Ag(111) in-situ via sublimation. X-ray photoelectron spectroscopy (XPS) and X-ray absorption spectroscopy (XAS) have been used to obtain chemical information and map out the density of states for the system. We find the LUMO (lowest unoccupied molecular orbital) lies below the Fermi level of the silver surface allowing ultra-fast bi-directional charge transfer between the molecule and surface. This was probed using resonant photoelectron spectroscopy (RPES) by observation of super-spectator and super-Auger decay mechanisms from the core excited state.

In the final experimental chapter, films of phenyl-C61-butyric acid methyl ester (PCBM) and Poly(3-hexylthiophene-2,5-diyl) (P3HT), common acceptor and donor molecules used in organic photovoltaic devices, were successfully deposited in-situ in UHV using electrospray deposition on the Au(111) surface. Bi-layer heterojunction and bulk heterojunction structures of the two molecules were also produced using electrospray. Again, XPS, XAS and RPES were used to investigate chemical interactions, map out the density of states for the molecular systems and probe charge transfer between the molecules and surfaces. For PCBM, some interesting chemical behaviour regarding an oxygen group on the ligand is observed. Measurements also show the LUMO of PCBM lies below the surface Fermi level, but surprisingly no evidence of super-spectator or super-Auger decay is found. RPES was unable to show evidence of charge transfer between the two molecules in a bi-layer heterojunction structure. Finally, careful ionisation potential calibration of XPS spectra were used to try and infer the position of the valence band maximum of the two molecules when brought together in a heterojunction.

List of Publications

Adsorption and charge transfer interactions of bi-isonicotinic acid on Ag(111). R. H. Temperton, A.J. Gibson, K. Handrup, J.N. O'Shea. *The Journal of Chemical Physics*, **147**, 054703 (2017)

On the suitability of high vacuum electrospray deposition for the fabrication of molecular electronic devices. R.H Temperton, J.N. O'Shea, D.J. Scurr. *Chemical Physics Letters*, **682**, 15-19 (2017).

Exploring ultra-fast charge transfer and vibronic coupling with N 1s RIXS maps of an aromatic molecule coupled to a semiconductor. J.N. O'Shea, K. Handrup, R. H. Temperton, A.J. Gibson, A. Nicolaou, N. Jaouen. *The Journal of Chemical Physics*, **147**, 134705 (2017).

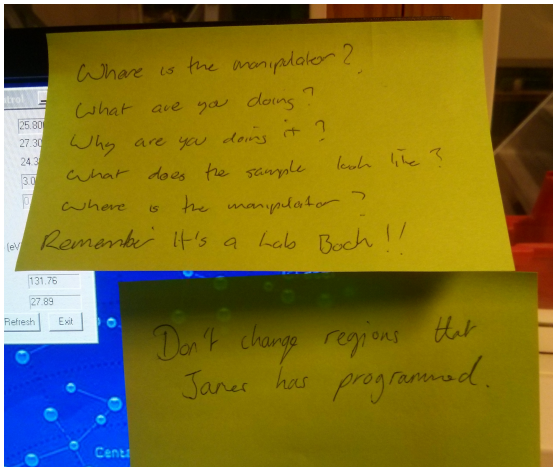
Resonant core spectroscopies of the charge transfer interactions between C60 and the surfaces of Au(111), Ag(111), Cu(111) and Pt(111). A.J. Gibson, R.H. Temperton, K. Handrup, J.N. O'Shea. *Surface Science*, **658**, 69-78 (2017).

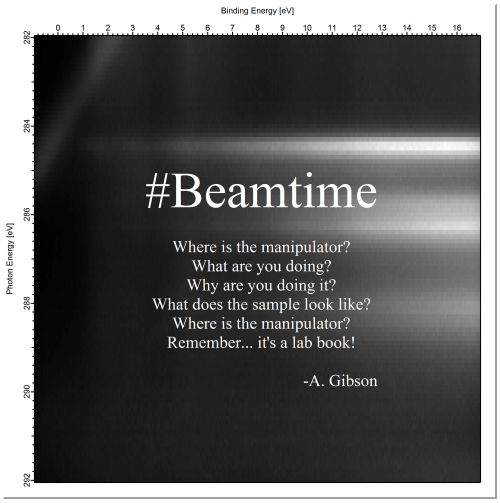
Electrospray deposition in vacuum as method to create functionally active protein immobilization on polymeric substrates. E. Fornari, C. J. Roberts, R. H Temperton, J. N. O'Shea. *Journal of colloid and interface science*, **453**, 252-259 (2015).

Charge transfer from an adsorbed ruthenium-based photosensitizer through an ultra-thin aluminium oxide layer and into a metallic substrate. A. J. Gibson, R. H. Temperton, K. Handrup, M. Weston, L. C. Mayor, J. N. O'Shea. *The Journal of Chemical Physics*, **140**, 234708 (2014).

Acknowledgements

Beamtime can be a stressful but incredibly rewarding process and without the help of James O'Shea (who is an incredible PhD supervisor), Andy Gibson and Karsten Handrup the process would not have been anywhere near as enjoyable or successful. I therefore owe a great deal of thanks to these colleagues and friends. Not to say that the weeks were not without their challenges. Below is a little memento from a beamtime at MaxLab i311. On a night shift, Andy and I were getting rather frustrated with the quality of the lab book that started producing a small series of well intended, but passive aggressive, post-it notes between shifts. The first of which was memorialised into artwork by James who presumably had reached the pinnacle of procrastination during a week plagued with beam-dumps.





I am also grateful for the long series of collaborators we have in Lund who have invited me to participate in their experiments and assisted with ours. I am convinced there is no better way to develop as a scientist then to attend beamtime with different people, so owe them a great deal of gratitude.

I was very fortunate for my research to be funded via Molecularspray Ltd. and the Engineering and Physical Sciences Research Council (EPSRC) through a DTG/CASE conversion studentship. Molecularspray are a spin-out company who have commercialised the type of portable electrospray deposition instrument used

in this study and it has been a absolute pleasure to work closely with them over the course of my PhD. I am also grateful for further funding from the University of Nottingham Interdisciplinary Centre for Analytical Science (UNICAS) who provided funding via a sandpit. It was an incredibly valuable experience to design a research proposal and be the principle investigator of a collaborate project. Thanks also need to go to Nottingham's Advanced Molecular Materials research priority area who funded my access the Kratos XPS facility in the Nottingham Nanoscale and Microscale Research Centre.

I would like to end by thanking the many people in Nottingham who I have worked with over the years. I have had support from so many members of academic staff, but special thanks to Mike Smith who was the driving force behind the ultra fast exposure speed video project and James Sharp who continued the work I left behind after completing my masters. My sincere gratitude goes to the amazing team of technical staff to whom basically every experimentalist in the building owes more thanks than they can possibly give. Particularly, to all the people in the mechanical and electrical workshops who have realised all my wacky experimental ideas over the years. These hugely talented people transform poorly thought through concepts, with briefs as vague as "I need a thing to bodge this thing", into precision engineered parts using challenging materials. You are all amazing and neither I nor any of my fellow experimentalists would be anywhere near as successfully without you.

List of abbreviations

- BE – Binding Energy
- CRM – Charge Residue Model (see Chapter 1.5.2)
- D1011 – A beamline at the Max II synchrotron (see Chapter 2.7.3)
- DSSC – Dye Sensitised Solar Cell (see Chapter 1.2)
- ESD – Electrospray Deposition
- HOMO – Highest Occupied Molecular Orbital
- I311 – A beamline at the Max II synchrotron (see Chapter 2.7.4)
- IEM – Ion Evaporation Model (see Chapter 1.5.2)
- IP – Ionisation Potential
- K-cell – Knudsen-cell
- KE – Kinetic Energy
- LUMO – Lowest Unoccupied Molecular Orbital
- MCP – Microchannel plate
- NEXAFS – Near Edge X-ray Absorption Spectroscopy
- OPV – Organic Photovoltaic device (see Chapter 1.3)
- RPES – Resonant Photoelectron Spectroscopy (see Chapter 2.2.5)
- ToF-SIMS – Time of Flight Secondary Ion Mass Spectrometry
- UHV - Ultra-High Vacuum
- XAS – X-ray Absorption Spectroscopy (see Chapter 2.2.4)
- XPS – X-ray Photoelectron Spectroscopy (see Chapter 2.2.1)

Table of contents

1 Low cost photovoltaics **1**

1.1 Introduction 1
1.2 Dye sensitised solar cells 3
1.3 Organic photovoltaics 6
1.4 Charge transfer in the photoexcited state 9
1.5 Electrospray ionisation 12
1.5.1 Taylor cone and jet formation 13
1.5.2 Molecular ion formation 14
1.6 Electrospray deposition 15
1.6.1 The electrospray/vacuum interface 16
1.6.2 Electrospray deposition instrumentation 18
1.6.3 Applications 19
1.7 Aims of this thesis 21

2 Experimental methods **22**

2.1 Vacuum methods 22
2.1.1 Surface cleaning 22
2.1.2 Traditional molecular deposition techniques 23
2.1.3 Electrospray deposition system 24
2.2 Photoemission spectroscopy 26
2.2.1 X-ray photoelectron spectroscopy 26
2.2.2 Surface sensitivity 32
2.2.3 Interpreting XPS spectra 33
2.2.4 X-ray absorption spectroscopy 37
2.2.5 Resonant photoelectron spectroscopy (RPES) 39
2.3 X-ray generation 42
2.3.1 X-ray anode 42
2.3.2 Synchrotron radiation 44
2.4 XPS data processing 49

2.4.1 Energy calibration . . . 49
2.4.2 Background subtraction . . . 51
2.4.3 Peak fitting . . . 52
2.4.4 Quantitative measurements . . . 52
2.5 XAS data processing . . . 53
2.5.1 Photon energy calibration . . . 53
2.5.2 Density of states . . . 53
2.5.3 The "Carbon Dip" . . . 54
2.6 RPES data processing . . . 54
2.7 Instruments/facilities used . . . 55
2.7.1 VESPA . . . 55
2.7.2 Kratos Axis Ultra . . . 55
2.7.3 MAX-Lab D1011 . . . 55
2.7.4 MAX-Lab I311 . . . 56

3 Instrument development for the characterisation of electrospray ionisation 58
3.1 Ultra-short exposure video capture of electrospray ionisation . . . 58
3.1.1 Introduction . . . 58
3.1.2 Instrument details . . . 60
3.1.3 Development . . . 60
3.1.4 Example images . . . 64
3.1.5 Discussion and conclusions . . . 65
3.2 Image charge detection . . . 68
3.2.1 Introduction . . . 68
3.2.2 Methods . . . 68
3.2.3 Velocity distributions . . . 72
3.2.4 Conclusions . . . 74

4 Suitability of electrospray deposition for the fabrication of molecular electronic devices 75
4.1 Introduction . . . 75
4.2 Instrumentation . . . 76
4.3 Methods, results and discussion . . . 77
4.3.1 Layered deposits of molecules from the same solvent . . . 77
4.3.2 Deposition of immiscible polymer blends . . . 78
4.3.3 Miscible polymer blends for organic photovoltaics . . . 80
4.4 Summary and conclusions . . . 83

5 Adsorption and charge transfer interactions of bi-isonicotinic acid on Ag(111) 84
5.1 Introduction . . . 84
5.2 Method . . . 85
5.3 Results and discussion . . . 89
5.4 Conclusions . . . 97
5.5 Acknowledgements . . . 98

6 Photoemisson of PCBM and P3HT deposited by electrospray 99
6.1 Introduction . . . 99
6.2 Methods . . . 101
6.2.1 Synchrotron experiments . . . 101
6.2.2 Lab-source experiments . . . 104
6.3 PCBM and C_{60} . . . 105
6.3.1 XPS . . . 105
6.3.2 Density of states . . . 109
6.3.3 Resonant photoemission . . . 112
6.4 P3HT . . . 118
6.4.1 XPS . . . 118
6.4.2 Density of states . . . 120
6.4.3 Resonant photoemission . . . 120
6.5 Bi-layer: P3HT on PCBM . . . 125
6.5.1 XPS . . . 125
6.5.2 Resonant photoemission . . . 129
6.6 Ionisation potential measurements . . . 131
6.6.1 Beam-damage . . . 131
6.6.2 Bi-layer . . . 132
6.6.3 Bulk heterojunctions . . . 132
6.6.4 Summary of results and Kraut's method . . . 134
6.7 Ex-situ samples . . . 137
6.8 Summary and conclusions . . . 139

7 Conclusions and future work 141

References 144

Appendix A Electrospray compatible solvents and solutes 158
A.1 Solvent information . . . 158
A.2 Solute information . . . 159

Chapter 1

Low cost photovoltaics

1.1 Introduction

The ability to harvest light to produce energy is regarded as a critical part of modern energy strategy in order to meet both energy demands and emission targets. The importance of photovoltaics in the gradual transition from fossil fuels to renewables is outlined in both European [1] and UK [2] energy roadmaps. The traditional approach to photovoltaics is to use a semiconductor that has a bandgap that falls within the visible spectrum, allowing light to excite an electron from the valence band of the semiconductor into the otherwise unoccupied conduction band. This separation of an electron/hole pair across the bandgap, and the intrinsic electric field in the depletion region, means that it is possible for the charges to leave the device, and do useful work in a circuit before recombining. This process is summarised in Figure 1.1.

Although semiconductor solar cells (along with other semiconductor technologies) have become commonplace, they are relatively expensive to produce - both in terms of the material processing and fabrication costs. And even given the decreasing cost of silicon solar cells, partly due to industrial experience from fabricating silicon based electronics, there is still a large motivation to be able to produce lower cost photovoltaics. Here we discuss two potential technologies that have the potential to meet this low-cost ambition by utilising more abundant materials that have lower processing costs and from which devices can be made using high throughput manufacturing techniques.

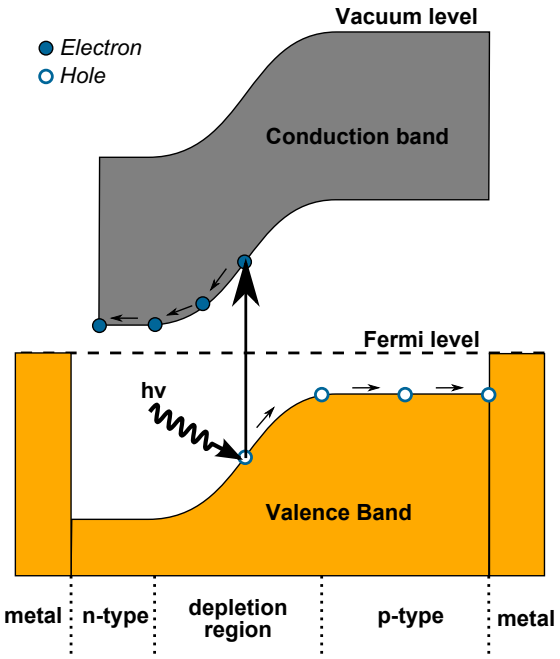


Figure 1.1: Simplified schematic showing the use of a p-n junction as a photovoltaic device. After a photoexcitation event, where an electron is taken from the valence band to the conduction band leaving a hole in the valence band, the intrinsic electric field in the depletion region makes it favourable for the charges to separate into the n and p type regions rather than recombine. A voltage is therefore created between the n and p regions and a current is able to flow if a load is applied between the metal contacts.

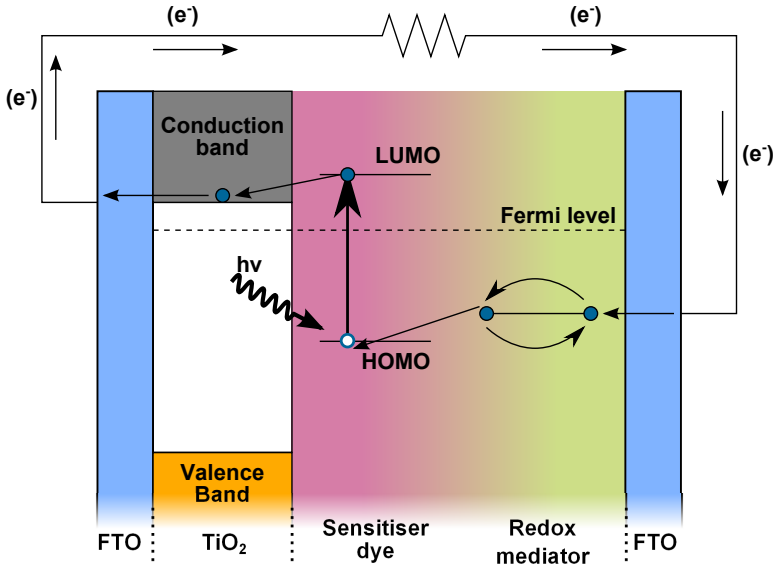
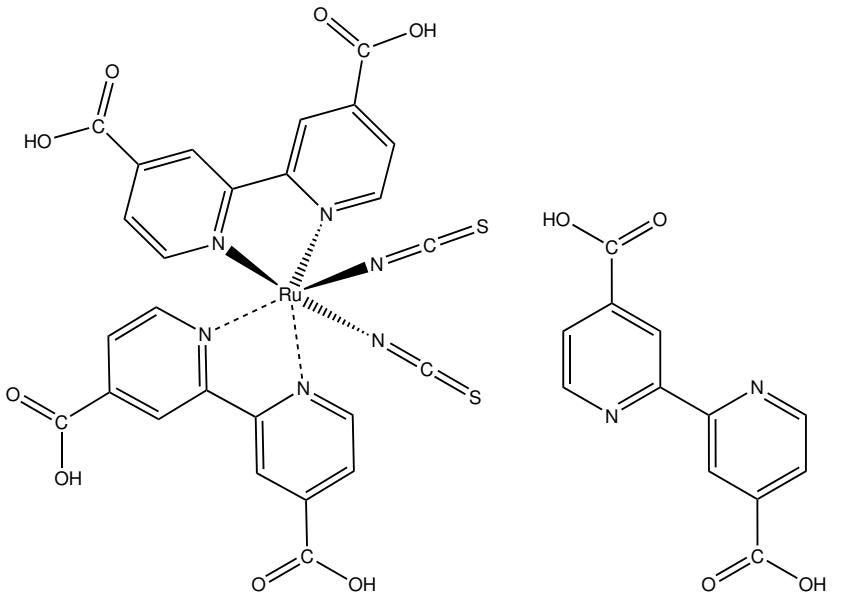


Figure 1.2: Schematic outlining the operating principle of a dye sensitised solar cell (DSSC). Photoexcitation of a dye molecule on the surface of the titanium dioxide allows the injection of an electron into the conduction band of the titanium dioxide. The core hole is filled via an electrochemical process whereby a redox mediator undergoes oxidation and reduction cycles allowing electrons to be transferred from the counter electrode to the dye. A voltage is created (limited by the energy difference between this redox process and the TiO_2 conduction band) allowing work to be done. The electrodes are made from a transparent conducting material, for example glass coated in fluorine doped tin oxide (FTO).

1.2 Dye sensitised solar cells

Dye sensitised solar cells (DSSC) are now a well established alternative to traditional semiconductor based devices. They rely on a wide band gap semiconductor, generally titanium dioxide (titania), that would require light outside of the visible spectrum in order to directly excite electrons from the valence to conduction bands. However, a dye that absorbs light in the visible spectrum (ie. if the gap between the highest occupied and lowest unoccupied molecular orbitals matches a visible wavelength of light) can be used to inject electrons into the conduction band of the titania if the dye's LUMO (lowest unoccupied molecular orbital) lies above the titania conduction band. The first DSSC devices based on this principle were fabricated by Brian O'Regan and Michael Grätzel in 1991 [3] and the operating principle of such a device, which is now also known as a Grätzel cell, is shown in Figure 1.2.

As shown, photons of visible light excite an electron from the dye's HOMO (highest occupied molecular orbital) to its LUMO taking the sensitiser dye (S)



(a) N3 **(b)** Bi-isonicotinic acid

Figure 1.3: (a) shows the "N3" dye sensitiser - Bis(isothiocyanato)bis(2,2'-bipyridyl-4,4'-dicarboxylato)ruthenium(II) - a metalorganic complex with a ruthenium center, two thiocyanate ligands and two bi-isonicotinic acid (shown in (b)) ligands

into an excited state (S^*). The electron now in the LUMO can then transfer to the titania leaving the sensitiser in an oxidised state (S^+). A redox mediator - typically a liquid electrolyte consisting of iodide and tri-iodide - facilitates regeneration of the dye by transporting electrons from the counter electrode:

$$S^+ + e^- \rightarrow S \tag{1.1}$$

The electrons required for this reduction process come from the oxidation of the I^- species by the dye molecule:

$$3I^- \rightarrow I_3^- + 2e^- \tag{1.2}$$

The I_3^- diffuses to the counter electrode where the above is reversed reducing the tri-iodide back into iodide that can continue round this cyclic process and regenerate more dye molecules:

$$I_3^- + 2e^- \rightarrow 3I^- \tag{1.3}$$

The most commonly used sensitisers are ruthenium based metal-organic complexes such as the famous "N3" dye (also known as Ru-535) introduced in Grätzel's

original 1991 paper [3]. The structure of N3 is shown in Figure 1.3a. It has a ruthenium centre atom with two bi-isonicotinic acid (Figure 1.3b) and two thiocyanate ligands. On TiO_2, N3 has been shown to bond to the surface via both a carboxylic acid group of the bi-isonicotinic acid ligands and the sulphur atoms that terminate the thiocyanate [4]. These experiments were later repeated on gold, where only the thiocyanate bonded with the surface [5], and aluminium oxide where only the carboxylic group is involved in the bonding [6]. These experiments were made possible by electrospray deposition (discussed in Chapter 1.5) as the molecule is too large/fragile to be deposited in-situ in a vacuum chamber using traditional evaporation based techniques.

Prior to these experiments, there was a great deal of work carried out on the smaller and simpler bi-isonicotinic acid ligand which can be sublimed in UHV. These studies have examined how the molecule bonds to the titanium dioxide surface for both the rutile crystals [7, 8] and anatase nanoparticles [9] (which is a more accurate model of the real devices). Other studies have looked at the charge transfer dynamics between the molecules and the rutile surface and measured super fast transfer times of sub 3 fs [10]. Similar measurements have been carried out on the Au(111) surface, where the carboxylic acid groups do not deprotonate and bond to the surface (as is the case on on titania), where the authors do not observe this super fast charge transfer from LUMO states of the molecule to the metal [11].

There is a whole zoo of dyes that can be used for the purpose of a sensitiser in a DSSC, but the vast majority of the most efficient dye sensitisers that are commercially available from companies like DyeSol and Solaronix are based on the N3 molecule. These include N719, referred to as "the industry standard dye" which is sold as being more soluble than N3 and capable of producing larger cell voltages, and N795 "black dye" which has a wider absorption range. Less efficient options on the market include purely organic dye molecules, such as SQ2 and RK1, which have the obvious potential advantage of being low cost due to the absence of rare earth elements. The research community have also been trying to strike a compromise between efficiency and cost by maintaining metal centred complexes but using more abundant elements like copper [12] or iron [13, 14].

Despite variations in dye technology, the efficiency of the sensitiser is not considered the limiting factor in terms of mass adoption of the technology. The greatest challenge is the liquid electrolyte which has a tendency to leak out of devices over the desirable lifetime of solar cell devices. This has resulted in researchers attempting to replace the electrolyte with non-liquid alternatives, such as polymers [15], or non-volatile ionic liquids [16].

Although interest in DSSC's for commercial energy production seems to be decreasing, DSSC technology has the potential to be applied elsewhere such as for photocatalytic water splitting where similar molecules can be used [17]. There is therefore still a great deal of value in understanding the interactions between these molecules and surfaces, especially in the photoexcited state.

1.3 Organic photovoltaics

An alternative type of solar cell device that possesses many of the same desirable characteristics as dye sensitised solar cells (cheap, flexible substrates, mass production compatible) are organic photovoltaic (OPV) devices. A typical design and operation of an OPV device is outlined in the diagrams in Figure 1.4. The most efficient devices utilise the interface between electron acceptor and electron donor molecules mixed together to form a structure known as a bulk heterojunction. The two approaches to making these types of structure, where the two species are either co-deposited or mixed together in a single solution prior to deposition, were pioneered in 1990 [18] and 1995 [19] respectively. Prior to these bulk-hertojunctions, single heterojunction devices, i.e. bi-layer structures, were the norm. The landmark single heterojunction device, achieving 1 % efficiency was reported in 1986 [20].

Like DSSCs (Section 1.2), OPVs are a type of excitonic solar cell where a photon is absorbed creating a strongly bound electron hole pair. In an OPV, this exciton is created in the electron donor (step 1 in Figure 1.4a) and needs to diffuse to the interface between the accepter and donor molecules (step 2) in order for the electron and hole to separate. The electron can then travel through the acceptor molecules to the cathode and the hole via the donor molecules to the anode [21]. With DSSC's, the devices rely on efficient charge transfer between the dye and the semiconductor in order to avoid recombination of the exciton. In an OPV, the challenge is to have efficient diffusion to the donor/acceptor interface as this is the only place charge separation can occur, so it is intuitive as to why a well designed bulk heterojunction maximises this electron/hole dissociation. It is now established that the ideal bulk heterojunction has sharp interfaces, a good balance between small domain sizes matching the diffusion length of the exciton, typically considered about 10 nm, but also providing a continuous path through the network of molecules to the respective electrodes [22]. An excellent discussion of the morphologies of heterojunctions can be found in the recent review by Hedley et al. [23].

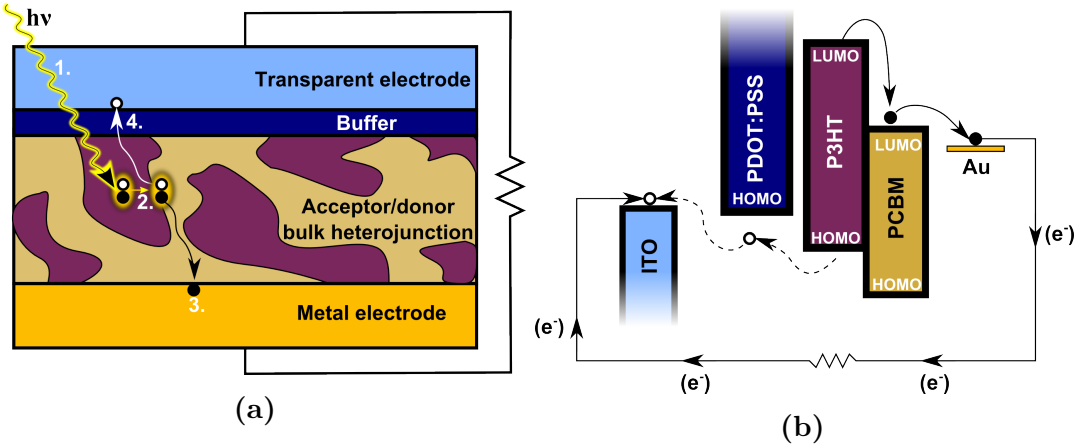
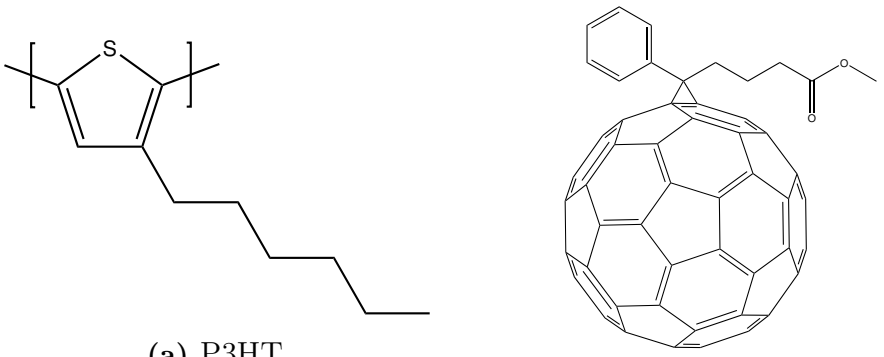


Figure 1.4: (a) A cartoon showing the structure of a basic bulk heterojunction organic photovoltaic device. The bulk heterojunction is a blend of an electron acceptor and electron donor (commonly PCBM and PCBM shown in figure 1.5). The buffer layer is typically the polymer blend PEDOT:PSS (shown in Figure 1.6). Electrodes are commonly made from indium doped tin oxide and gold. (b) shows the approximate energy alignment of these common materials. The device works by photoexcitation of the donor molecule creating an exciton that diffuses to the donor/acceptor interface where the electron and hole separate.

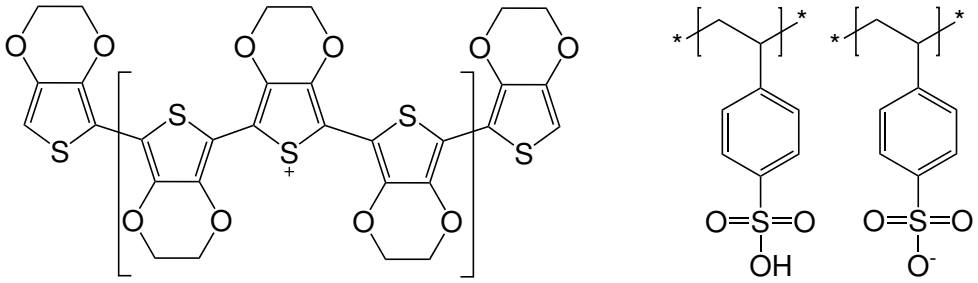
The exciton dissociation process itself and the charge transfer across the accepter/donor interface is still not well understood. The simple series of processes described here, as well as in a lot of the literature, is now known to be an oversimplification as there are various other mechanisms potentially at play. For example, it has been shown for a different molecular system [24] that rather than direct electron transfer from the donor to the acceptor, energy can be transferred creating an exciton in the acceptor. This in turn can be followed by a hole transferring from the acceptor into the donor creating the same final state as the direct electron charge transfer mechanism. However for the purposes of this study, the simple picture presented is sufficient. For an overview of some of the other complications we refer the reader to Kippelen and Brédas' review article [25] which covers this topic.

There is a wide array of electron acceptors and donors that can be used in OPVs [26–28]. For the types of device discussed here, that is a hole conducting polymer with a fullerene electron acceptor, P3HT and PCBM, both are shown in Figure 1.5, are two of the most studied [29]. PCBM has comparable properties to C_{60} but its functional group improves its solubility and its band structure places its LUMO at a higher energy. The LUMO position is important as the energy gap between the donor HOMO and acceptor LUMO (E_g) has been experimentally



(a) P3HT **(b)** PCBM

Figure 1.5: Structure of the common electron donor and acceptor molecules (b) Poly(3-hexylthiophene-2,5-diyl) (P3HT) and (a) Phenyl-C61-butyric acid methyl ester (PCBM) used in organic photovoltaic devices.



(a) PEDOT **(b)** PSS

Figure 1.6: The conductive polymer blend PEDOT:PSS used as a buffer layer in OPV devices. (a)PEDOT - poly(3,4-ethylenedioxythiophene. (b)The co-polymer PSS - polystyrene sulfonate.

shown to determine the open circuit voltage ($eV_{OC} = E_g - 0.3eV$), using PCBM, or other functionalised fullerenes, rather than C_{60} allows for more efficient devices. The solubility is an important parameter as bulk heterojunctions are now generally made by dissolving them in the same solution (chlorobenzene being a common choice) and depositing via spin casting or other solution based techniques.

As well as the heterojunction, it is common to include a hole transport "buffer layer" on the anode of the device. This is commonly a p-type polymer blend called PEDOT:PSS as shown in Figure 1.6 that provides better energy level alignment between the hole conducting layer and the anode, acts to blocks electrons and smooths the anode surface [30]. Although not shown in the diagram here, some researchers also include an equivalent n-type transport layer on the cathode [31]. Further complexities to the devices are possible to improve the efficiency, such as the inclusion of a layer of pure polymer between the buffer and the bulk heterojunction [32].

1.4 Charge transfer in the photoexcited state

As the heart of molecule based photovoltaic devices relies on the movement of photoexcited electrons between a molecule and a surface, previous studies have attempted to probe the charge transfer dynamics using resonant photoemission spectroscopy, discussed in Chapter 2.2.5, of simplified/model systems in order to gain insight into the operation of real devices. Example experiments studying some of the key molecules discussed above include C_{60} [33, 34], bi-isonicotinic acid [9–11, 35], as well as N3 [4, 36, 6] and related dyes for water splitting [37–39]. Resonant photoemission involves the photoexcitation of an electron from an occupied level into a LUMO state (much like the photoexcited state in DSSC's where a photon excites an electron from the HOMO to the LUMO) allowing the electron to charge transfer to the surface. These studies generally involve comparison of model systems of both monolayer and multilayer films of molecules on their associated surface. For the monolayer case, all the molecules probed allow electron transfer between the molecule and surface. The high surface sensitivity of electron photoemission means that multilayer films represent the bulk molecule where the influence of the surface is removed.

These type of measurements rely on inferring charge transfer behaviour that occurs whilst the molecule is in its core excited state by examining the decay mechanisms that follow. Interpreting the measurements therefore relies on having an understanding of what the various decay options are. The available decay mechanisms are outlined in Figure 1.7 for an example molecule whose LUMO lies below the Fermi level of a metal surface, so charge transfer between the molecule's LUMO and the occupied valence structure of the metal is possible. The example shows the resonant excitation of an electron from a core level in the molecule (such as carbon, nitrogen etc.) that does not feature in the substrate. If we were to excite, for example, from the valence structure/HOMOs where both the surface and molecules have several overlapping states, both the molecule and surface could contribute making the interpretation much more difficult.

The first process shown in the top left of Figure 1.7, describes the resonant excitation process creating a core hole and a photoexcited electron in a LUMO state. Following the arrow to the right shows the various charge transfer options available to this photoexcited system and the downwards arrows highlight the decay options from the various states. As shown, it is possible for the molecule to relax directly via either the participator or spectator mechanisms without any charge transfer happening. In the case of the participator channel, the photoexcited electron participates in an Auger like decay process; whereas for

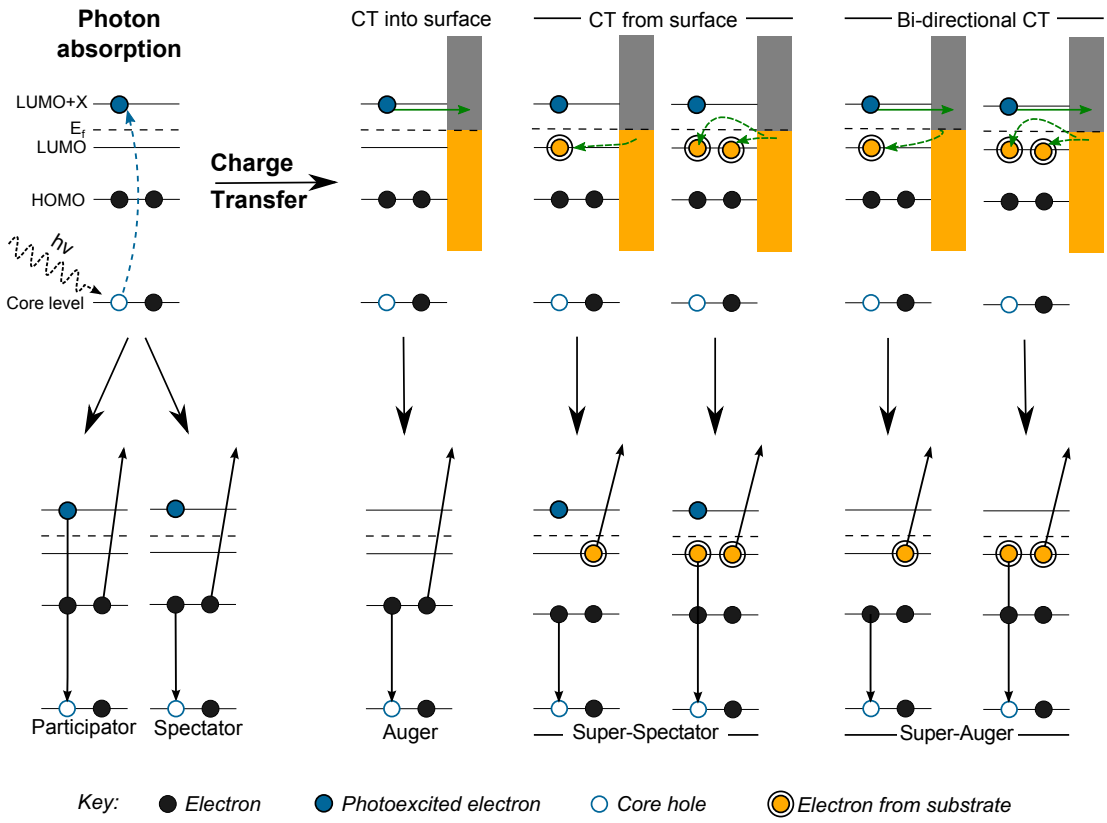


Figure 1.7: The various charge transfer (CT) options and resulting decay mechanisms of a molecule on a surface that has undergone photoexcitation. The excited state can decay without charge transfer via participator or spectator mechanisms. If the photoexcited electron charge transfers into the surface, the molecule can relax via Auger decay. If the LUMO lies below the Fermi level of the surface (E_f), electrons can charge transfer from the surface to the molecule opening the Super-Spectator decay channel. Super-Auger decay can occur when electrons can transfer in both directions.

spectator decay, the photoexcited electrons sits in the unoccupied level for the duration of the core-hole lifetime, whilst electrons from other orbitals undergo the decay mechanism. It is worth noting that for all these Auger-like mechanisms, the role of the electrons can be reversed with no change in the observable electron state. For the example of participator decay it is equally valid for the photo-excited electron to be emitted as it is for it to transition down to fill the core hole (the option shown in the figure).

The other possible decay paths occur when we either get charge transfer - either from the molecule to the surface, from the surface to the molecule, or bi-directional charge transfer in both directions - within the core hole lifetime. In the first case, where the photoexcited electron tunnels from the molecule into the surface, the resulting decay mechanism is normal Auger decay. In the second case, where one or more electrons from the surface transfer to the otherwise unoccupied states of the molecule, the relaxation process is now known as "super-spectator" decay [35]. This is where these electrons originally from the surface participate in the Auger like process whilst the photoexcited electron stays in its state and spectates the process. Finally, if charge transfer happens in both directions (ie the electrons from the surface transfer into the LUMO and the photoexcited electron tunnels into the surface during the lifetime of the core hole) we get "super-Auger" decay [34]. This mechanism is identical to a normal Auger process but involving the electrons originally from the surface.

The objective, using resonant photoemission, is to be able to distinguish the products of the decay mechanisms. For example, taking a simple system where charge transfer only happens in the molecule to surface direction, it is possible to compare the strength/intensity of the participator decay channel, the "no charge transfer" case, with the normal Auger decay channel (resulting from charge transfer). This ratio, along with the known core hole lifetimes and the ability to compare the monolayer and multilayer films (where molecules are isolated from the surface so no charge transfer is possible), allows this so called "core-hole clock" method [40] to be applied to calculate charge transfer times.

1.5 Electrospray ionisation

Understanding how the devices discussed in Sections 1.2 and 1.3 operate is fundamentally a surface science problem, as at their heart, they rely on the chemical and physical interactions between complex molecules and a surface. Gaining insight into the bonding, morphology and charge transfer is therefore critical to the development and optimisation of the devices. Historically, much of this work has been done with model systems for a number of reasons. The nature of surface science experiments lend themselves to starting with simple systems and slowly building complexity - an approach critical to interpreting the data. Secondly, many of these experiments are done in ultra-high vacuum and depositing larger more complex species onto surfaces in-situ is an experimental challenge. The latter can be addressed using electrospray deposition - one of the techniques helping bridge the disconnect between fundamental surface science and molecular engineering.

At the heart of this technique is a process called electrospray ionisation. This is a mechanism whereby a large electric field is used to create a stream of small, charged droplets from a liquid solution. Generally, several kilovolts are applied between liquid exiting a small capillary tube and a target (such as a sample, an inlet to an instrument, an electron-optics component or some other counter electrode). The physics underpinning electrospray stems from a theoretical study by Rayleigh who examined the physics of charged isolated droplets [41]. He predicted that, at a critical voltage, drops will fission as the electrostatic forces overcome the surface tension of the liquid. Zeleny continued this work and over a series of three papers [42–44] discusses what we now refer to as electrospray ionisation. Zeleny's apparatus is very comparable to modern day electrospray systems and throughout his papers he makes key observations, such as multi-jet modes, and acquires some stunning images of the process that are very impressive even when compared to modern studies.

Early work using electrospray ionisation to produce a beam of molecular ions was published in 1968 by Dole et al. [45] but it wasn't until 1988-1989 that Fenn et al. definitively showed, using mass spectroscopy, that electrospray was in fact producing intact gas phase molecular ions and the molecules were not breaking apart during the process [46]. There are several excellent review articles covering the mechanism of electrospray ionisation [47, 48] but the basic mechanism is outlined below in the context of the simple set-up shown in Figure 1.8. This shows a liquid passing through through an emitter capillary (made of an electrically

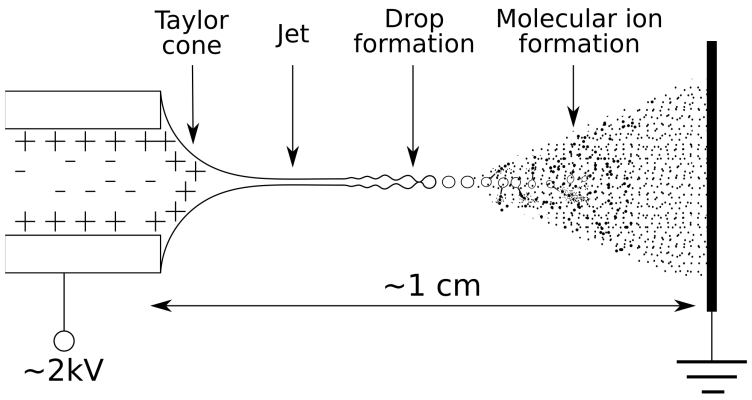


Figure 1.8: A typical electrospray ionisation experiment. Liquid passes through a metal capillary tube that is positioned ∼1 cm away from a counter electrode. A few kilovolts is applied between the two causing the liquid to form a Taylor cone, break off into a jet and a stream of droplets.

conducting material) that has a large voltage (∼2 kV) applied to it with respect to a grounded counter electrode ∼1 cm away from the exit of the capillary.

1.5.1 Taylor cone and jet formation

The first stage of the process describes the formation of an aerosol of small liquid droplets from liquid exiting the emitter capillary. The electric field resulting from the, in this case, positive bias on the emitter causes the solvent to become polarised with a build up of positive charge at the liquid meniscus. The same physics applies equally with a negative bias and negative charges. The two dominant forces on the liquid are due to surface tension, acting to pull the liquid back inside the capillary to minimise surface area, and electrostatic forces acting to pull the charged liquid towards the counter electrode. These two forces balance at all points at the surface of the liquid forming a range of geometries at different field strengths. At lower voltages, the liquid is pulled into a rounded/elliptical shape by the electric field. Above a threshold voltage, the meniscus suddenly forms a Taylor cone. This geometry has a fixed semi-vertical angle of 49.3° and was originally calculated by Taylor in 1964 [49].

The Taylor cone is an inherently unstable shape; as the tip at the apex of the cone tends towards being infinitely sharp, the field at the tip would tend towards a singularity. As the field strength is increased, it is therefore energetically favourable for a jet of highly charged liquid to be expelled from the tip of the Taylor cone. As the surface of the jet has an excess of charged ions compared to the bulk, repulsion of charges makes it favourable for the jet to pinch off into a

series of droplets. These have been shown to be charged close to the theoretical Rayleigh limit [50], describing the maximum possible charge that a droplet can have before fissioning, that is given by

$$Q = 8\pi\sqrt{\epsilon\gamma R^3} \tag{1.4}$$

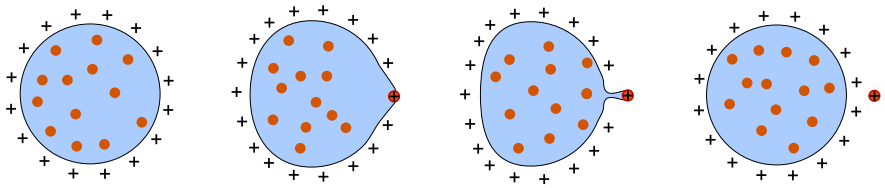
where Q is upper charge limit of a drop of radius R [41]. ϵ and γ are the electrical permittivity and surface tension of the liquid respectively. This expression shows that for a given amount of liquid, multiple smaller drops is a more stable system than one large drop - a principle fundamental to transforming charged droplets into molecular ions.

1.5.2 Molecular ion formation

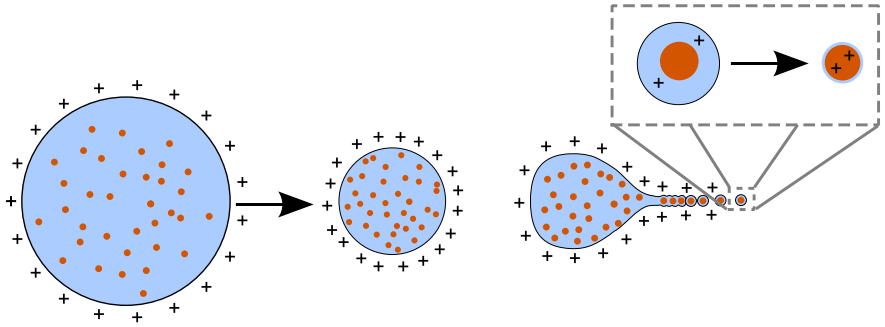
There are two proposed main mechanisms for the formation of gas phase molecular ions from the relatively large droplets: the ion evaporation model (IEM) and charged residue model (CRM) both of which are outlined in Figure 1.9 and are well discussed in several excellent review articles [47, 48, 51]. IEM is a mechanism originally introduced, in the context of drops produced from spray atomisers, by Iribarne and Thomson [52, 53] in the 1970s. In the context of electrospray, IEM is generally applicable to low molecular weight ions and works on the principle that for small droplets, $R \sim 10$ nm, the electric field at the surface of the drop (charged near the Rayleigh limit) is large enough for it to be energetically favourable for the ejection of a small ion from the surface [48].

The alternative model now known as CRM, which has its origin in Dole's papers on molecular beams of macroions [45, 54], is is generally applied to larger molecules ($\sim$1000 Da [48]) and relies on the repeated breakup of larger droplets until each progeny drop contains only a single analyte molecule. Droplet breakup occurs via the electrospray process: solvent evaporation causes the drop to shrink increasing the charge on the surface, and as the drop approached the Rayleigh limit, Taylor cone emission ejects charged liquid from the parent drop. CRM states that after several cycles of this process, the solvent from of the final droplet (containing a single molecule) evaporates producing analyte ions in the gas phase.

One further mechanism, called the Chain Ejection Model (CEM) [51], discusses the production of gas phase ions of long chain molecules, such as unfolded proteins rather than the globular analytes that CRM generally describes. CRM poorly describes the electrospray ionisation of long chain non-globular molecules, for which it has been shown the ions have a much larger and wider distribution of charge than CRM would predict [55]. For the case of a protein unfolding



(a) IEM - Ion Evaporation Model



(b) CRM - Charge Residue Model

Figure 1.9: Two mechanisms for the production of molecular ions from charge droplets containing a solution of the molecules.

in solution, the properties of the molecule change to being more hydrophobic meaning the protein chain migrates to the surface of the drop. CEM proposes a model similar to IEM where the chain is expelled from the parent droplet that is near the Rayleigh limit - initially the end of a chain is ejected and the rest of the chain follows in a stepwise motion until the entire chain is liberated from the drop.

It is worth noting that these models are far from accepted as the definitive mechanisms at play. There is a lot of debate, particularly around CRM and Dole's early claims [56, 57] but the consensus is as described above. Consideration of these models provides the best insight we have as to how gas phase molecular ions are produced.

1.6 Electrospray deposition

Electrospray ionisation found its first mainstream application as a mass spectrometry source that allowed the measurement of analytes, such as biological molecules [46], that are not volatile or thermally stable enough to survive traditional evaporation/sublimation techniques. A further benefit of electrospray mass spectrometry is it can allow chemical analysis of species whilst in solution [58]. However a more recent application is the use of electrospray as both an ambient and an ultra high vacuum compatible deposition source. Its use as an

ambient source can be trivial - simply use a substrate of your choice as the counter electrode. Vacuum deposition is slightly more sophisticated, relying on similar instrumentation to mass spectroscopy applications, where a series of differentially pumped chambers reduces the pressure from atmospheric conditions to the desired high vacuum environments.

The motivation to use electrospray ion beam deposition, rather than traditional surface science techniques (see Chapter 2.1.2), is that most traditional techniques required to take molecules from the solid or liquid to the gas phases rely on thermal evaporation or sublimation - for large molecules this can be a problem. For small molecules a partial pressure of the molecule in the gas phase can be achieved by gently heating the liquid/solid. The larger the molecule the higher the temperature required for sublimation/evaporation tends to be. As the chemistry of the molecules become more complex and the size increases further, increasing the temperature of the molecule causes it to damage (break apart) long before one has reached the required energies to get them in the gas phase.

1.6.1 The electrospray/vacuum interface

The general approach is to use a narrow (< 0.5 mm inner diameter) and long (typically about 5 cm) capillary tube to transfer the ions into a vacuum chamber. A capillary is used in order to minimises the amount of gas leaking into the chamber whilst still allowing the ions to pass through reducing the amount of pumping required to achieve a reasonable pressure in the chamber. Although the norm is to use a standard capillary tube, more efficient designs exist. By using a funnel type geometry rather than the standard pinhole on the inlet of the capillary, up to 100 % transmission into the vacuum system can be achieved [59].

Regardless of the capillary design, the pressure gradient across the inlet is large and the fluid dynamics at this atmosphere/vacuum interface is critical to the operation of vacuum electrospray instruments. As the gas/ions leave the inlet and enter the first vacuum stage, they undergo free-jet expansion. The physics of free jet expansion is explained well elsewhere [60], but the important principle in this context is that if the pressure difference across the exit of the capillary is high enough, the gas/ions undergo expansion where they are accelerated to the speed of sound (Mach number, M=1) at the capillary exit and supersonic speeds (M>1) downstream of this point. There is a transition point, known as the "quitting surface", beyond which the gas has expanded to the point the particles no longer undergo collisions due to the rapidly increasing speed and decreasing density.

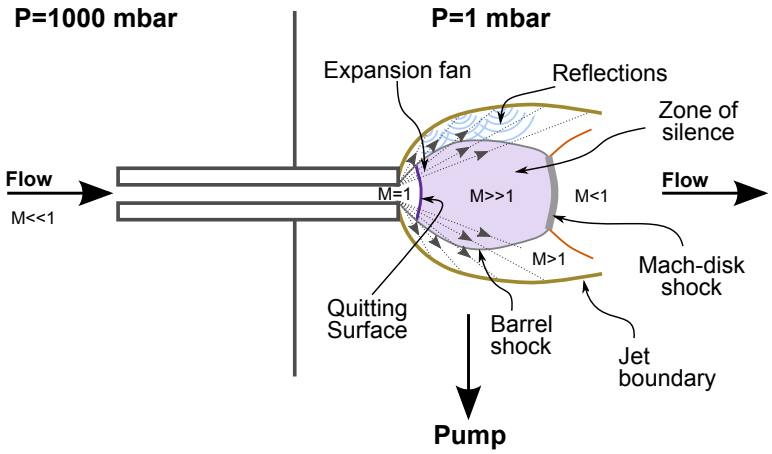


Figure 1.10: The free jet expansion process that occurs at the vacuum interface. Shown is an inlet capillary with a pressure gradient of ∼1 bar across it. Key phenomena are marked including shock boundaries that form the "zone of silence" (shown in purple) where the molecular ions are sampled.

Supersonic flow has the characteristic that it is not "aware" of downstream boundary conditions (the information cannot propagate faster than sound) but they are still there and the flow must adjust accordingly. The resulting phenomenon is the formation of shock waves (regions of high pressure and temperature) such as the so called "Mach disk". The position of Mach disk from the capillary exit can be estimated as it is a function of the capillary diameter (d) and the pressure ratio across the capillary:

$$x \approx 0.67 d \sqrt{\frac{P_{ambient}}{P_{vacuum}}} \tag{1.5}$$

At the capillary exit, expanding gas forms a series of waves which fan outwards, reflecting off the jet boundary and causing re-compression of the gas which creates "barrel shock". The area inside these shock boundaries and beyond the "quitting surface" is known as the "zone of silence" as the fluid here is not aware of any external influences. Here the expansion means the particles are flowing in a direction so particle collisions are least probable - i.e. the behaviour is like a molecular beam rather than a typical gas. It is therefore in the "zone of silence" we want to sample the ions. This is typically done using a skimmer cone (rather than an aperture) so that turbulence and other undesirable flows are minimised. It is worth noting the presence of a skimmer cone can modify the geometry of the mach disk [61].

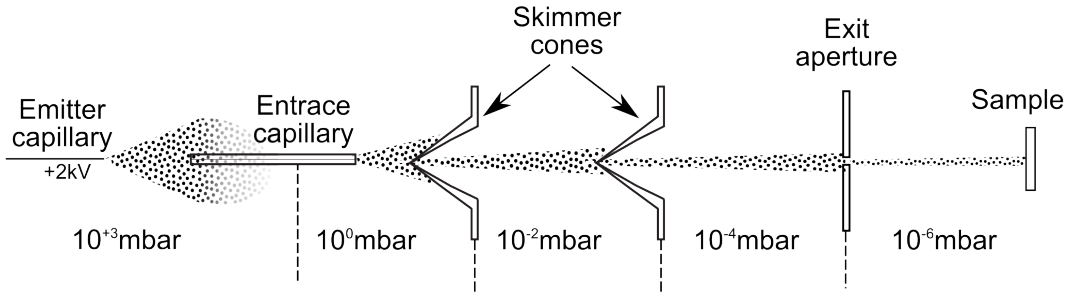


Figure 1.11: A typical basic electrospray deposition source showing the key components and approximate pressures.

1.6.2 Electrospray deposition instrumentation

The approach used in this thesis is that of a small portable deposition source (now commercially available from Molecularspray Ltd.) used previously by O'Shea et al. for a wide range of spectroscopy and microscopy studies - some of which are discussed below in Section 1.6.3. The specific instrument details are discussed in Chapter 2.1.3 but the basic principle is outlined in Figure 1.11. Liquid is passed through a stainless steel emitter capillary, generally floated at $\sim \pm 2$ kV relative to the inlet to the system that is $\sim$1 cm away. This inlet (forming the atmosphere/vacuum interface) is a stainless steel inlet capillary followed by three differentially pumped vacuum stages separated by skimmer cones. The instrument is low cost, small and portable - designed to be moved between instruments and facilities - so is particularly suited to synchrotron work.

Whilst portable and low-cost, this approach is somewhat more restrictive in its functionality when compared to many electrospray deposition instruments that have been developed. Details about these electrospray sources can be found in references [62–64], all of which incorporate ion optics in order to manipulate the molecular ion beam.

Ion funnel

The downside of using a skimmer cone to sample the expanding jet is the low throughput caused by the small solid angle that is sampled. A more sophisticated approach to creating a beam of molecular ions, using the entire throughput of an inlet-capillary, is an ion funnel [65]. These devices utilise an extensive series of electron optics controlled using an RF signal to collimate the ions in the jet. They have been incorporated into multiple electrospray deposition systems [63, 64].

Ion lenses

It is possible to use electrostatic lenses to focus the molecular beam to, for example, minimise losses through differential pumping apertures or to collimate the beam after manipulation by other ion optics components. A common lens design is the Einzel lens (also known as a unipotential lens) [66]. It is worth noting that this sort of lens can not be used in the first pumping stage to collimate the ion beam, as the high voltages that would be require much lower pressures (hence the need for sophisticated optics like ion funnels)

Mass selection

The most common addition to electrospray deposition sources is the use of mass selection in order to be able to control exactly what is landing on the surface. Utilising the fact that electrospray ionisation produces charged species, mass selection is typically done using one or more quadrupole mass filters [67] (as is commonly used in mass spectrometry). In addition to mass filtering, Rauschenbach et al. have coupled their source to a time of flight mass spectrometer to allow precise quantification of the species after mass filtering, so that is is known what is landing on the surface [62].

Neutral separation

It seems to be widely accepted, although not properly discussed in the literature, that electrospray ionisation can produce "neutral" species. These species have very high m/z values so are unable to be filtered out using conventional mass selection ion optics alone - instead a corner or bend is used where ion optics are used to deflect the desirable charged species away from the neutral component. This can be achieved using an electrostatic quadrupole to create a 90° corner [63, 64].

1.6.3 Applications

High vacuum electrospray deposition has been used to study a vast array of molecular systems. Some of this key literature is listed below.

Dye Sensitisers

The motivation of the O'Shea group to develop their electrospray instrument was to be able to study the "N3" dye, the benchmark sensitiser used in dye sensitised solar cells, deposited in-situ on rutile titanium dioxide. This ambition was realised in 2008 [4] where soft x-ray synchrotron radiation was used to probe occupied

and unoccupied states showing how the molecule bonded to the surface and gave insight into the charge transfer dynamics. Since then, N3 dye has become one of the most extensively electrosprayed molecules for UHV measurement. Scanning tunnelling microscopy and spectroscopy have also been used to study it on the anatase surface [68]. On Au(111), studies have examined the absorption of the molecule where N3 has been shown to not bond via the carboxylic oxygen atoms but only by the sulphur in the thiocyanate ligands [5]. Further experiments probing the charge transfer have been carried out showing ultra-fast charge transfer only occurs from the molecule into the surface and not in the other direction [36]. Finally, ultra-thin films of aluminium oxide have been grown on NiAl(110) where the bonding and charge transfer has been studied [6].

Electrospray has also been used to study related ruthenium centred metal-organic dyes designed for photocatalytic water splitting [37, 39, 38, 69] as well as other dye molecules relevant to photovoltaics, such as zinc protoporphyrins [70].

Nanoparticles

Early electrospray deposition experiments focussed on fullerenes [71] and nanotubes [72]. Electrospray has since facilitated the in-situ characterisation of a number of nanoparticles on surfaces including clusters [62], nano-rings [73–77] and single molecule magnets [78–81].

Polymers

As well as polymeric rings, electrospray has also allowed the deposition of a wide range of polymers in vacuum ranging from simple chains like poly(ethylene) oxide [82] to more complex system such including systems including porphyrin polymer chains [83] and blends of the conducting polymer P3HT with the fullerene PCBM (see Section 1.3) [84].

Biological molecules

High vacuum electrospray deposition has opened up the plethora of surface science techniques to biological systems, such as peptides [85], by facilitating in-situ deposition of such complex species in vacuum. An example of this is the use of scanning tunnelling microscopy to study proteins. When coupled with electrospray, not only does this allow imaging of individual proteins in different conformations [86, 87], but it also allows control of the deposited conformations via variation of the deposition energy [88]. Further to this, we have shown that proteins deposited onto surfaces in UHV via electrospray retain their biological activity [89].

High energy chemistry

Because electrospray produces ionised species that can be manipulated with ion optics, it is possible to accelerate the ions into the surface. Scanning tunnelling microscopy and spectroscopy have been used to show that N3 dye does indeed remain intact, when deposited onto Au(111), at energies lower than 2.5 eV; as the energy approaches ∼7 eV it has been shown to fragment [90]. For simpler molecules that are less prone to fragmentation however, this trick can be used to carry out chemical reactions on surfaces, at room temperature, that are not possible using traditional in-situ deposition techniques due to the high energies required. For example, graphene has been functionalised with azopyridyl species by colliding azopyridinium ions onto the surface at high energy [91].

1.7 Aims of this thesis

This thesis attempts to investigate complex molecular systems that are relevant to light harvesting using X-ray spectroscopies and electrospray deposition. Firstly, the key experimental methods are outlined included discussion of instrumentation and some background into the spectroscopic techniques used. The thesis goes onto investigate a couple of techniques that were developed to aid the further development and characterisation of electrospray. Specifically, using high speed imaging to gain an insight into the electrospray ionisation mechanism and image charge detection to obtain velocity and charge distributions of the molecular ions. This leads onto a study addressing whether electrospray deposition is a suitable technique for building model systems for studying organic photovoltaics - specifically using it to build bi-layer structures and blends. This has been published in journal Chemical Physics Letters [92]. A surface science experiment, using a traditional sublimation based deposition technique, is then presented investigating the bonding and charge transfer of bi-isonicotinic acid with the Ag(111) surface - this chapter has been published in the Journal of Chemical Physics [93]. Finally this thesis presents a thorough soft-X-ray synchrotron study examining PCBM and P3HT layers, bi-layers, and bulk heterojunctions on Au(111). This chapter uses electrospray to construct these structures, in-situ in UHV, and aims to probe bonding and charge transfer between two molecules and with the gold surface.

Chapter 2

Experimental methods

2.1 Vacuum methods

Many of the studies presented here require the use of high vacuum environments. There are two key reasons for this. Firstly, the analytical techniques used, due to the nature of the experiments, are incredibly surface sensitive. The ability to prepare and measure samples without even the slightest levels of atmospheric contamination is of critical importance. The pressure required to achieve this depends on the reactivity of the surface, but maintaining an ultra-high vacuum (UHV) of 1×10^{-9} mbar or below is common place. Secondly, the photoelectron measurement techniques described in Section 2.2 require high vacuum environments in order to reduce the mean free path of electrons to the lengthscales ($\sim$1 m) required to measure them - typically base pressures of $\sim 1 \times 10^{-6}$ mbar or better are required.

Methods of producing, maintaining and measuring high and ultra-high vaccum are now so routine in this field there is little merit to discussing them here. However, many of the experiments presented here fall under the category of "traditional surface science" where the surface of a single crystal is cleaned and molecules deposited onto the surface, all in-situ in UHV, prior to measurement. Below is a brief discussion of how this was achieved.

2.1.1 Surface cleaning

The in-situ cleaning of surfaces in UHV was generally done using a combination of sputtering and annealing. For all the experiments here, basic argon sputtering was used whereby argon gas was ionised and accelerated towards the surface - generally at energies between 0.5 eV and 2 eV - using commercial sputter guns.

This high energy bombardment lifts fragments away from the surface but causes a lot of damage. The surface is repaired by annealing, generally to temperatures in excess of 500 °C. Crystallinity of surfaces was routinely checked using low energy electron diffraction (LEED) ensuring the annealing has been sufficient to re-form the surface after sputtering. Successive rounds of sputtering and annealing are often required to ensure the surface is properly clean - this can be checked using X-ray photoelectron spectroscopy (described later in Section 2.2.1) to ensure no unexpected contaminants are present.

2.1.2 Traditional molecular deposition techniques

Although the majority of the work in this thesis looks at molecules deposited using electrospray deposition (see Section 2.1.3), it is useful to draw comparison to the comparable traditional methods for the in-situ growth of films of molecules on surfaces. These techniques rely on the molecules being small and robust so they can be evaporated or sublimed without the molecule breaking apart. This provides a limit on the use of these techniques to study complex chemistry as polymers, photo-sensitisers, molecular magnets, nanoparticles, as well as biological molecules such as proteins, are all often too large or fragile.

Gas dosing

The simplest way to get a species onto a surface is to expose the surface to a partial pressure of the molecule by leaking gas phase molecules into the vacuum chamber. In its most basic form, a UHV leak valve is used to let in a controlled amount of a gas into the chamber. This has the advantage that the dose can be easily measured (generally considered to be a product of the partial pressure and the exposure time) although care needs to be taken as pressure gauges generally have different sensitivities to different gasses. As well as standard room temperature/pressure gasses (e.g. oxygen), high vapour pressure liquids (e.g. water) can also be introduced in this way.

Molecular beam

Many small molecules can be sublimed from evaporation sources such as Knudsen cells (K-cells) - generally an electrical current is used to heat a crucible containing the molecule that you want to deposit. Assuming the solid molecule, generally a powder, has been thoroughly degassed, there should be a minimal pressure increase in the chamber during this process as the molecules tend to stick where

they land - a direct line of sight is therefore required between the source and the sample. Again, this technique allows uniform films to be produced over large areas.

2.1.3 Electrospray deposition system

The electrospray systems used throughout this thesis were all similar variants of the commercially available UHV-4 system from Molecularspray Ltd. This system, outlined in Figure 2.1, allows the pressure to be reduced from atmospheric pressure to $\sim 1 \times 10^{-7}$ mbar in the deposition chamber via three intermediary differentially pumped vacuum stages. The entrance into the system is a 50 mm long stainless steel capillary tube with an internal diameter of 0.005 inches. This inlet capillary can be heated to aid desolvation of the droplets. The three pumping stages are separated by skimmer cones with aperture diameters 0.4 mm and 0.6 mm. The exit from the source into the deposition chamber is a 1.0 mm diameter aperture. The pumping in the first two vacuum stages was normally provided by Varian SH-110 dry scroll pumps. The third stage was pumped using a small $\sim 50\,\mathrm{L\,s^{-1}}$ turbomolecular pump (such as a Varian V-81).

For the emitter capillary, New Objective 5 cm metal taper tips were used with inner and outer diameters of 360 µm and 100 µm. This formed part of an assembly, constructed using PEEK microfluidic components, that provided a liquid feedthrough from a glass syringe and an electrical connection allowing the required high voltage to be applied the liquid. The liquid flow was controlled using a basic syringe pump (NE-300 from World Precision Instruments) and the high voltage using an iseg EHQ-104M. The position of the emitter was controlled using a five axis maniplator (Thor Labs) and was typically on axis to the inlet a few milimeters away. Typically a flow rate of $\sim 0.3\,\mathrm{mL\,h^{-1}}$ and a voltage of $\sim 2\,\mathrm{kV}$ was used. The deposition time varied based on the desired film thickness but monolayer coverage was generally achieved after about 20 minutes and multilayer coverage after multiple hours.

During operation, the deposition was monitored by observing fluctuations in the deposition chamber's pressure and/or the direct measurement of the sample drain current. The inlet capillary was regularly flushed through with solvent to prevent clogging - the risk of which increased with liquid concentration, but using dilute solutions with concentrations below $\sim 0.1\,\%$(w.t.) generally made this manageable. We have shown it is possible to deposit a wide range of molecules from various solvents - a list of successful solutes and solvents is detailed in Appendix A. For some solvents, such as non-polar solvents like toluene and chlorobenzene, a

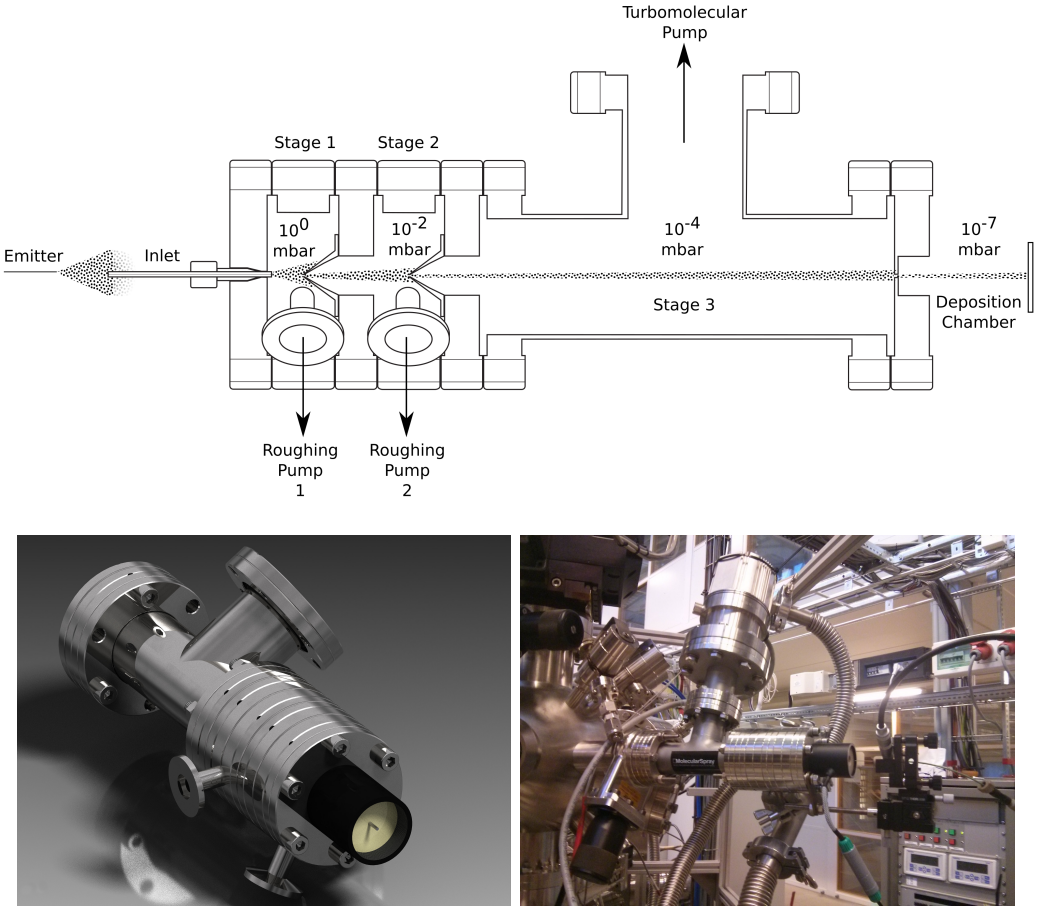


Figure 2.1: Schematic, CAD drawing and photograph showing the Moelcularspray UHV-4 system. The photograph shows the UHV-4 installed on the SPECIES end-station at the MAX IV synchrotron facility.

small amount (∼10 %) of a miscible polar solvent, such as methanol or acetone, was added.

2.2 Photoemission spectroscopy

Photoemission spectroscopy stems from observations of the photoelectric effect in the late 19th and early 20th century where electrons were emitted from a metal surface when irradiated light above a threshold frequency. Einstein famously explained this phenomenon in 1905 [94]. The maximum kinetic energy, E_{max}, of an ejected electron from the surface of a metal is given by the difference between the energy of the incident photon, $h\nu$, and the work function, Φ, of the metal.

$$E_{max} = h\nu - \Phi \tag{2.1}$$

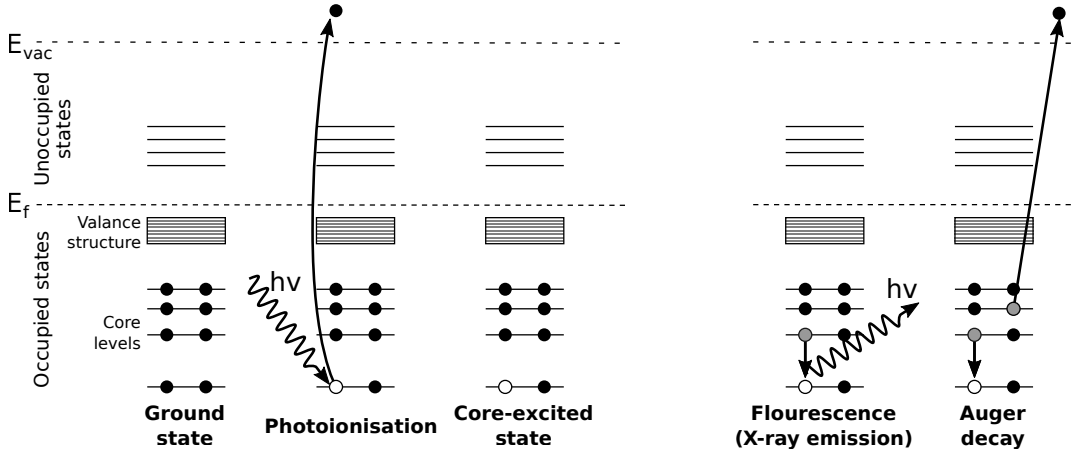
As long as the photon energy is high enough, electrons from any energy level can undergo this photoionisation process. Photoemission spectroscopy describes a suite of techniques that allow us to probe the energies of both occupied and unoccuped states of atoms by measuring this photoinionsation process. Some of these techniques make direct measurements of the resulting photoelectrons and others measure products of the relaxation processes where the final core-excited state decays back into the ground state. Descriptions of these states and the two main decay mechanisms are summarised in Figure 2.2.

2.2.1 X-ray photoelectron spectroscopy

X-ray photoelectron spectroscopy (XPS) is a tool allowing us to probe the chemical environment of electrons. It is a hugely powerful technique not only allowing quantitative analysis of the elemental composition of samples, but also the density and positioning of the occupied electronic states of atoms and molecules. It specifically allows measurements of core level electrons, providing insight into their bonding and chemical environment, and measurements of the valence band structure and molecular orbitals providing insight into electronic structure. This is achieved by measuring the kinetic energy of electrons produced by photoionisation.

Photoelectron spectroscopy is based on a extension of the photoelectric effect where a more general case is considered: the kinetic energy of any individual electron, E_K, after photoionisation is given by

$$E_K = h\nu - \Phi - E_B \tag{2.2}$$



(a) Photoionisation **(b)** Relaxation

Figure 2.2: (a) Energy level diagram showing the initial ground state of an atom, the photoionisation process where a core level electron is liberated to the vacuum and the final core-excited state where a core-hole remains. This final state is unstable and will relax back to the ground state. (b) The two main decay mechanisms - Auger decay and flourescence/photon emission.

where E_B was the binding energy of the electron prior to photoionisation. The binding energy of an electron is an intrinsic property describing the energy difference between the initial state of the atom and the ionised final state where an electron has been removed from an occupied orbital. The binding energy is specific to the bonding/chemical environment of the electron as well as electrostatic effects such as screening (discussed in detail more detail Section 2.2.3).

Photoelectron energy measurement

The kinetic energy of photoelectrons is generally measured using a hemispherical analyser. The basic operating principle is shown in Figure 2.3. The precise use of the electron optics varies between instruments, but generally electrons enter the analyser and pass through a lens system where they are decelerated and focused, through a slit, into the main body of the analyser consisting of two concentric hemispheres. A fixed (but controllable) voltage difference between the hemispheres exerts an electrostatic force on electrons between the hemispheres. If the centripetal force of the electrons, due to their kinetic energy (F=E_K/r), roughly balances with this electrostatic force the electrons will pass through to the detector. If the unbalance is too great, electrons will crash onto either of the hemispheres depending on if they have too much or too little kinetic energy. The electrons that make it will be dispersed across the detector area according to their energy where they are counted. Varying the strength of the retardation

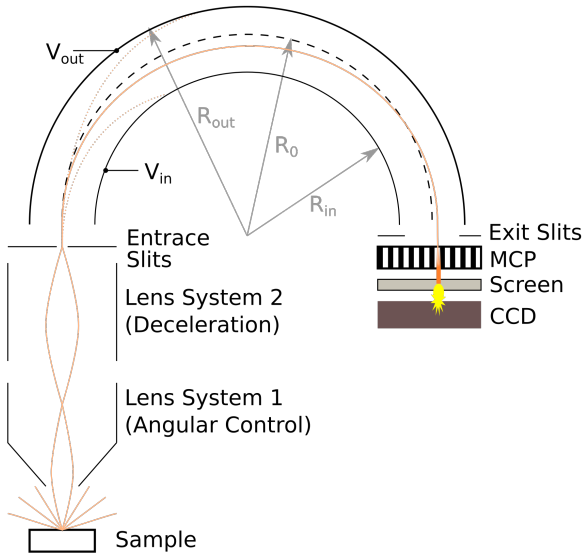


Figure 2.3: Operating principle of a typical hemispherical analyser. Photoelectrons leaving the sample (from an angular range) are accelerated into the analyser. Electrons are decelerated, focussed through a slit into the void between two hemispherical domes with a voltage between them. Only electrons that have kinetic energy within the pass energy range will make it to the detector where electrons are counted. The detector showed here is an MCP detector - here the MCP amplifies the electron signal which created a flash of visible light on a phosphorescent screen that can be detected using a CCD.

potential in the lens system allows the number of electrons reaching the detector to be counted as a function of kinetic energy.

Various types of detector exist - the most commonly used in this study is made up of a microchannel plate (MCP), phosphorescent screen and camera. Very basically an incident electron causes a cascade event in the MCP producing many electrons which impact the screen creating a flash of light bright enough to be detected using a standard CCD or CMOS sensor. This type of detector has the advantage that they are 2D - one axis, as described, is the energy but the other can be used to show information about the angle at which the electron entered the analyser. Such angular measurements without needing to move the analyser around the sample provide a convenient way of measuring band structure. More traditional detectors are either a single or 1D array of channeltrons or similar single channel electron multiplier devices. This approach is well suited to applications where large intensities are measured - MCPs are generally saturated long before these single channel devices but are less suited to high resolution measurements (you are quantising your detection area into generally less than 10

bins). Although not used in this study, the most recent development is the use of delay line detectors. These detectors can either be single or multi-dimension devices and provide several advantages - unlike MCP/camera systems there is very low dark/background count rates and the response is linear across the detector. Most notably they have very fast readout times so are compatible with high count rates and can be used for time resolved measurements.

Although the electron-optics in hemispherical analysers can be fairly complex, for example optics allowing transmission of electrons that entered the analyser only within a specific angular range, the main parameter that needs inputting from the user (apart from the energies one wants to measure, dwell time etc.) is the pass energy. This describes the energy of electrons that travel via a central path between the two hemispheres (indicated by a black dashed line on Figure 2.3). This energy is typically selected from a list of discrete values, typically between 5 eV and 200 eV, depending on the desired application: High pass energies provide higher count rates and allows a wider energy range to reach the detector (with a 2-D detector high pass energies routinely allow spectra ∼15 eV wide to be measured at a fixed retardation potential). However the trade off is high pass energies result in lower energy resolution. As well as pass energy, E_P, the ultimate energy resolution of the analyser is determined by the sum of the two slit widths, $W = w_{entrace} + w_{exit}$, and the size of the spectrometer. Narrower slits and larger spectrometers allow for a greater resolution. This is summarised in Equation 2.3 where ΔE represents the smallest FWHM that can be measured.

$$\frac{\Delta E}{E_p} = \frac{W}{2R_0} \tag{2.3}$$

R_0 is the radius of the path electrons travelling at the pass energy take. For an ideal spectrometer, this is the median path through the spectrometer where $R_0 = \frac{1}{2}(R_{in} + R_{out})$ [95, 96].

Energy calibration

Equation 2.2 tells us the binding energy of a photoelectron can be determined by measurement of its kinetic energy if the photon energy is known given some calibration to take into account the sample's work function. However, the sample work function can be anything but constant and measuring this can even be the objective of photoemission experiments. Fortunately, the measurement technique provides an elegant solution to this whereby the sample work function can be discounted for basic XPS binding energy measurements.

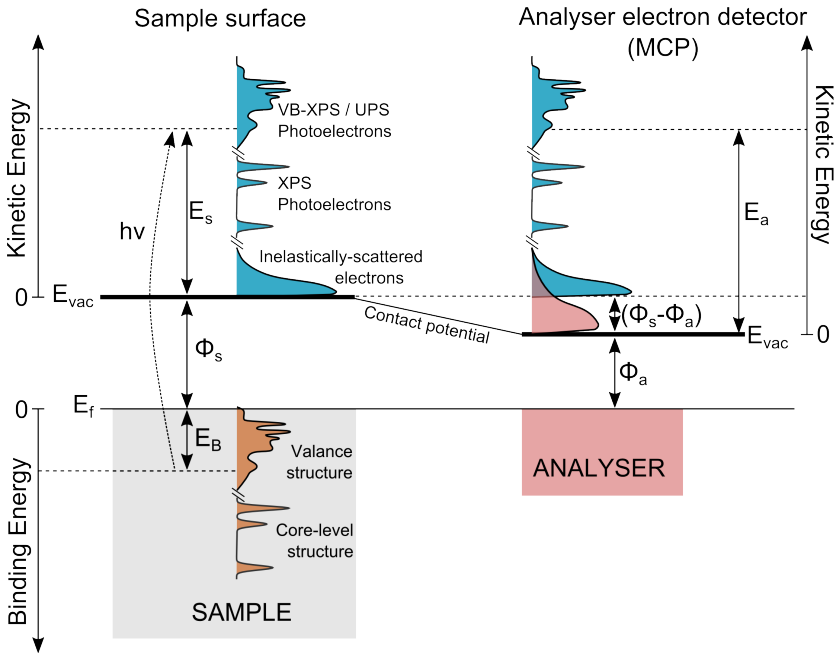


Figure 2.4: Alignment of the sample and analyser Fermi levels create a contact potential offsetting the two vacuum levels. The measured kinetic energy (relative to the vacuum level) is therefore different to that of the kinetic energy of the electron leaving the sample so the analyser work function must be taken into consideration to measure meaningful energy information.

Figure 2.4 outlines how the binding energy of an electron can be determined by means of a band diagram showing the alignment of energy levels for a conducting metal sample and an hemispherical analyser that have a common ground (so the Fermi level of the sample and analyser align). This analysis therefore does not apply to measurements of the gas phase or other electrically insulating samples - the Fermi levels of the sample and detector would not align so the band bending will not occur in the same way. The left hand side of the figure shows the sample. In the grey box, a cartoon of the sample's density of states is shown on a binding energy axis where the Fermi edge provides the defining point of 0 eV binding energy. The photoionisation process takes an electron from any energy with electron density into the vacuum with kinetic energy

$$E_s = h\nu - E_B - \phi_s \tag{2.4}$$

where the work function of the sample is Φ_s. The blue plot shown above the vacuum level is a projection of the samples' density of states in terms of an imaginary spectrum of photoelectrons leaving the sample. This can not be

directly measured but, assuming a constant photon energy, a peak in the number of electrons at a kinetic energy corresponds to a peak in the density of states.

There is an additional feature shown at low kinetic energy: a continuous distribution of a secondary electrons emitted from the sample due to inelastic scattering events generating low energy electrons. The lowest energy edge of this feature, known as the secondary electron cutoff, defines the point of 0 eV kinetic energy and thus the position of the vacuum level at the sample surface.

By the time emitted photoelectrons have passed through the hemispherical analyser and reached the detector, their kinetic energy has increased. This acceleration is due to the detector, shown on the right hand side of the diagram, having a different work function, Φ_a. A contact potential is therefore created between the sample and detector given by the difference in their work functions, $(\Phi_s - \Phi_a)$. Adding the contact potential to the terms in Equation 2.4 gives the measured kinetic energy of electrons in the analyser:

$$E_a = h\nu - E_B - \Phi_s + (\Phi_s - \Phi_a) \tag{2.5}$$

$$E_a = h\nu - E_B - \Phi_a \tag{2.6}$$

So the measured kinetic energy and binding energy are now independent of the sample work function (which can vary even across the same sample - in some samples by design). Therefore the binding energies can be calculated if the analyser work function is known. This constant can be determined by measurement of the Fermi edge. Photoelectrons from the Fermi level have 0 eV binding energy meaning the only unknown in the equation, once the kinetic energy of these photoelectrons is measured, is the analyser work function.

It is worth noting that this approach is also valid for non-metals despite the calibration of the analyser work function requiring measurement of a Fermi edge (which is obviously not present for non-metallic samples). Because the analyser work function is a constant, this calibration can be done using a metal prior to measurement of the non-metal.

The final note-worthy feature is the second cutoff drawn in red on the cartoon spectra measured by the analyser in Figure 2.3. Electron analysers can produce their own secondary electrons, again with a cutoff appearing at the vacuum level (not effected by the contact potential). Care therefore needs to be taken when measuring this energy region as the two cutoffs overlap - the common solution is to apply a bias to the sample to push the kinetic energy of electrons away from

such analyser features. Typically only a few volts is required, but the voltage source needs to be very smooth - a 9 V battery is often used.

2.2.2 Surface sensitivity

One of the key advantages to using photoemission spectroscopy for surface science studies is its surface sensitivity. Although the penetration depth of soft X-rays into a surface is on the order of microns [97], the escape depth of photoelectrons is notably smaller (generally of the order of a few monolayers or nanometres). This is because the interaction between electrons and matter is strong - scattering events are therefore common meaning the mean free path, a function of the energy of the electrons, is short. The mean free path has been empirically derived from various sets of measurements taken of common elements as well as inorganic and organic compounds. An analysis of these datasets is included in reference [98] - one of the fits from which is plotted out in Figure 2.5.

Because of the definition of the inelastic mean free path (the distance through a material which will attenuate the electron intensity by $1/e$) it follows that the measured intensity of electrons that pass through material of thickness d is given by

$$I = I_0 \exp\left(-\frac{d}{\lambda(E)}\right) \tag{2.7}$$

where I_0 is the initial intensity of electrons and $\lambda(E)$ is the inelastic free mean path. In the case of photoelectrons generated in the bulk of a sample, Equation 2.7 describes the intensity of photoelectrons generated from a depth d that make it to the surface and can be measured. A realistic example case would be for $\lambda = 2$ nm, corresponding to $\sim$1000 eV from the universal curve in Figure 2.5, approximately 5% of I_0 can be attributed to photoelectrons escaping from below 5 nm. In other words 95% of the measured intensity comes from the top 5 nm of material. More generally we can say

$$\frac{I_d}{I_{total}} = 1 - \exp\left(-\frac{d}{\lambda(E)}\right) \tag{2.8}$$

where $\frac{I_d}{I_{total}}$ is the ratio between the measured photoelectrons that originate from within a depth d of the surface and the total measured intensity. Finally to consider the more general case where there is an angle θ between the surface normal and the entrance to the electron analyser, we need to take into account

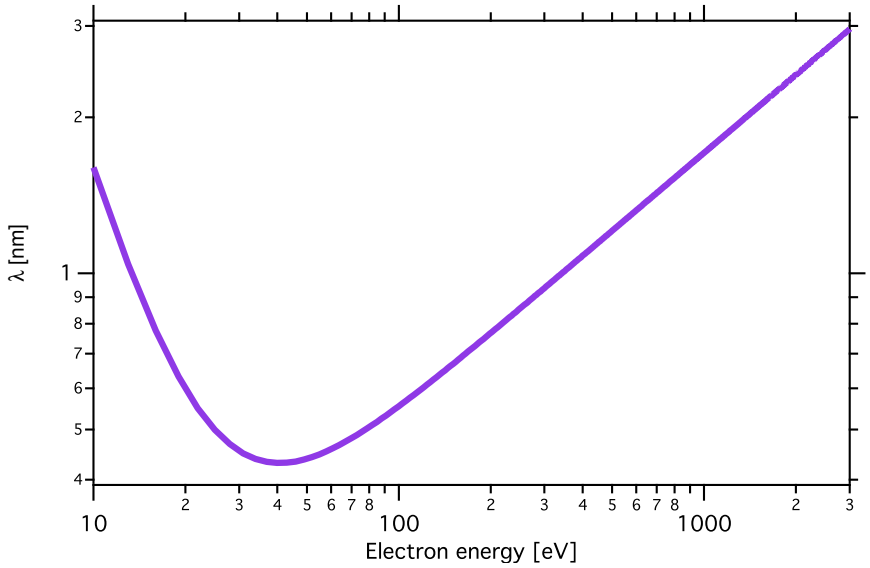


Figure 2.5: One version of the "Universal Curve" showing the inelastic mean free path for electrons travelling through a solid. Calculated using equation, $\lambda = \frac{143}{E^2} \times 0.054E^{\frac{1}{2}}$ from the "elements" dataset in reference [98], where E is the electron energy.

the increased path length the electrons need to take, $d/\cos\theta$. Substituting this in and factoring out I_0 gives

$$\frac{I_d}{I_{total}} = 1 - \exp\left(-\frac{d}{\lambda(E)\cos\theta}\right) \tag{2.9}$$

This implies that the more grazing the sample is to the path of analyser, the more surface sensitive the measurement will be (electrons from within a depth d will make up a greater proportion of the measured signal) [99].

2.2.3 Interpreting XPS spectra

There is a whole range of mechanisms at play that can produce structure in XPS spectra, which are more complex than single peaks corresponding to core levels. These spectral features are a double edged sword - they can make interpretation much more complex but can also provide a great deal of the information.

It can be helpful to consider photoemission as a three stage processes. The initial state effects cover the photoexcitation process whereby a photon is absorbed and a core hole is created. Secondly, the final state effects describe how the atom responds - generally some sort of decay mechanism facilitating relaxation back to its initial state. Both the initial state and final state processes produce electrons which make their way to the surface of the sample and escape into the vacuum.

This final electron transport stage is responsible for a range of extrinsic loss processes.

Koopman's theory [100] states that the binding energy of an electron is given by the difference between its initial and final state. Extrinsic (inelastic) losses can then reduce the kinetic energy of the electron leaving the sample. Understanding the processes that give rise to these effects are therefore critical to correctly interpreting XPS spectra.

Chemical shifts

The position of XPS peaks is very sensitive to the initial state (prior to photoexcitation) as the orbitals, and thus the electron's binding energy, depend on the chemical environment of the atom. This means that shifts in the measured binding energy can infer oxidation states and bonding. Physical interactions can also be apparent but the binding energy shifts tend to be less dramatic.

Auger decay

The lifetime of the core-hole is very short and, for small atoms (low Z), the preferred decay mechanism back to the ground state is Auger decay (discussed previously). Auger electrons appear as constant kinetic energy (rather than constant binding energy) as they are emmitted as a result of an electronic transition. This, combined with the fact the peaks tend to be broarder than photoemission peaks, makes the two easily distinguishable.

Spin-orbit splitting

Spin orbit coupling causes the splitting of XPS peaks when photoelectrons are from orbitals which have angular momentum (i.e. p,d and f orbitals - not s orbitals). Following photoionisation, the photoelectron can either be in a spin up ($s = +\frac{1}{2}$) or spin down ($s = -\frac{1}{2}$) configuration. Without considering spin orbit coupling we would expect electrons with either spin to have the same kinetic energy - i.e. there is no degeneracy between the two electron configurations. However, consideration of the total angular momentum, $j = |l + s|$ where l is the orbital angular momentum quantum number, a degeneracy is apparent which is given by

$$Degeneracy = 2j + 1 \tag{2.10}$$

This degeneracy results in peak splitting where the spin up and spin down electrons appear at slightly different energies due to their interaction with the

Orbital	j values	Degeneracy	Peak ratio
s ($l = 0$)	$\frac{1}{2}$	0	
p ($l = 1$)	$\frac{1}{2}$,$\frac{3}{2}$	2,4	1:2
d ($l = 2$)	$\frac{3}{2}$,$\frac{5}{2}$	4,6	2:3
f ($l = 3$)	$\frac{5}{2}$,$\frac{7}{2}$	6,8	3:4

Table 2.1: Total angular momentum, electron degeneracy and resulting peak areas for XPS of s,p,d and f orbitals

orbital angular momentum vector. If the spin angular momentum vector is parallel to the angular momentum vector, so $j = l + \frac{1}{2}$, the interaction is favourable increasing the kinetic energy of the electron. If they are anti-parallel, so $j = l - \frac{1}{2}$, the interaction is unfavourable reducing the kinetic energy. The size ratio of two peaks is determined by the ratio of the degeneracy values. This is listed for the sub-shells in Table 2.1. The amount of splitting (the separation between the two peaks) is determined by the amount of shielding from the nucleus - ie the separation decreases with increasing principle quantum number, n.

Background

Looking at a "wide"/"overview" scan, a striking feature is the stepped background with decreasing intensity from high to low binding energy. This is caused by extrinsic losses whereby electrons from the bulk lose kinetic energy due to inelastic interactions - the further into the bulk the greater the losses. The background is stepped because this is a cumulative effect from each photoemission peak - the loss processes will always add intensity to the lower kinetic energy side of each peak.

Shake-up and Shake-off features

Shake-up satellites result from the excitation of a valence structure into an unoccupied state. The energy input required for the valence electron to make this transition is provided by photoelectrons (produced by core level photoemission). The measured kinetic energy of the photoelectron is therefore reduced and the separation between the core level peak and the first shakeup satellite should be equal to the HOMO-LUMO gap. Further shake-up satellites are indeed possible between other valence and unoccupied states appearing at even lower kinetic energy. The shake-off process follows the same mechanism but the valence electron is ejected into the continuum of unbound states above the vacuum level. Shake-off features are therefore very broad and can vanish into the background.

Plasmon excitations

Plasmon excitations are another example whereby a core-level photoelectron loses kinetic energy to the valence structure, but in this case, the energy is lost by exciting plasmons. These oscillations have fixed frequencies that are not only dependent on the materials but also form a harmonic series. The resulting spectra is therefore a series of satellite peaks on the higher binding energy side of a photoemission peak that reduce in intensity the further away they get.

X-ray satellites

If an X-ray source is non-monochromatic, an additional satellite structure can be visible. These "ghost peaks", generally at a lower binding energy, are standard photoemission peaks but created by photons with a slightly different energy. This is discussed further in Section 2.3.1.

Charging

The photoemission process is continually removing electrons from the surface into the vacuum which, in the extreme case of the sample being an insulator, quickly causes photoemission peaks to shift to higher binding energy and become very broad. In the case of measuring insulators, electron flood guns can be used to combat this effect by creating a cloud of low energy electrons around the surface that can replenish electrons lost from the surface.

In the case of a conductive sample without the use of a flood gun, no net charge builds as the sample is grounded. However, growing thick films of non-conductive materials on such a sample can still result in charging effects. So even after careful calibration of the binding energy scale (see Section 2.4.1), the position of XPS features of the thick films can appear to be shifted relative to surface features or that of an equivalent thin film.

Screening effects

For the case of having a thin film of molecules on a metal surface, electronic coupling between the molecule and metal can cause screening effects. Screening is caused by the polarization of the atoms surrounding the core hole [101] effectively reducing the localised workfunction manifesting itself as a shift to lower binding energy. This final state effect can be used an an indicator of molecule/surface interactions. The electronic coupling is strongest for thin films - for the case of

multilayer films where XPS probes molecules near the surface of the films, the screening effect is reduced.

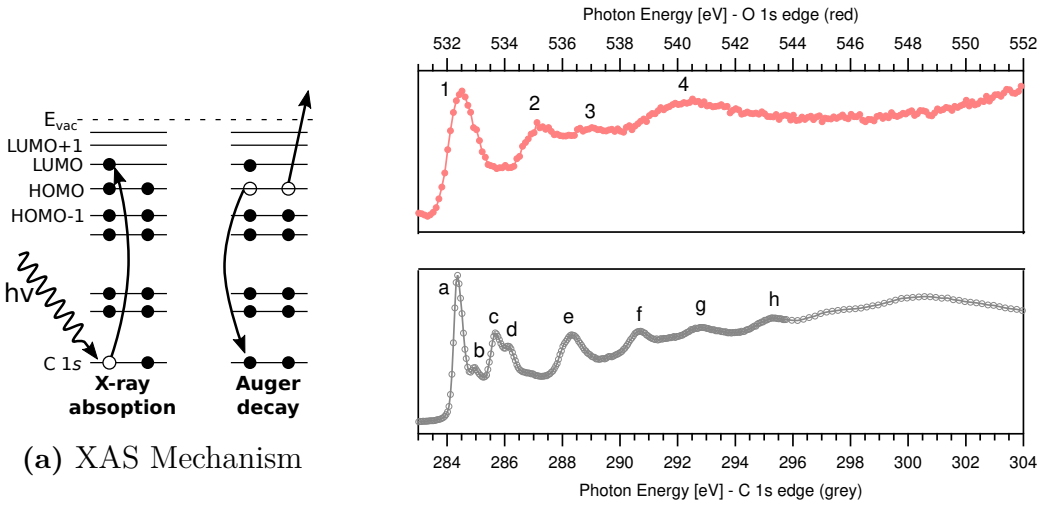
2.2.4 X-ray absorption spectroscopy

The XPS technique described above uses a constant photon energy to probe occupied energy states (whether that be valence or core levels). X-ray absorption spectroscopy (XAS) allows us to probe unoccupied energy levels such as the LUMO states - the alignment of which is critical to the operation of molecular electronic devices. As outlined in Figure 2.6, this spectroscopic technique works by sweeping through photon energies over an absorption edge of a sample - photon's with an energy matching an energy gap between occupied and unoccupied levels can be absorbed promoting an electron into the unoccupied level. The resulting core-excited state decays back to the ground state via Auger or florescence emission. Counting these electrons or photons as a function of photon energy therefore allows us to map out the density of unoccupied states that are accessible by X-ray absorption (as determined by dipole selection rules). This technique is also commonly referred to as Near Edge X-ray Absorption Fine Structure (NEXAFS) spectroscopy.

For molecular systems, choosing an appropriate absorption edge can be important if the aim is to map out molecular orbitals. Although it is possible for any atom in a molecule to absorb a photon exciting an electron into an unoccupied atomic orbital, they are not necessarily part of the molecular orbital of interest. This is much more likely for larger molecules, e.g. nanoparticles, where specific molecular orbitals are not necessarily de-localised across the entire molecule. An example is shown in Figure 2.6b where absorption spectra across both the carbon and oxygen K edges for a multilayer of PCBM (see chapter 6 for information about the molecule). At a glance, we can see the the spectra have very different structure.

The oxygen spectra contains 4 peaks, labelled 1-4, which have been attributed in the literature by DFT calculated NEXAFS [102]. The first peak (peak 1) is attributed exclusively to the absorption into the π^* orbital of the carbonyl (C=O) oxygen. The intensity of peaks 2 and 3 is predominantly due to absorption into a π^* orbital from the methoxy oxygen atom (C-O-C). By the time we get to peak 4 and beyond, we are exciting into the σ^* orbitals - both oxygen species are contributing to this intensity.

The carbon spectrum shows many more peaks, labelled a-h, which Richter et al. have deconvolved using resonant photoemission [103]. Peak a, the first LUMO



(a) XAS Mechanism

(b) XAS measurements of PCBM

Figure 2.6: X-ray absorption spectroscopy (XAS), measured via Auger decay, for a thick film of PCBM deposited via electrospray deposition onto Au(111). (a) Schematic of the XAS mechanism. (b) XAS measurements over the C 1*s* and O 1*s* absorption K edges.

state, is attributed to a highly excitonic π^* state. Peak b represents excitation into the π^* system of the side group and peaks c-e represent excitation into the π^* system of the fullerene. Peak f and beyond represent σ^* orbitals. Richter et al. conclude that there is no overlap of the π^* system of the cage and ligand, which can be treated as separate units.

It is worth noting that for organic molecules, although the carbon C 1*s* edge can be a tempting absorption edge to select (if there is a choice), on some beamlines the so called "carbon dip" can very dramatically reduce the photon flux incident on the sample. This is discussed in section 2.5.3.

XAS measurements can be carried out in a number of ways. Here we discount the methods of detecting fluorescence as only Auger electron measurement was used in this work - for low z molecules the cross section for Auger emission is greater than that of fluorescence. The following describes methods of measuring Auger emission as a function of photon energy.

Hemispherical analyser

Perhaps the most complex method is to use a hemispherical analyser (described in Section 2.2.1). This is generally done using a high pass energy and measuring a fixed kinetic energy window (often called constant final state mode) containing the main Auger peak of interest. The intensity of this peak is integrated as a

function of photon energy (the actual kinetic energy information about the Auger electrons is discarded.)

Drain current measurement

The simplest approach is to measure the sample drain current. As a result of photoemission, the current leaving the sample gives us the total electron yield. The disadvantage of using this technique is that no filtering is possible - it is not just Auger electrons that are measured. There can be sizeable background contributions due to inelastic processes and secondary electrons.

Partial yield detector

A partial yield detector (PYD) typically uses one or more channel plates to measure the current of photoelectrons that pass into the detector. There are typically two grids before the channel plate(s). The first grid is generally grounded and the second held at a negative voltage - this acts as a variable high pass energy filter meaning counts due to background/low energy electrons can be eliminated. Total electron yield can be measured by applying a small positive bias to the grids. Dual channel plate PYDs typically apply a gain of $\sim 10^7 - 10^8$ [104].

This retardation potential is generally set to $\sim$50 eV below the kinetic energy of the Auger electrons. For example, the main carbon Auger emission line is around $\sim$270 eV and in this work a retardation potential of -200 eV was commonly used for XAS measurements over the carbon edge. PYDs can be made to have large acceptance angles and are notably smaller than hemispherical analysers so can be brought relatively close to the sample.

2.2.5 Resonant photoelectron spectroscopy (RPES)

With standard XAS, the photoelectrons leaving the sample are simply counted - their energy is not measured. Resonant photoelectron spectroscopy (RPES) combines XPS measurements with XAS: In its most basic form RPES is an XPS spectra (generally of the valence structure) measured with an incident photon energy that is on resonance with an energy gap in the molecule allowing x-ray absorption and the promotion of an electron from an occupied to unoccupied state. This can accentuate spectral features in the XPS spectra that occur due to decay mechanisms from this core-excited state, such as the participator decay channel (discussed in Chapter 1.4).

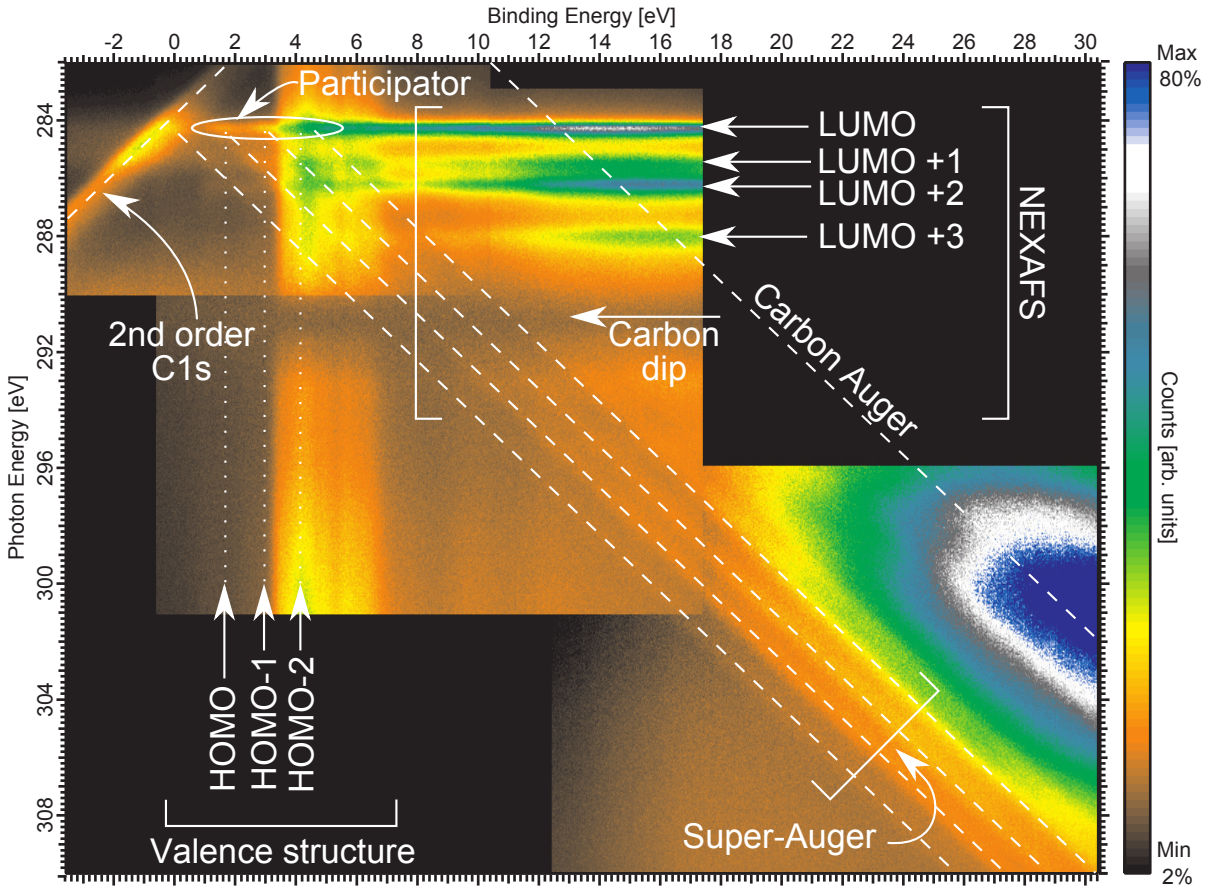


Figure 2.7: RPES map, measured on the i311 beamline at Max IV Laboratory (see Section 2.7.4), of a monolayer of C60 on Ag(111). This is an example system demonstrating the charge transfer of electrons between the surface and the molecules. Key features are annotated. Photoemission HOMO features measured at the LUMO resonance are are enhanced due to participator decay channels (circled). Dashed lines show constant kinetic energy features, starting at the participator enhancements, that are attributed to Auger-like decay mechanisms featuring electrons that have charge transferred into the molecule from the surface.

In a more complex form, XPS measurements can be taken as a function of photon energy resulting in a 2-D map - Figure 2.7 shows one such map for a monolayer of C60 on Ag(111) where there are a number of relevant features showing electron transfer between the surface and molecule [34]. In this example, XPS of the valence band region (a constant binding energy window) is measured as a function of photon energy over the C1s absorption edge. Constant kinetic energy features, such as the carbon Auger, are shown with dashed diagonal lines. The horizontal bands of intensity correspond to resonant enhancement of the LUMO states. Integrating the intensity of these features over the area corresponding to the enhancement of the carbon Auger gives the NEXAFS (marked by with square brackets). The other horizontal feature is the region showing less intensity - this is the so called "carbon dip" is caused by light being absorbed by carbon on the mirrors in the beamline reducing the intensity of of light reaching the sample. The diagonal feature at the top left of the map shows the C1s photoemission peak excited by second order light from the monochromator.

When on the LUMO resonance, we see an enhancement of the HOMO states (marked with vertical dotted lines). This is due to the participator decay channel whereby the electron that had been excited into the LUMO drops back down to fill the core hole - the energy it loses in this process is transferred to an electron in a HOMO state causing it to be emitted into the vacuum. It is worth noting that the final state after participator decay is identical to that of standard photoemission from the HOMO. The two processes are therefore indistinguishable in terms of the measured binding energy but its existence is inferred from the intensity enhancement of the HOMO when measured at the LUMO's excitation energy.

For the case of spectator decay, a core electron is excited into an unoccupied state and, as the name suggests, stays in the LUMO and does not participate in the relaxation to the ground state. Core-hole recombination occurs through an Auger decay process. There is a small shift ($\sim$1 eV) to lower binding energy due to the presence of the spectating electron but the shift is small and often not resolvable in these RPES maps as the main Auger feature is so broad.

The LUMO lies below the silver Fermi level for this system allowing it to be partially occupied. Charge transfer between the metal and LUMO is therefore possible. This opens up the super-spectator and super-Auger decay mechanisms As discussed in Chapter 1.4, these two decay mechanisms are Auger mechanisms that involve electrons originally from the metal surface whilst the photoexcited electron in the LUMO either spectates or tunnels away into the metal surface. Super-spectator and super-Auger account for the constant kinetic energy bands that track back to the participator resonant enhancements - the Auger electrons

involved in the decay originate from either the HOMO, HOMO-1 or HOMO-2 (hence the three bands). The fourth visible band occurs due to electrons in the partially occupied LUMO being involved in the Auger decay (hence tracking back to 0 eV binding energy at the LUMO resonance).

Further discussion of these decay mechanisms and the charge transfer processes can be found in Chapter 1.4 and further examples of how they can be seen in RPES can be found in the literature [6, 11, 33, 34].

In this study, RPES was measured using the spectrometer's constant initial state mode and a large pass energy, typically 200 eV. This creates a constant binding energy window of width ∼16 eV that we can position over the valence band region.

2.3 X-ray generation

Two methods for generating X-rays were utilised in this work. Firstly, X-ray anodes provide a compact and relatively low cost solution for generating X-rays at specific fixed wavelengths. Secondly, when control of the X-ray energy is required, synchrotron radiation was used.

2.3.1 X-ray anode

As shown in Figure 2.8, X-ray anodes consist of one or more metal targets and a filament. A current is passed through the filament (so it is glowing) and a large voltage applied between it and a metal target, causing electrons to be ripped from the filament and accelerated onto the target. Here a number of processes occur but the two most relevant are characteristic and Bremsstrahlung X-ray emission as outlined in Figure 2.9. Bremsstrahlung radiation provides a board background whereby the electrons from the filament are decelerated by electrostatic interactions with electrons in the target. This change in momentum of the electron causes X-ray photons to be emitted. Characteristic X-ray emission occurs after the incident electrons from the filament excite electrons from a low to high energy state in the target's atoms. As electrons decay back to their ground state, X-ray photons with energy equal to the energy gap are emitted.

In order to minimise the effect of the Bremsstrahlung and secondary electrons from entering the analysis chamber, anode sources generally have a very thin aluminium foil "window" that the characteristic X-rays can penetrate. To remove unwanted characteristic peaks, some lab sources utilise a monochromator. Using a toroidal quartz crystal in the Rowland circle geometry[105] it is possible to not



(a) Schematic **(b)** Omicron DAR400

Figure 2.8: (a) Schematic of the inside of a typical dual anode X-ray source. (b)Photograph of an Omicron DAR400 anode source (from www.ormicron.com).

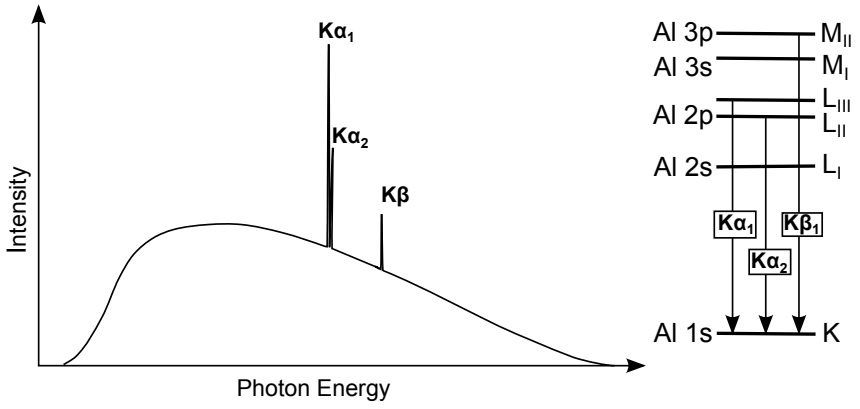


Figure 2.9: Cartoon showing characteristic X-ray emission and Bremsstrahlung background for Aluminium

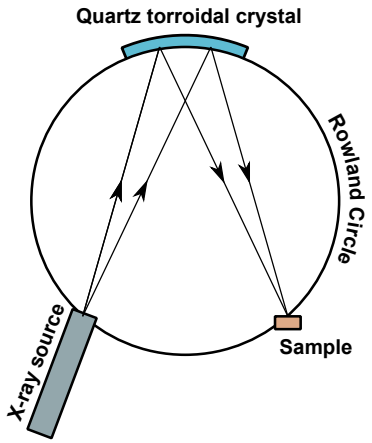


Figure 2.10: The Rowland circle geometry along with a quartz crystal is a common combination for the monochromation and focussing of x-ray emission from an anode

only remove unwanted X-ray emission peaks but also to focus the X-ray spot onto the sample. This arrangement is outlined in Figure 2.10. In accordance with Bragg's law, $n\lambda = 2d_{hkl}\sin(\theta)$, only integer wavelengths matching the path length difference ($2d_{hkl}\sin(\theta)$) between light diffracted by the parallel crystal planes (separated by d_{hkl}) will constructively interfere. By setting the incident angle, θ (measured from the plane of the surface), so that the path length difference equals the wavelength of the desired emission line, the unwanted spectral contribution is vastly reduced.

Monochromatic x-rays not only provide an increase in energy resolution and filter out unwanted characteristic emission, but also reduce of the measured background. This is demonstrated in Figure 2.11 which shows XPS measurements of gold (not UHV clean). The lower binding energy satellite features next to Au peaks in the non-monochromatic wide scans (not present in the monochromatic data) are due to K_β X-ray emission.

2.3.2 Synchrotron radiation

Although high quality XPS can be collected using X-ray anodes, for measurements such as XAS and RPES, continuous control of the photon energy is needed. It is also beneficial for XPS to be able to measure at photon energies that are near to the binding energy of the core level to maximise the photoionisation cross section, and to change surface sensitivity (higher photon energies create higher kinetic energies increasing their escape depth).

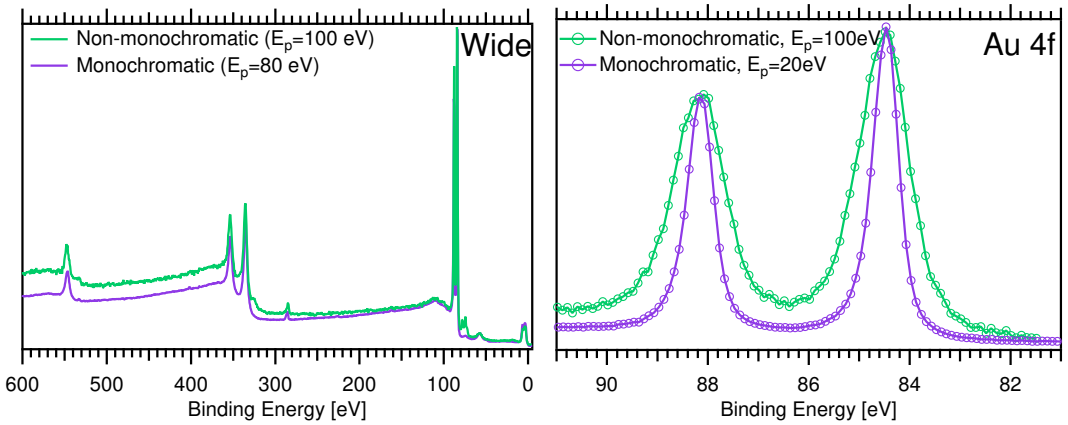


Figure 2.11: XPS wide-scan and the Au 4*f* region measured using both a monochromatic (purple) and non-monochromatic (green) Al K_α x-ray source. The monochromatic data was collected using a Kratos Axis Ultra instrument and the non-monochromatic using the VESPA system - details of which are outlined in Section 2.7. For the wide-scan the pass energies (E_p) are comparable. For the Au4f region, the pass energy was lowered to the point further reduction showed no obvious improvement in resolution. All data was collected at normal emission and normalised to the Au 4f peaks.

When the momentum of a fast moving electron is changed a photon is emitted in order to obey conservation laws. These photons, known as synchrotron radiation, were first thought of as a nuisance when observed at the General Electric Research Laboratory in 1947 [106], but facilities are now designed with the purpose of producing this radiation - the first being the Synchrotron Radiation Source at Daresbury Laboratory [107]. The radiation is of great use because it can span a huge range of wavelengths (from microwaves to hard X-rays) and is very intense. Modern synchrotrons can also operate in time resolved modes allowing "pump-probe" measurements [108].

Electron synchrotrons in their most basic form consist of an electron source, a linear accelerator to accelerate the electrons to relativistic speeds and a large (typically ∼100 m) diameter storage ring where the orbit and relativistic speed of the electrons is maintained using magnetic and electric fields. In reality storage rings are made up of straight sections and corners (rather than being a continuous ring). Bending the path of electrons round each bend is done using bending/dipole magnets. Focussing of the beam is done using quadrupole magnets. As the electrons travel round the ring, radiating their energy as photons, their energy/speed is maintained using an RF (radio frequency) cavity. This sinusoidal signal from which means that the electrons go round the ring in bunches - any

electrons outside of a bunch are scattered as they are out of phase with pulses of energy provided by the cavity.

Bending Magnets

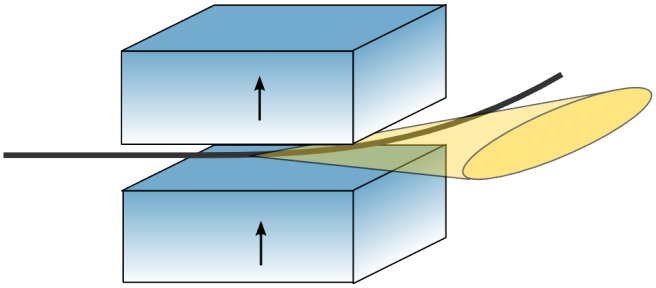
The most basic source of synchrotron radiation is emitted from the bending magnets that make up the storage ring (between straight sections). They produce a broad-band continuous distribution of photon energies.

Insertion devices - wigglers and undulators

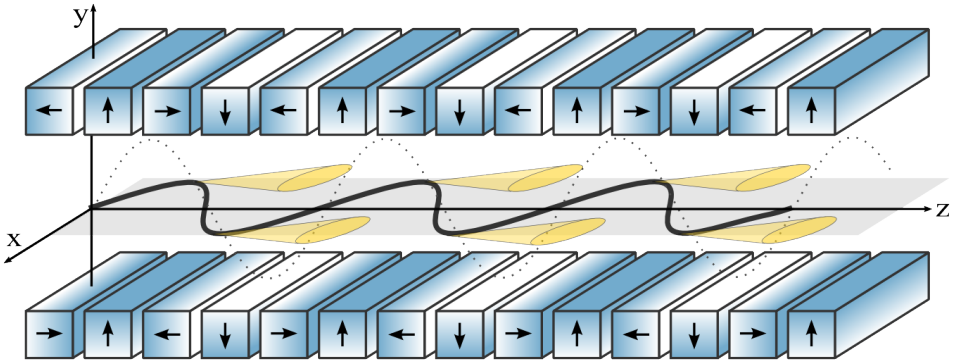
The two types of insertion device used in "3rd generation" light sources are wigglers and undulators. As shown in Figure 2.12, both of these devices are based on the same principle: a periodic array of dipole magnets creating a sinusoidal magnetic field. The path of the electrons is therefore forced to oscillate. The number of magnets that make up each period is variable but 4 is a common number providing a good balance between engineering practicality and a the ideal field design [108].

The design of undulators and wigglers differ only in the size of the electron oscillations with wigglers providing a larger oscillations than undulators. This however does have a dramatic effect on the radiation produced. Wigglers are designed to produce radiation with similar properties to a bending magnet but at a much greater intensity. The majority of the energy is radiated from the electrons at the turning points of the oscillatory path as this is when the momentum change is greatest. Wigglers rely on the light output at these two extremes being physically separated so interference effects are limited. The output intensity is given by the sum of the intensities of all the "emission cones" so scales with $2N$ (where N is the number of periods in the wiggler). Wigglers are not used in this work so will not be discussed further

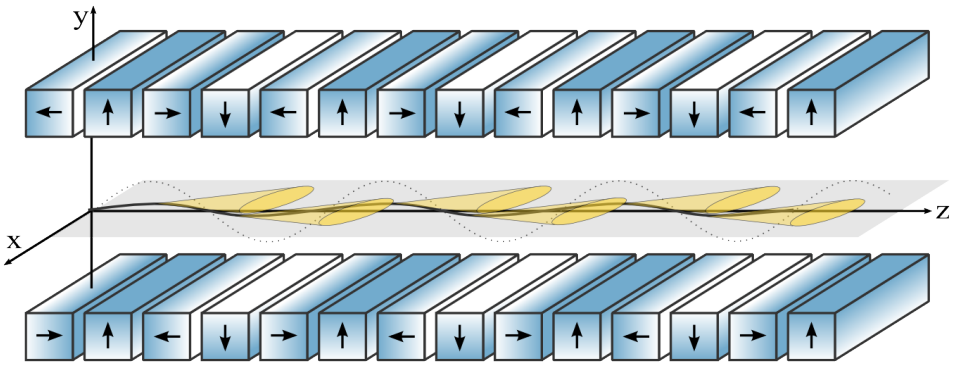
In undulators, unlike wigglers, electrons undergo much smaller amplitude oscillations meaning the light output from each oscillation overlaps. The resulting interference produces narrow regularly separated bands of intense radiation. This is shown in Figure 2.13. The physics describing the operation of undulators is well established and can be found elsewhere [109], but when operating undulators the key difference is one needs to consider the separation between the magnet arrays as this controls the output characteristic of the radiation. There are three parameters. Firstly, the "gap", which describes the separation between the magnetic arrays, controls the field strength which determines the position and separation between the harmonic bands. Smaller gaps also produce more intense harmonics. Secondly, some undulators allow a taper of the magnetic arrays to be set. This allows the



(a) Bending Magnet



(b) Wiggler



(c) Undulator

Figure 2.12: Schematic showing the operating principle of: (a) bending magnets, (b) wigglers and (c) undulators. The solid line shows the path of the electrons (on the x,z plane) and the dotted line the magnetic field (y,z plane). Black arrows denote the field direction/orientation of the magnetic elements. Photon emission is shown by the yellow cones.

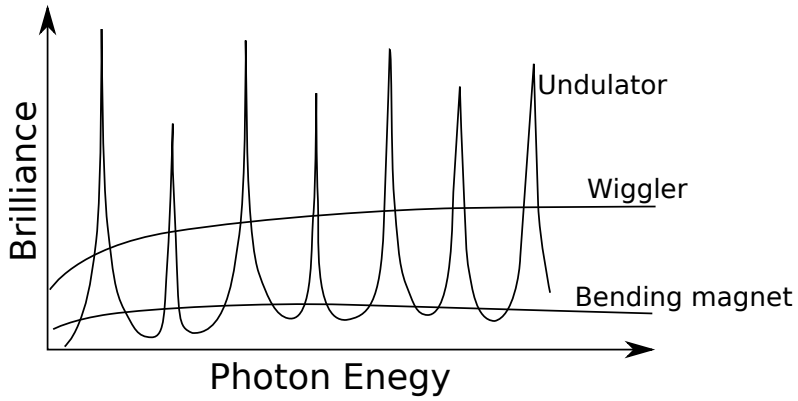


Figure 2.13: Cartoon plot showing the differing characteristics of synchrotron radiation produced by bending magnetic, wigglers and undulators. The positioning of the undulator harmonics can be controlled by varying the gap.

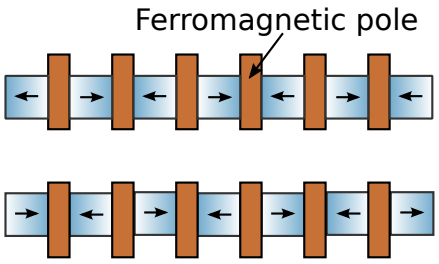


Figure 2.14: Diagram showing the design principle of a hybrid undulator where ferromagnetic poles are used between the magnetic poles (oriented in the plane of the electrons).

flux to be more uniform for a given energy range. Finally, a lateral offset between magnetic arrays allows control over the polarisation (often 4 arrays are used for this). When the magnets are perfectly aligned, the polarisation is linear as the electrons oscillate back and forth on a 2D plane. By applying an offset between magnetic arrays, the electrons can be made to undergo a three dimensional helical path. Not only does this effect the polarisation but it also causes higher harmonics to be dominant. This study does not make used of these "helical" undulators - only linearly polarized light is considered.

One final relevant consideration in the design of undulators is the use of ferromagnetic poles between the magnetic poles as shown in Figure 2.14. These "hybrid" undulators the advantage of having larger peak fields for the same gap size and period as the "Pure Permanent Magnet" (PPM) arrangement (shown in Figure 2.12c) [110].

Beamlines

As the light output from the synchrotron is broadband and divergent - a series of mirrors and gratings, that make up a "beamline", is used in order to focus and monochromatise the light. Although there are a variety of beamline designs, the following generalisation describes the a basic/common series of optical elements that make up a beamline: Firstly mirrors are used to focus and collimate the light that comes out the the insertion device in the horizontal and vertical planes. The light then enters the monochromator which consists of mirrors and a grating that are rotatable to allow diffracted light of the desired wavelength to pass through a set of exit slits. The separation of these slits is often variable to allow the user to select an appropriate balance between resolution and flux. Finally another pair of mirrors and slits can be used to focus and shape beam that is incident onto the sample.

2.4 XPS data processing

2.4.1 Energy calibration

Binding Energy

For metallic samples measured at a synchrotron, the binding energy scale was calibrated using the position of the Fermi edge which by definition is 0 eV binding energy. When using a anode source, measurement of the Fermi edge is harder so a metallic core level substrate peak was used as a reference. For non metallic samples, another well defined core level was used as a reference.

Using a lab source this process is trivial because this calibration should remain fairly constant (the so called analyser work function). However, at a synchrotron this is not the case. Often even between XPS measurements the monochromator is moved meaning every spectra needs calibrating. Two approaches can be used: either measure a fermi edge (other other reference spectra) every time the monochromator is moved or measure spectra in an order and repeat specific measurements so the measurements can be calibrated to each other.

Ionisation Potential

As well as the binding energy and kinetic energy, it can also be helpful to refer to the ionisation potential, E_I, of electrons. This quantity, the energy required to remove an electron to the vacuum, takes into account the work function as well as the binding energy but is not referenced to the sample's Fermi edge. It is therefore

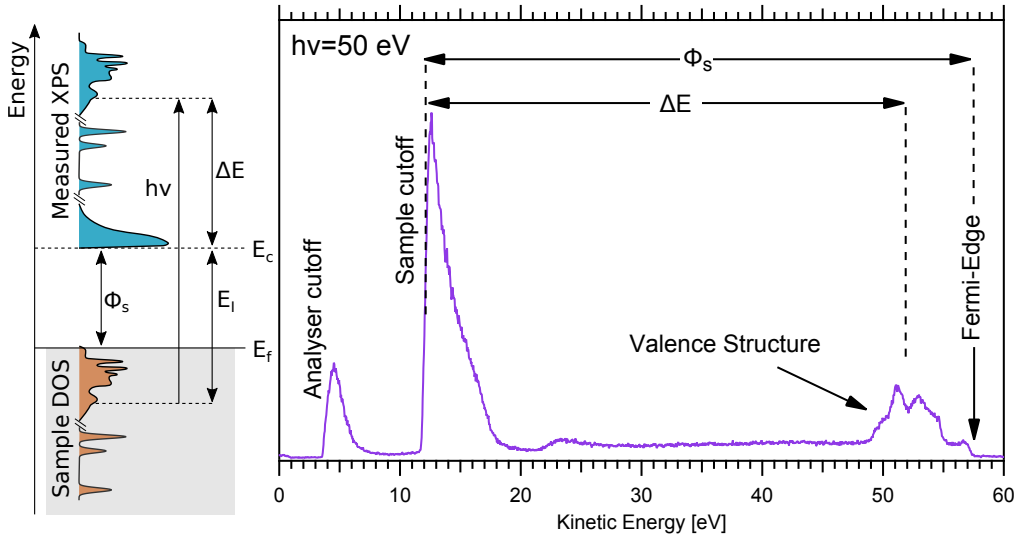


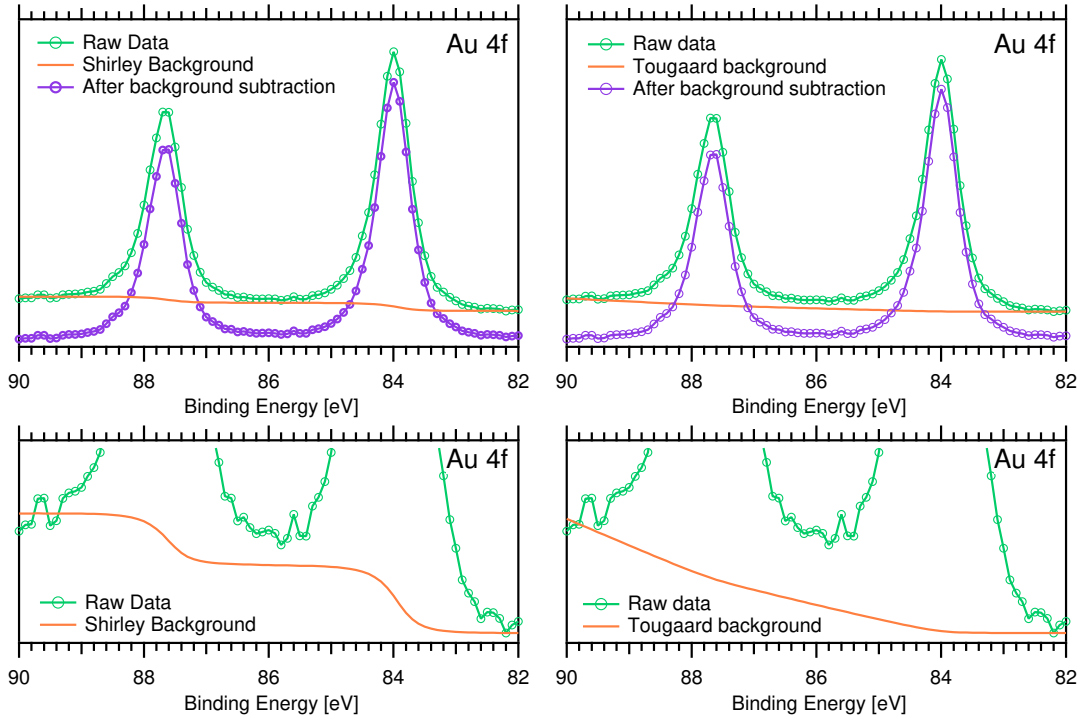
Figure 2.15: Method for measuring the ionisation potential of electrons and example spectra showing the cutoff, valence band and Fermi-edge for clean Au(111). X-ray light of a known energy, in this case $h\nu = 50$ eV, takes electrons from the sample to the vacuum. Measuring the energy difference between the measured energy of an electron and the the secondary electron cutoff, ΔE, allows the ionisation potential of an electron to be determined.

useful when wanting to measure the absolute positions of electronic states as ionisation potential measurements are not affected by, for example charging effects due to film thickness. The method used to determine the ionisation potential is that of Maxwell et al. [111] and is summarised in Figure 2.15. Light of known energy excites an electron from the sample into the vacuum - the ionisation potential is

$$E_I = h\nu - \Delta E \tag{2.11}$$

where ΔE is the kinetic energy difference between the secondary electron cutoff and electrons kinetic energy. As mentioned in Section 2.2.1, in order to measure the cutoff a bias of several volts needs to be applied to the sample to give these electrons that would otherwise have 0 eV kinetic energy to enter the analyser. The voltage needs to be sufficient to move the samples' secondary electron cut-off beyond the cutoff generated by the analyser's detector in order to accurately measure the cutoff position.

The same method allows the work-function of a metal to be measured as this this equal to the ionisation potential of the Fermi edge.



(a) Shirley background **(b)** Tougaard background

Figure 2.16: Subtraction of Shirley and Tougaard backgrounds

2.4.2 Background subtraction

Several functions are used to fit the background under curves to allow peak fitting and other quantitative analyses. XPS backgrounds can be complex - as mentioned previously they are largely due to the build-up of low energy secondary electrons and inelastic scattering meaning simple linear backgrounds rarely provide a good quality fit. The approach taken here to fit the inelastic background used here was that described by Shirley [112] who made the simple assumption that the background intensity is caused entirely by the scattering of higher energy electrons. The background at a certain energy is therefore proportional to the integral of the intensity above that energy.

The alternative to the Shirley background is the Tougaard background [113] which was not used in this thesis but is shown here for comparison.

Often spectra can sit on the tail of the secondary electron cut-off - this normally occurs when measuring low kinetic energy peaks. An exponential or power law fit of the background was generally used in this case.

2.4.3 Peak fitting

Several factors contribute to the shape of XPS peaks which generally contribute to either Gaussian or Lorentzian broadening. A combination of these two functions is generally used for curve fitting via an approximation called a pseudo-Voigt function where a weighted sum of the two curves is used [114]. A brief discussion of Lorentzian and Gaussian broadening follows.

Lorentzian contributions

The fundamental limit to the width of an XPS peak is determined by the core hole lifetime (τ). This Lorentzian contribution, called the natural line width (ΔE_0), can be estimated from the uncertainty principle

$$\Delta E_0[\text{eV}] = \frac{\hbar\ [\text{eV.s}]}{2\tau\ [\text{s}]} = \frac{6.6 \times 10^{-16}\ [\text{eV.s}]}{2\tau\ [\text{s}]} \tag{2.12}$$

where $2\Delta E_0$ describes the full width (rather than the half width) of the peak [115].

Gaussian contributions

The combined effects of other types of broadening are generally considered to be Gaussian [116]. These can include instrumental broadening, such as the energy resolution of the spectrometer or the X-ray source, and genuine variations in the energy of electrons in the sample, e.g. from vibrational broadening [117].

2.4.4 Quantitative measurements

XPS is widely considered to be a quantitative technique; the implied meaning of which is that the ratio of different photoelectron peaks can be related back to the amount of the species that the electrons came from. This requires consideration of the cross section for photoionisation, which is dependent on both the electron's orbital (ie the type of atom and energy level) and the photon energy - calculated values for which exist in the literature [118, 119]. This can be applied in two ways: Firstly, assuming that the cross section does not change for electrons in different bonding environments of the same species, implies a direct link between peak areas and quantity of each environment, Secondly, the ratio of different species can be inferred by comparing the area under peaks for each species multiplied by its photoionisation cross section.

It is worth noting that in some cases the situation is more complex. Authors have described cases where intensity ratios between two peaks that describe different chemical environments of the same orbital oscillate as a function of photon energy [120].

It is also possible to use XPS to measure film thickness by looking at the suppression of XPS peaks as film thickness is increased. This was alluded to by the equations in Section 2.2.2 where the surface sensitivity of the technique is discussed. This approach is well suited to thin films, such as oxides on both crystals such as silicon [121] or more complex structures like nanoparticles [122].

2.5 XAS data processing

2.5.1 Photon energy calibration

The photon energy at a synchrotron can often be determined by measuring the kinetic energy of a core level using both first and second order light produced by the beamline's monochromator. The first and second order peaks are found at:

$$E_{K1} = h\nu - E_B \tag{2.13}$$

$$E_{K2} = 2h\nu - E_B \tag{2.14}$$

The energy difference between these two spectra is therefore equal to the photon energy. This works because any effect that can change the measured kinetic energy would have an equal effect on both of these measurements. After an XAS or RPES scan, this technique was used to measure the exact energy that the scan finished.

2.5.2 Density of states

XAS data can be placed on a binding energy scale and placed along side valence band XPS measurements to produce a density of states plot[123]. The binding energy of a point in a NEXAFS spectrum can be expressed relative to the binding energy of the core hole created by the X-ray absorption process, which is referenced to the Fermi level by XPS measurements (for XAS over the nitrogen K edge, the binding energy position of the N $1s$ core level is used). This is done, once the photon energy scale of the NEXAFS and binding energy scale of the XPS has been calibrated, by subtracting binding energy position of the core level from the photon energy scale of the NEXAFS. This principle is explained in Figure 2.17.

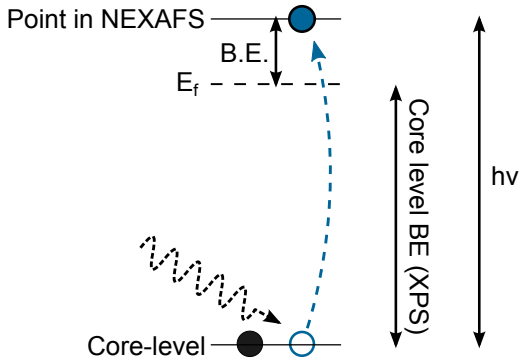


Figure 2.17: Showing how a position in a NEXAFS measurement can be positioned on a common binding energy scale with XPS measurements (referenced to the Fermi edge)

It is worth noting this gives the position of the unoccupied energy levels (relative to the binding energy) whilst in the core excited state.

2.5.3 The "Carbon Dip"

Carbon contamination on the mirrors of the beamline will absorb X-rays in the same way a carbon sample would. Therefore absorption measurements taken at a carbon edge see a non-uniform reduction in the flux incident on the sample. This effect can be measured using a clean sample containing no carbon - not having any accessible resonances on the surface means that the shape of the background reflects the intensity profile of light exiting the beamline. Dividing the measured carbon XAS spectra through by this background allows the effects of the carbon dip to be minimised.

2.6 RPES data processing

RPES by its nature is a combination of photoemission and absorption measurements. Assuming a map is produced as described in Section 2.2.5, the binding energy axis is calibrated in the same way as XPS (described in Section 2.4.1). The photon energy scale is calibrated in the same way as XAS (Section 2.5.1). The carbon dip is again minimised by diving through by a background spectra measured using a clean, non-carbonaceous sample.

NEXAFS can be extracted from RPES maps by integrating over the Auger region. This is less optimal than taking separate XAS measurements as the Auger features drift out of measurement region as the spectrometer is typically set to measure a constant binding energy (rather than constant kinetic energy) window.

This strictly limits the NEXAFS measurements extracted from RPES to the near edge structure.

2.7 Instruments/facilities used

Technical information about the various facilities used for the measurements presented in this thesis are included below.

2.7.1 VESPA

Our home-built lab-based system in Nottingham allows XPS, UPS (ultraviolet photoelectron spectroscopy) and PEEM (photoemission electron microscopy) measurements. An Omicron DAR400 X-ray source with magnesium and aluminium anodes, Omicron HIS-13 helium UV lamp and a Scienta R3000 hemispherical analyser provide spectroscopy. Standard sample preparation facilities including electron beam heating, argon sputtering and LEED can be carried as well has ability to use k-cell deposition sources and dose gasses. A Focus PEEM with an IEF (imaging energy filter) allows imaging of work function variations on the micron length scale. A Molecularspray UHV-4 and Extrel 150-QC quadrupole mass filter allowed electrospray deposition.

2.7.2 Kratos Axis Ultra

This commercial system utilises a monochromatic Al source (single anode with quartz torrodal crystal monochromator), non-monochromatic dual anode (Mg and Al) source and helium UV lamp source. The analyser is equipped with a series of apertures and a magnetic immersion lens system allowing the measured area to be controlled by the analyser, however for measurements presented here the analyser was run in "hybrid mode" where a larger slit is used allowing measurement over an area of $\sim 700\times\ 300\,\mu$m. Measurements were taken with the monochromatic source which has a spot size of the order 1 mm, which when combined with low pass-energy measurements allows XPS measurements with a binding energy resolution comparable to that measured at synchrotrons.

2.7.3 MAX-Lab D1011

This bending magnet beamline is equipped with two end-stations - the front end-station for photoelectron spectroscopy and the back X-ray magnetic circular dichroism. For this study the front end-station was used which is equipped

with a Scienta SCIENTA SES200 (upgraded) analyser, a partial yield detector, argon sputtering, e-beam heating and LEED. The sample is mounted on a large, motorised manipulator containing a cryostat mounted vertically allowing the sample to be positioned in either the preparation or analysis chambers (which are mounted on top of each-other)

The bending magnet itself has two additional quadruples allowing control of the tilt of the electron's orbit through it producing elliptically polarized light. The light can be considered linearly polarized when no tilt is applied (the set-up used in this study). The beamline consists of pre-mirrors followed by an SX700 monochromator (containing a movable mirror and grating, followed by a focussing mirror). The output of the monochromator is focussed onto adjustable exit slits before entering the analysis chamber (with no additional optics). The spot size on the sample is $\sim$1 mm high and $\sim$3 mm wide.

Beamline D1011 is a low intensity beamline that is ideal for XPS and XAS measurements of molecules that are prone to beam-damage on higher intensity beamlines. The XAS data collected over C1s edge is very nice as the carbon dip is manageable allowing reasonable intensity at all energies.

2.7.4 MAX-Lab I311

I311 is a soft X-ray undulator beamline allowing high resolution high flux photoemission measurements between 30 and 1500 eV. As with D1011 there is a second end-station (this time for XPEEM measurements) that was not used in this study. The photoelectron spectroscopy end-station's analysis chamber is based around a Scienta SES200 hemispherical analyser. The preparation chamber contains LEED, e-beam or resistive heating sample heating (depending on how the sample stage) and argon sputtering. The sample is mounted on a large bellows manipulator containing a cryostat mounted vertically allowing access to both the preparation and analysis chambers.

Detailed information about the beamline is included in reference [124] but to summarise: A hybrid type undulator is used that allows a tapering of the magnetic gap allowing a smoother variation of photon energies which is of benefit to absorption measurements. As with D1011, after the pre mirror comes a modified SX-700 monochromator that allows access to the complete energy range from the single grating. Adjustable exit slits followed by two refocussing mirrors allow high energy resolution and a spot size of 500 $\times$ 100 microns.

I311 produces relatively high flux, which when combined with the ability to taper the magnetic gap, means it is ideal for producing the RPES maps previously

described where we are often trying to probe weak features. Beam-damaging the types of organic molecule studied here was almost guaranteed on this beamline - the effect of this is minimised by slowly moving the sample in the vertical direction.

Chapter 3

Instrument development for the characterisation of electrospray ionisation

3.1 Ultra-short exposure video capture of electrospray ionisation

3.1.1 Introduction

The electrospray ionisation mechanism is well suited to be studied using microscopy due to the sub-millimetre length-scales of measurable quantities such as drop size and jet length. However, typical video cameras have acquisition times of $\sim$10 ms, which limits their capability to resolve detail for fast processes like electrospray where a drop can fly across the field of view within that time-scale . Sufficiently reducing the acquisition time of each frame is possible with very expensive high speed cameras, but a more cost effective option can be to have a very short pulse of illumination within the longer frame duration of a more affordable camera. This allows sharp images of fast processes to be acquired despite the long acquisition time.

With both methods, reducing the acquisition time and reducing the light exposure time, the challenge is to get enough light on the sensor in a short time-scale to get a high enough signal over the noise/background level. This thesis presents an instrument, where a relatively low cost high speed camera is coupled to a pulsed laser facilitating a short pulse of light in each frame, that can be used to image micron to millimetre sized objects. In this study, it was used to image electrospray ionisation (see chapter 1.5.

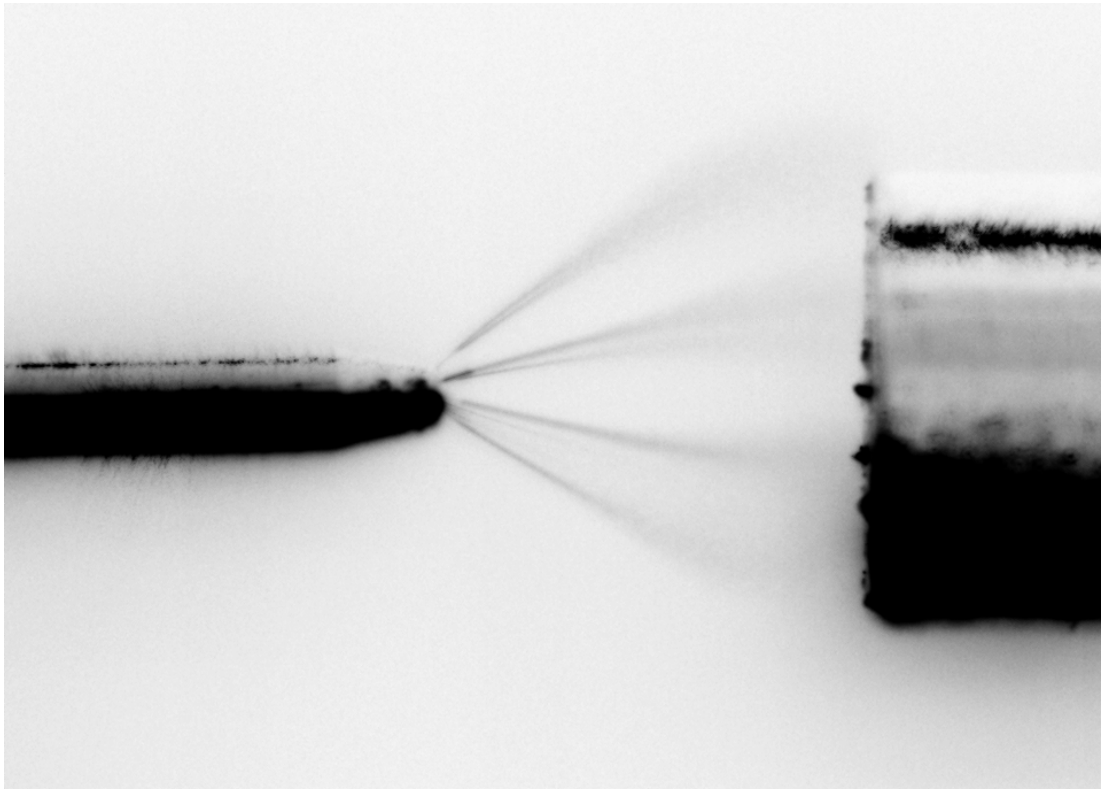


Figure 3.1: Standard camera image of the multi-jet regime of electrospray ionisation

3.1.2 Instrument details

The camera used was an Optronis CL600x2 which could capture at maximum frame rate of 600 fps at its full resolution (1280x1024). This was used as a trigger source to control a 527 nm diode pumped solid state (DPSS) pulsed laser (from Laser 2000) producing one ∼7 ns pulse of light per each trigger. A delay between the camera trigger and the pulse of light was introduced, using home built electronics, allowing control of when in the frame the light pulse was produced.

3.1.3 Development

The problems with using laser light directly as a light source for traditional imaging is illustrated in Figure 3.2 where an example image of electrospray ionisation along with a diagram of the optical system used is shown. Although there is more than sufficient light intensity and the image contains resolvable edges , the images are dominated by a speckle pattern and diffraction effects resulting from the coherent nature of laser light. The challenge was to find a way of producing short, collimated pulses of light that are incoherent.

Our solution was to utilise fluorescence. Rhodamine 6G dye was dissolved in methanol to a concentration of 0.1 mg mL^{-1} (0.2 mM) which is highly fluorescent when excited with the 527 nm laser light. This concentration was selected based on some approximate intensity measurements, made using a UV-vis spectrometer, of the light-output from the dye when excited by the laser. This was measured over a range of concentrations with two different sizes of cuvette, with path lengths 0.6 mm and 1.1 mm; the results are shown in Figure 3.3 along with an example transmission spectra of the fluorescence. Longer path lengths were seen to visibly reduce the intensity (the dye was reabsorbing light produced by the original excitation).

Given the fluorescence lifetime of less than 10 ns for such a dilute concentration of the dye [125], this system makes an ideal incoherent light-source that can still be turned on and off within 20 ns. Initially, a small amount of the dye was placed inside a transparent acrylic cylinder, as shown in Figure 3.4, which was used as a back-light for the electrospray. An example image collected using this technique is also included. This image lacks the sharpness of the image collected using the direct laser light and is notably darker. It does however not have the speckle pattern or diffraction effects.

The image quality using this technique was improved firstly by producing more light and secondly collimating the light output from the dye. This was achieved using the unique dye cell design shown in Figure 3.5a with the optical system

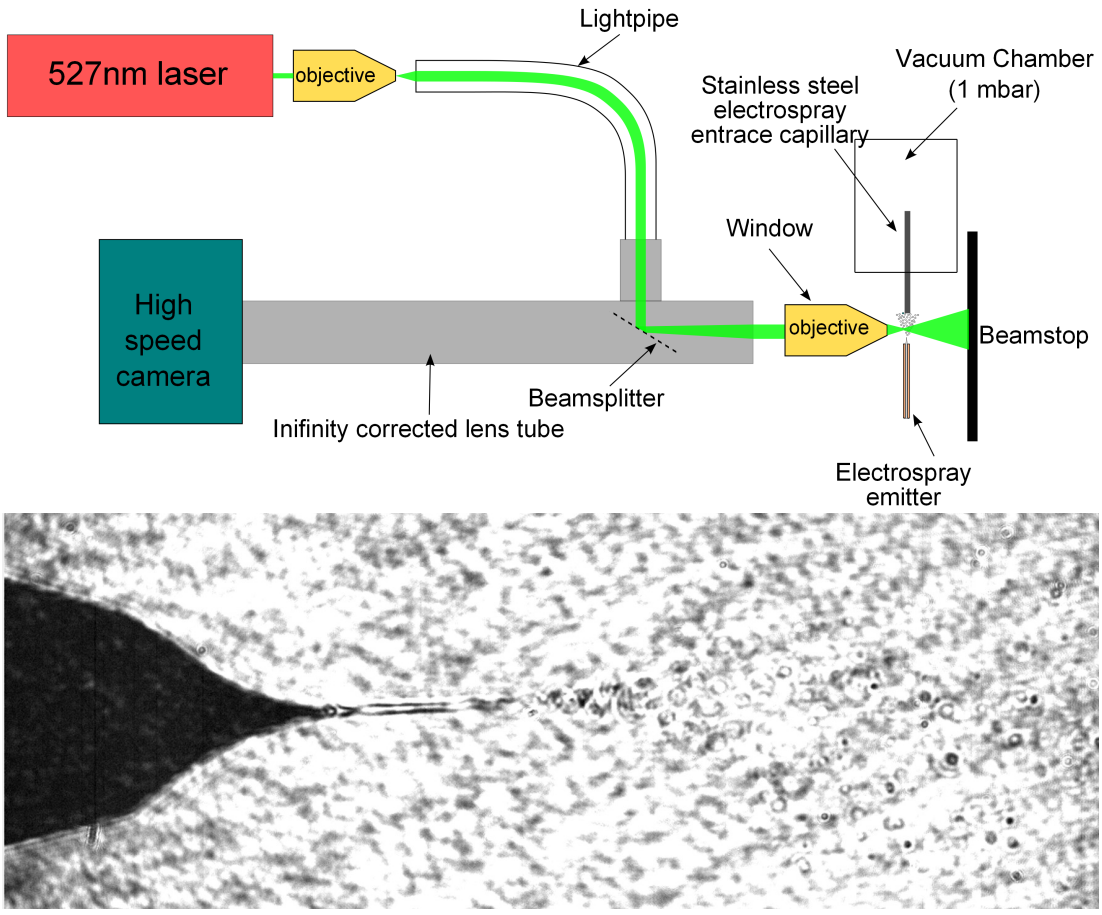


Figure 3.2: Optical set-up and example image demonstrating the direct illumination of electrospray ionisation by laser light.

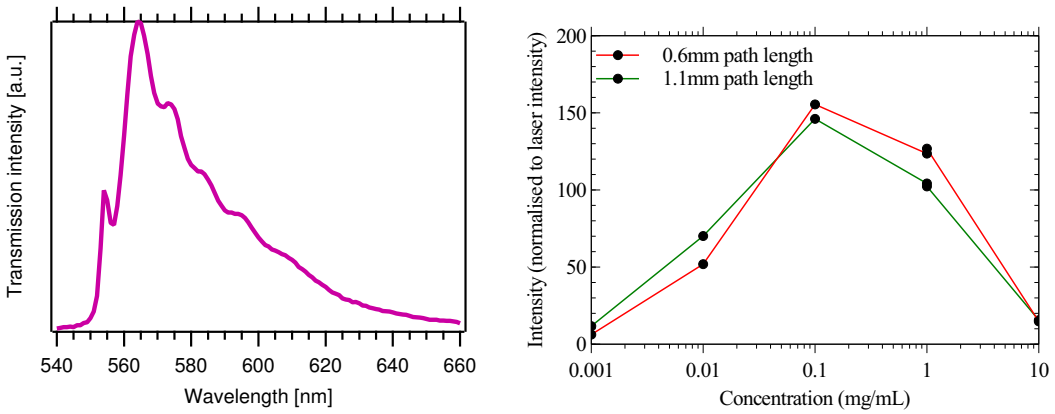


Figure 3.3: Left: example UV-vis spectra of Rhodamine 6G dye dissolved in methanol. Right: a plot graphing the intensity of that these spectra as a function of concentration.

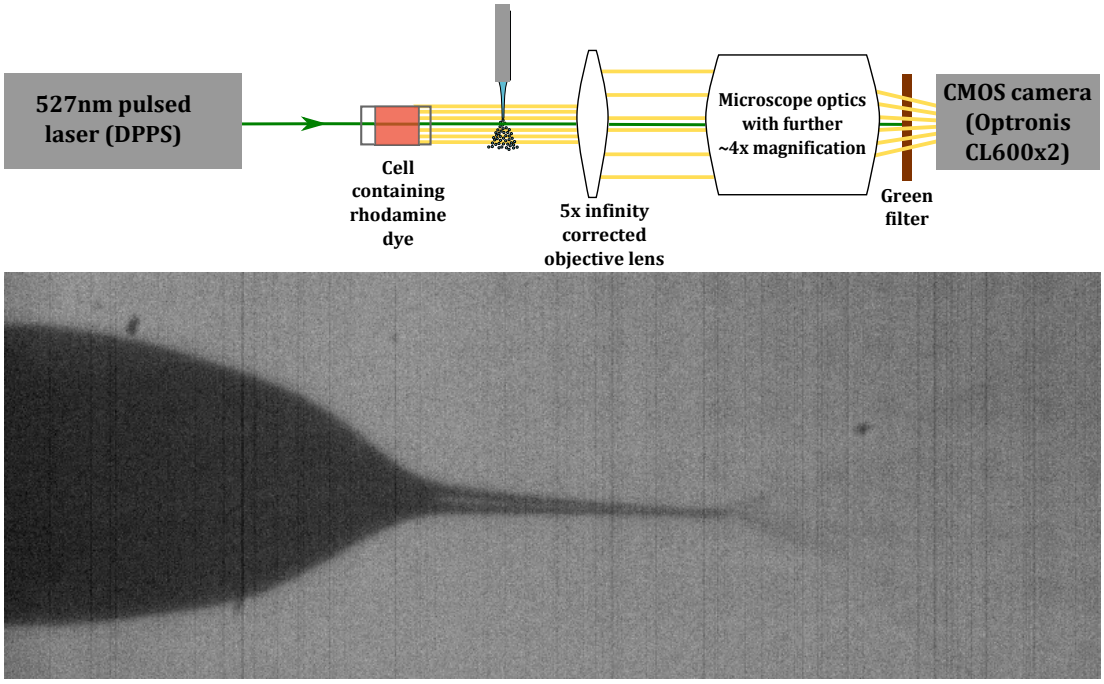
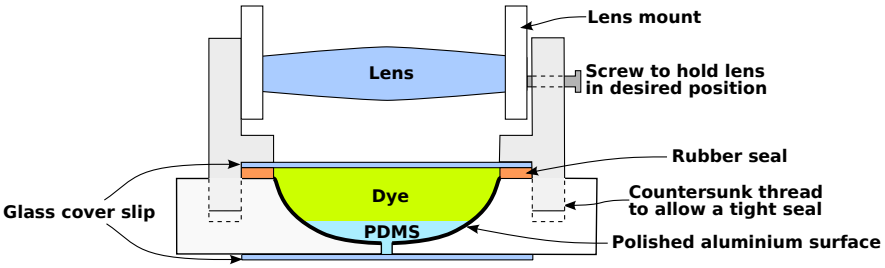


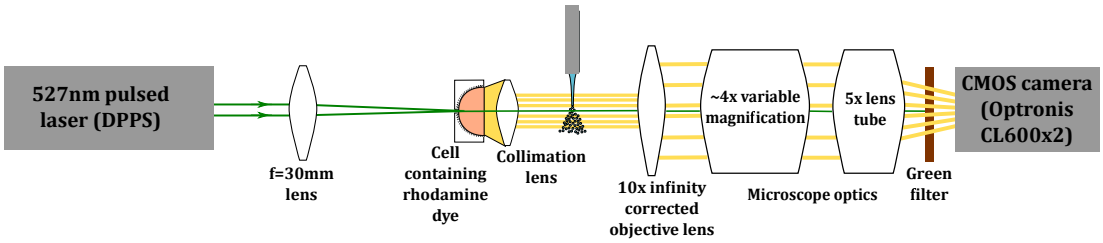
Figure 3.4: Optical system and example image collected using our original fluorescence back-light set-up.

shown in Figure 3.5b. The cell, which was refillable, was about 3 cm square and is designed to hold a small quantity of dye between two glass cover slips with a reflector to maximise the forward light output. The design allowed it to be coupled to a lens to improve the collimation of the light. Transparent PDMS was used to fill part of the volume ensuring the laser induced the fluorescence in the centre of the cell (within the reflector). The laser light was focussed through the pin hole on the back end of the cell using adjustable mirrors and a lens.

The electrospray ionisation source was set-up slightly differently compared to when used for deposition in order to try and produce the most stable spray possible. Firstly, the emmitter was in a vertical orientation pointing down - for electrospray deposition this is unfavourable as there is a risk of large drops falling from the emmitter into the vacuum system. However, in this case, the vertical orientation ensured the cylindrical symmetry of the system was not distorted by gravity. The liquid was gravity fed into the emitter capillary in order to provide a continuous backing pressure, as opposed to the repetitive pulsing from the stepper motors in a syringe pump. The height of the liquid reservoir was set so that the liquid only flowed out of the emitter when the high voltage was applied. The emitter was also clamped near its exit so it was unable to move as originally the emitter recoiled when liquid was ejected (visible in the high speed video footage).



(a) Dye cell design



(b) Optical setup

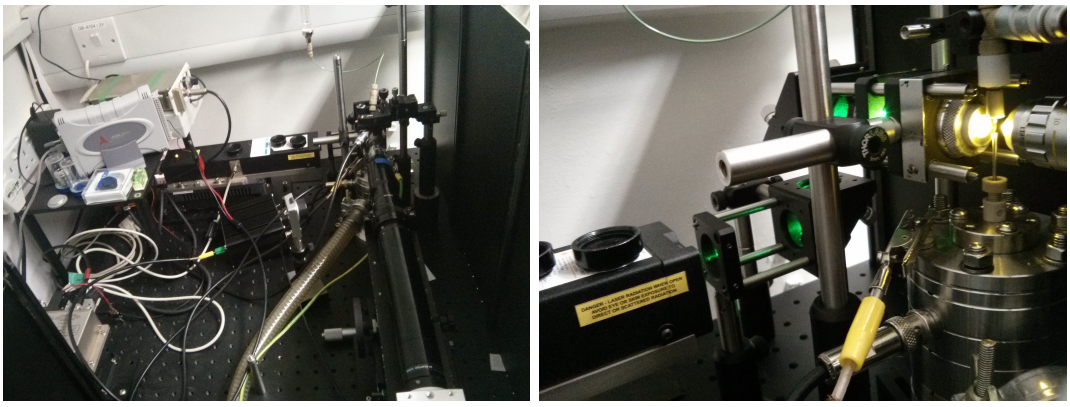


Figure 3.5: Final microscope setup based around a custom dye cell.

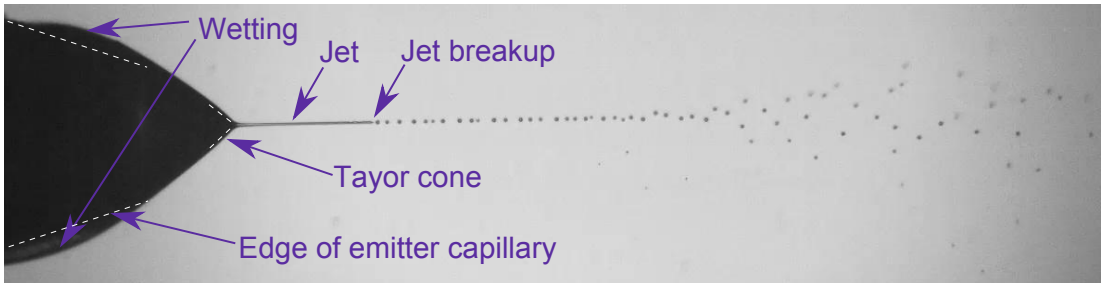


Figure 3.6: Example image showing the stable cone-jet mode of fluorescein dye in methanol. Key features are annotated

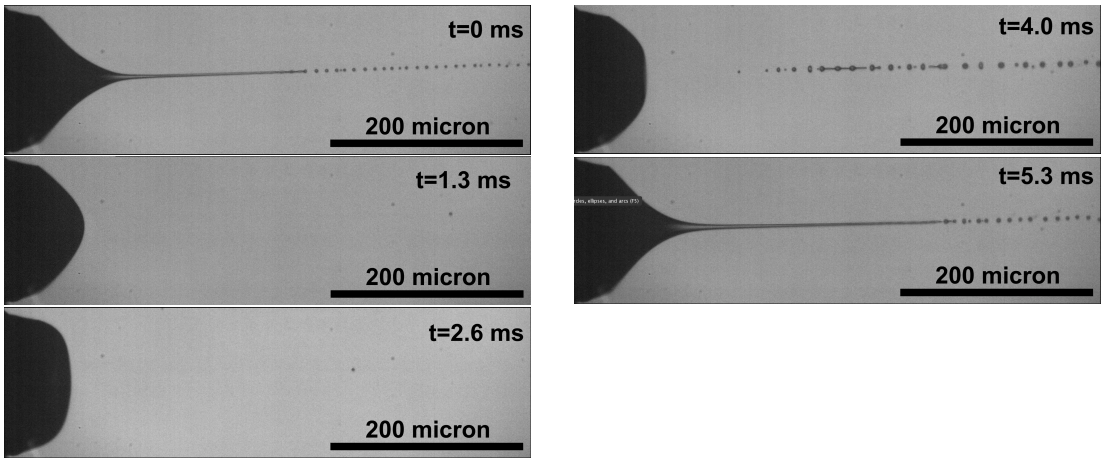


Figure 3.7: Subsequent frames captured showing the pulsing cone-jet regime of fluorescein dye dissolved in methanol.

3.1.4 Example images

The optics used had the capability to illuminate and image fields of views from 2 mm down to 100 µm and produce incredibly sharp images of micron sized objects. Figure 3.6 shows an frame captured at 1000 fps showing the cone-jet electrospray ionisation mode of methanol. At these frame rates, up to the fastest the instrument could measure (7000 fps), no feature of stable electrospray emission can be tracked from one frame to the next - each image needs to be treated as an entirely independent snapshot. Longer time-scale phenomena were resolvable such as the pulsing mode where pulses of cone-jet emission is not constant and turns on and off every 5 frames (5 ms) - see Figure 3.7 for an example.

Both of these examples are of methanol which was selected as it is very easy to spray. The main challenge in capturing these the images was controlling the wetting of the methanol on the emitter. The most probable outcome is the methanol would wet unevenly around the emitter causing the spray to veer off to the opposite side of the liquid build-up (due to electrostatic repulsion). To avoid

this, pure water was tried which has a much higher surface tension reducing its wetting ability. This was very difficult to spray but when it worked it worked very well. Figures 3.8 and 3.9 present example images of the jet-breakup of water, in the stable cone-jet regime, which highlight the capabilities of the imaging system.

The images selected in Figure 3.8 all show droplet explosions that look very like the picture described by the charge residue model (CRM - see Chapter 1.5.2) - these features are circled in the figure. Figure 3.9 shows even higher magnification images of the initial jet breakup process. These sorts of images are easily of high enough quality to use image processing to extract statistical information such as the size distributions of the drops if the field of view of the images were to be properly calibrated

Figure 3.10 shows an example of behaviour when the properties of the liquid are dramatically changed. NaCl was dissolved in methanol to a concentration of 0.5% (w.t.) to increase it's conductivity and was sprayed at $\sim$2 kV. The sorts of geometry seen bear little resemblance to the standard electrospray modes.

3.1.5 Discussion and conclusions

We have presented a highly capable ultra-fast exposure imaging system able of intensely illuminating a subject for sub 20 ns durations. This is many orders of magnitude shorter than a typical flash unit (typically $\sim$10 µs). This has been used to image the electrospray ionisation processes, across all relevant length-scales, providing images of sufficient quality to allow statistical analysis of drop size distributions, jet length etc. It has also allowed us to observe complex fluid mechanics processes, such as the geometry of jet breakup, producing high quality imagesthat have the potential to be united with theory and simulation work in the future.

Despite the high quality images, the electrospray experiments were unfortunately not pursued. We were unable to make the electrospray ionisation process repeatable enough to observe the same behaviour from the same parameters every time. Considerable effort was expended to control the system to insure all non-variables were held constant ensuring only the desired independent variable was changing. With low surface tension liquids, wetting was a problem that unfortunately was not overcome. For water, the more highly controlled the setup by ensuring the purity of the liquid, the cleanliness of the system etc., the harder it seemed to be able to get repeatable and stable spray parameters (voltage, distances, flow rate). It may be that the images presented here were made possible by imperfections in the experiment that were since eliminated, for example the

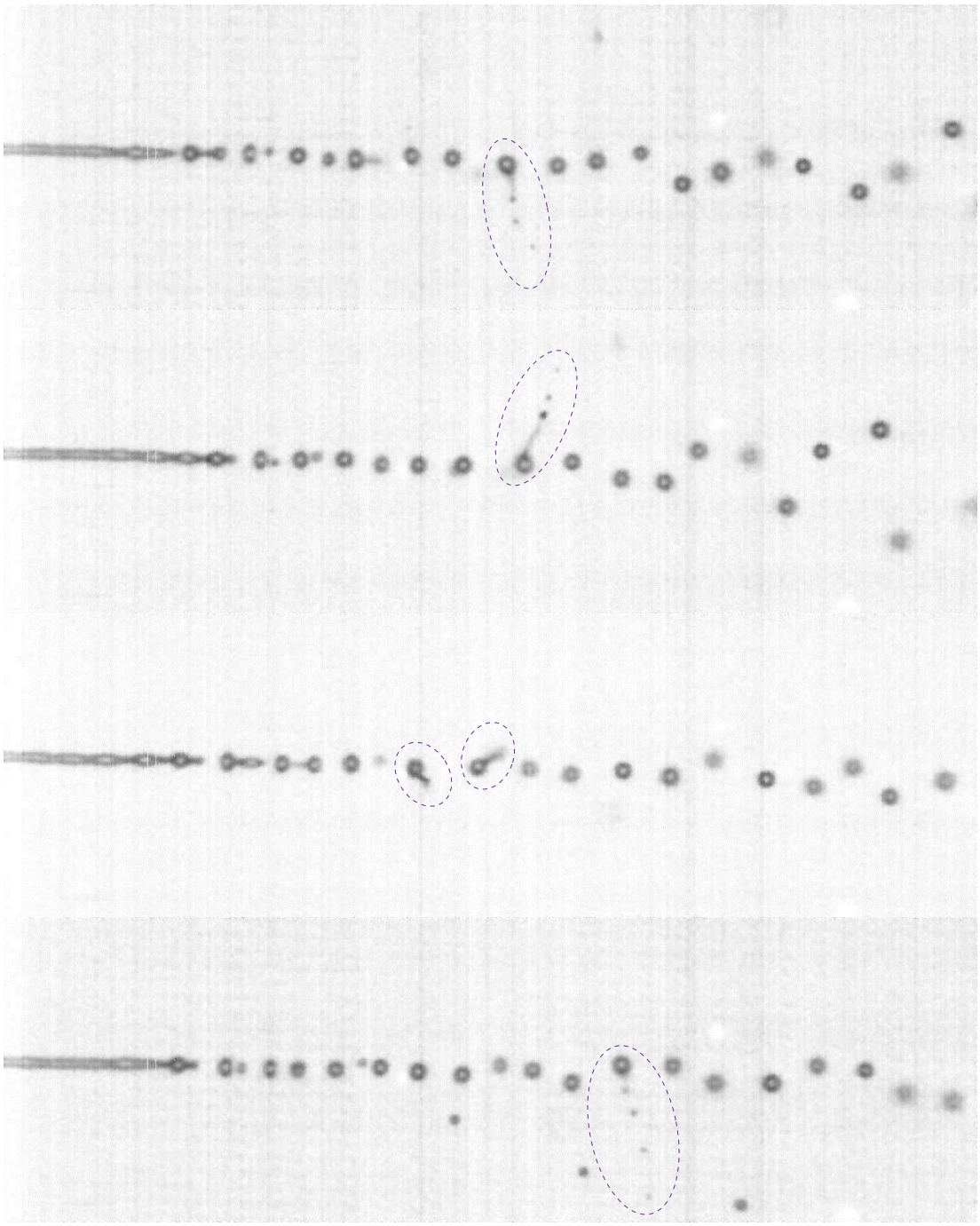


Figure 3.8: Example frames showing the drop breakup, via the charge residue model, of electrosprayed deionised water. Drops fissioning via CRM are circled.

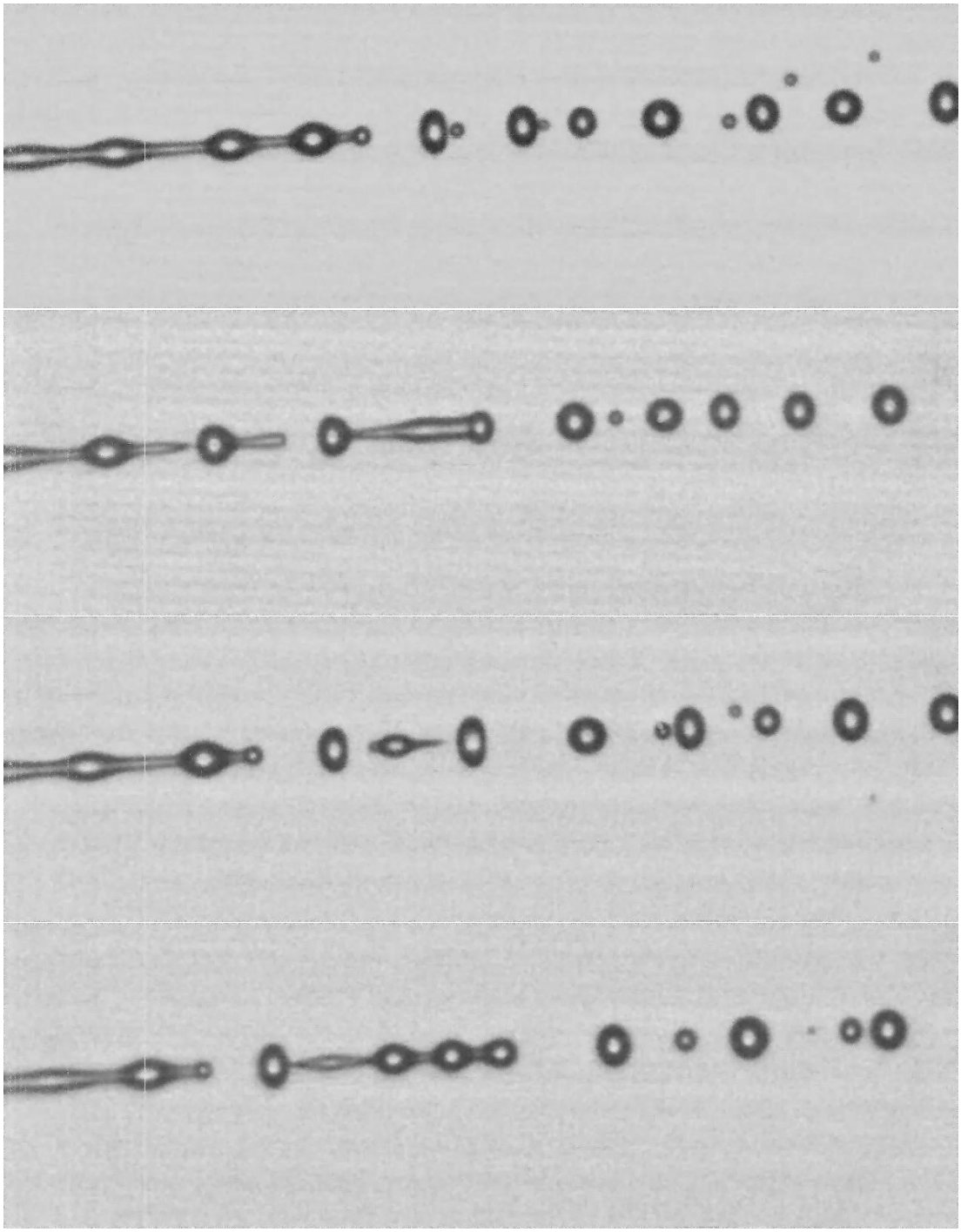


Figure 3.9: Frames showing the electrospray jet breakup of deionised water

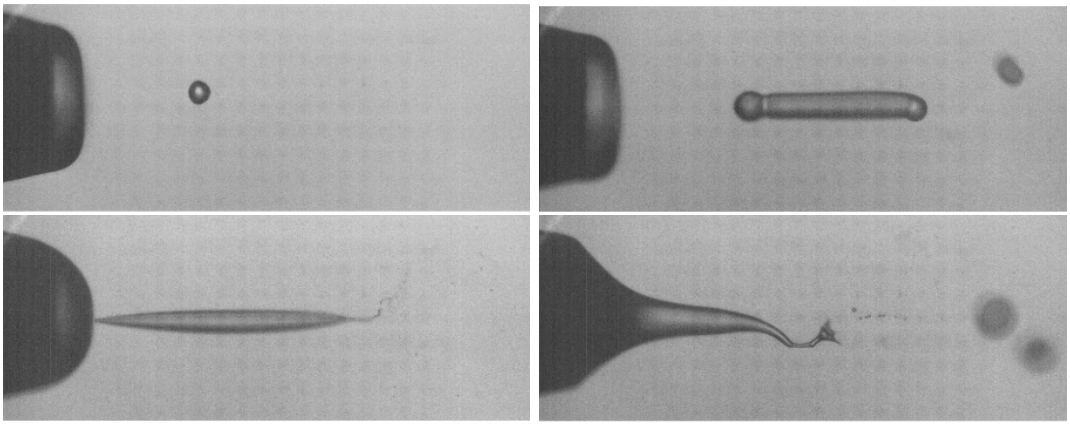


Figure 3.10: Frames showing the unusual electrospray ionisation behaviour of a concentrated (0.5 %w t) solution of NaCl in methanol.

purity of the liquid. It is also possible that finer control of distances, flow rate etc. are required or that working with a different style of electrospray emitter would aid future work.

3.2 Image charge detection

3.2.1 Introduction

Image charge detection mass spectrometry (CDMS) is an emerging technique that allows measurement of m/z as well as the charge of ions passing through the system from which the mass can be calculated. There are different variants on the technique [126–128], but all are based around passing the ions through a metal tube which is attached to a charge sensitive amplifier. This basic element is described in Figure 3.11. As an ion passes through the tube, and assuming it is long enough, an image charge equal to the charge of the ion builds up on the tube which can be measured as a voltage. The convention is to differentiate this voltage signal, from which the time-of-flight of the ions is known (the distance between peaks) allowing the velocity of the ions to be be calculated as the tube is of known length. By having two tubes separated with an accelerating stage in-between [126], m/z can be calculated by measuring the change in velocity when placed in an accelerating field.

3.2.2 Methods

We have taken the approach of Maze et al [129] who have taken just one of these elements to analyse electrosprayed droplets. Here, as well as the ToF, the

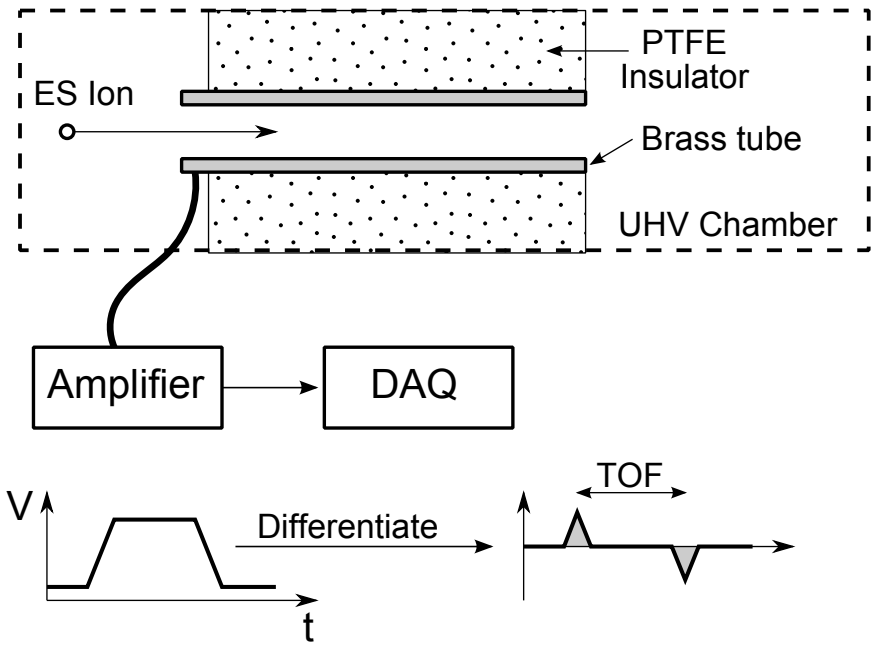


Figure 3.11: The operating principle of our home-built Image Charge Detection spectrometer. Electrospray ions pass through a metal tube of known length. An image charge of the ion builds up in the metal and is present whilst the ion is passing through it. The image charge on the tube can be measured using an amplifier and high speed data acquisition card. The duration between peaks of the differentiated signal indicates the time of flight and the area underneath them proportional to the charge.

authors also quantify the charge on the drops from the area under the peaks in the differentiated signal. This required calibration of the pre-amplifier using a known capacitance.

Example data from our first attempt at building such an instrument are shown in Figure 3.12. The instrument is simply a 50 mm long brass tube, held in a vacuum chamber using a PTFE insert, directly connected to a home built amplifier. The voltage output from the amplifier was measured using a National Instruments high speed data acquisition (DAQ) card. The chamber was placed on a vibration isolation table as the instrument is very sensitive to vibrations which predominantly came from vacuum pumps - careful consideration of the pumping was therefore required to minimise this. A small ion pump was used on the main chamber, whilst the turbomolecular pump, as is required for the 3rd differentially pumped stage of the electrospray source, was mounted separately and connected to the electrospray via bellows. The backing pumps were all connected via plastic tubing (metal tubing transmitted more vibrations).

Despite these efforts, vibrations from the pumps were never completely mitigated. In Figure 3.12, the sinusoidal background is attributed to vibrations from the turbomolecular pump - the oscillation period matches the frequency of the pump and the oscillations were not present with the pump turned off. Vibrations from the roughing pumps are much lower frequency so are less of a concern.

Also apparent in the data shown in Figure 3.12 is the shoulder on the left hand side of the transient. This is attributed to image charge build up on the wire used to connect the brass tubulation to the vacuum feed-through. Moving this wire to the other side of the device causes the shoulder to move to the other side of the transient. This artefact could easily be designed out of the instrument. It is also worth noting that the transients are not as sharp as those in the literature [129]. This is attributed to the lack of grounded apertures on the entrance and exit of the tube causing the image charge to prematurely build up on the tube just before the drop has entered it. Again, this is a trivial design problem to address.

Figure 3.13 shows another set of example data, this time for the negative bias mode hence the seemingly inverted data, showing the data processing used for the analysis. The data points, shown in black, are smoothed using a binomial algorithm. This is then differentiated (shown in green). Differentiating the unprocessed data made identifying the transients much more difficult as the differential signal was much noisier due to the high frequency noise. Applying various types of low pass filter showed similar results to the smoothing with no real advantage to justify the more computationally complex process. Time of flight was determined by measuring the time elapsed between the two peaks in

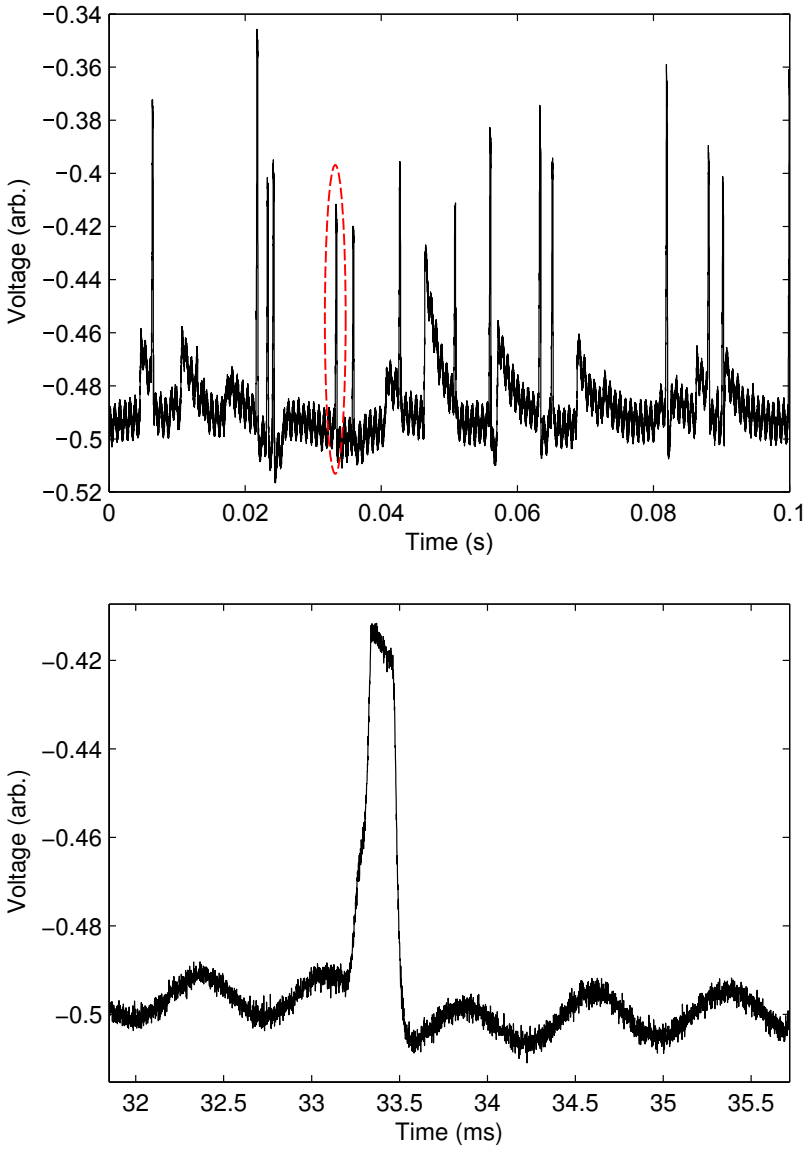


Figure 3.12: Example data collected using our image charge detector for a solution of fluorescein (dissolved in methanol) sprayed at 2.00 kV. The bottom plot zooms in on the transient marked in the top plot with a dotted circle.

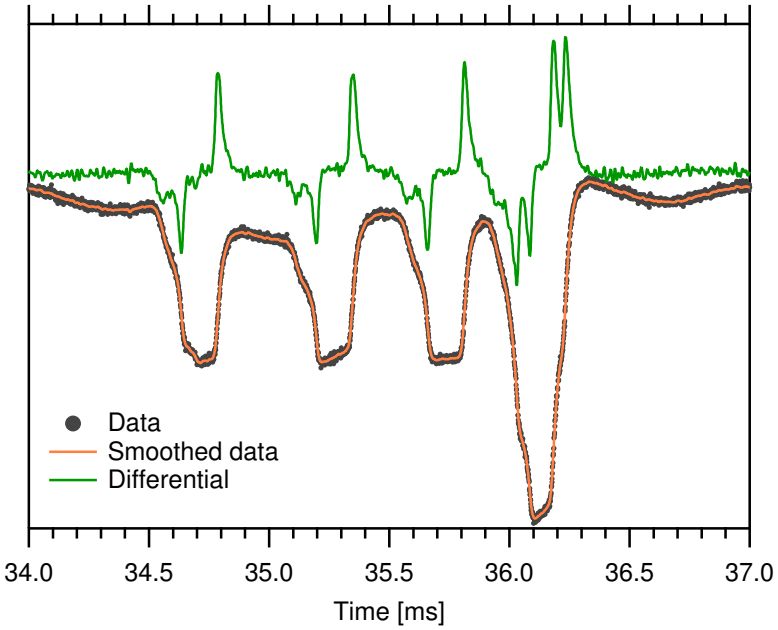


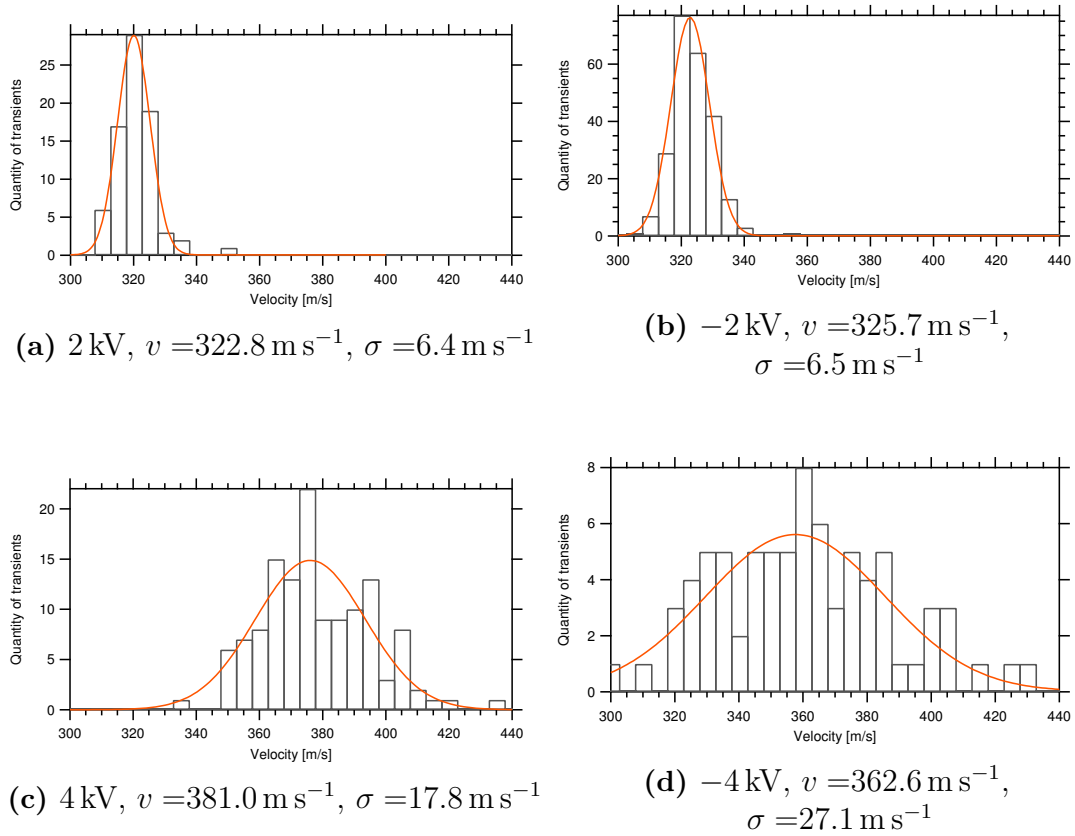
Figure 3.13: Example image charge detection data (black points) collected of fluorescein dye in methanol sprayed at −2.00 kV. For analysis, this data was smoothed and then differentiated as shown.

the differentiated signal corresponding to the leading and decaying edges of each transient.

Figure 3.13 shows three standard transients from electrospray ions passing through the tube sequentially followed by a fourth transient, at 36 ms, showing a double event where two ions enter the tube in quick succession so the two signals overlap. In this case the two ions likely have the same charge based on the identical peak heights in the differential signal. Analysis of the individual peaks on the leading edges is made difficult by the shoulder (caused by the wiring as previously discussed). To minimise these double (and higher order) events, the emmitter was withdrawn to a larger distance than usual and misaligned to minimise the throughput into the entrance capillary.

3.2.3 Velocity distributions

Figure 3.14 shows four histograms of the distribution of velocities measured for different spray biases (±2.00 kV and ±4.00 kV). In all cases, a 0.1 % solution of fluorescein in methanol was used. In each case, measurements were taken for 0.5 s, during which a statistically significant number of transients were recorded. The width of the transients was measured using a semi-automated process looking at the separation of peaks in the differential of the voltage signal from the pre-



(a) 2 kV, v =322.8 m s^{-1}, σ =6.4 m s^{-1}

(b) −2 kV, v =325.7 m s^{-1}, σ =6.5 m s^{-1}

(c) 4 kV, v =381.0 m s^{-1}, σ =17.8 m s^{-1}

(d) −4 kV, v =362.6 m s^{-1}, σ =27.1 m s^{-1}

Figure 3.14: Velocity distributions for fluorescein sprayed from methanol at ±2 kV and ±4 kV. The values quoted as v and σ represent the mean and standard deviation measured from the data (used to plot the Gaussian distributions shown). All histogram bins have width of 5 m s^{-1}.

amplifier. A Gaussian distribution is also shown with the histograms generated from the mean and standard deviation of the velocity values (listed in the figure captions).

The plots showing 2 kV and −2 kV both show very similar distributions centred at ∼320 m s^{-1} with each with a full width at half maximum of 12 m s^{-1} and 14 m s^{-1} respectively. The histograms for 4 kV and −4 kV are significantly broader. The distributions, centred at 381 m s^{-1} and 363 m s^{-1} have widths (again FWHM) of 42 m s^{-1} and 63 m s^{-1}. When processing the data, qualitatively it was obvious that for the ±2 kV dataset, each transient was of a very comparable image charge due to their highly repeatable shape. For ±4 kV, there was a huge variation in charges. This may go some way to explain the much broader velocity distribution for the high voltage case. It is however clear that the higher bias does seem to be increasing the velocity of the ions. Although it makes sense that for a higher capillary voltage/lager electric field to accelerate the ions to greater velocity prior

to entry into the inlet, in this system one would expect the velocity of the ions to be dominated by free jet expansion (see Chapter 1.6.1).

3.2.4 Conclusions

Data has been presented from a preliminary instrument with the capability to measure the charge and velocity distributions of a molecular ion beam in UHV. The instrument has been used to successfully measure the velocity distribution of fluorescein sprayed from methanol using biasses of $\pm 2\,\mathrm{kV}$ and $\pm 4\,\mathrm{kV}$, although we would be hesitant to quote any definitive velocity values from this data. Firstly, not many events were counted and repeat measurements have not been carried out. Secondly, it is worth noting that the velocities measured here are somewhat of a lower limit due to the lack of apertures on the entrance and exit to the tube which would likely have a broadening effect of the transient increasing the measured time of flight.

Regrettably quantitative charge information is not included as the pre-amplifier has yet to be calibrated - this data was intended to be a proof-of-concept to confirm the dimensions of the tube, capabilities of the amplifier and acquisition setup and to highlight any experimental issues. The data collected served this purpose well and led to a modified instrument, which has been built implementing the design suggestions discussed. This instrument has therefore lead the way for future studies such as investigating the optimal geometry in the first pumping state of the UHV-4 system (where adiabatic expansion dominates - see Chapter 1.6.1). Furthermore, measurements of velocity and charge are expected to aid the future development of ion optics into the electrospray instrument where knowing the charge and velocity of ions would be of huge benefit.

Chapter 4

Suitability of electrospray deposition for the fabrication of molecular electronic devices

4.1 Introduction

Vacuum electrospray deposition (ESD) is an emerging technique that has allowed researchers to study complex molecules on surfaces, *in-situ*, using a vast array of analytical techniques requiring high vacuum including various photoemission [4, 6, 36] and scanning probe techniques [71, 83]. Early examples of work using high vacuum ESD studied the bonding of molecules used in dye sensitised solar cells such as the benchmark "N3" sensitiser dye on the titanium dioxide surface [4]. The technique has also been applied beyond traditional surface science experiments and used with biological systems [62, 89]. In recent years molecular photovoltaics, such as organic solar cells, are increasingly reliant on the construction of multilayer and bulk heterojunction structures [25, 32]. Ambient electrospray deposition has been used as a tool to construct such structures [130] providing a pathway to use high vacuum electrospray to study critical parts of such devices *in-situ*.

Electrospray deposition relies on the formation of a beam of molecular ions via the electrospray ionisation process. This has been thoroughly discussed elsewhere [47, 82, 131], but in summary, a fluid is passed through a small capillary tube with a large voltage ($\sim$ kV) applied to it. The voltage causes the liquid emerging from the capillary to be drawn into a well-defined shape known as a Taylor cone - at the tip of which the charge on the liquid is so high a jet of liquid is expelled. Due to the charge on the liquid's surface, the jet pinches off into a stream of droplets which in turn repeatedly fission into ever smaller drops. This plume of

ionised droplets can be fired into a differentially pumped vacuum system where a series of apertures allow the pressure to be reduced to high vacuum conditions whilst skimming the ionised droplets, from which solvent is evaporating, into a narrowly diverging beam of molecular ions. Placing a surface in the path of this beam allows a film of the solute to be grown on the surface with minimal solvent contamination.

4.2 Instrumentation

The ESD system used was a Molecularspray UHV4 (a schematic is shown in Figure 4.1a). This portable deposition source consisted of a 250 µm inlet capillary, 0.4 mm and 0.6 mm skimmer cones separating the first two vacuum stages (pumped using roughing pumps) from the 3rd vacuum stage pumped using a turbomolecular pump. The exit from the instrument was a 1 mm aperture. The deposition chamber, pumped using a turbomolecular pump, had a base pressure of 1×10^{-7} mbar and a deposition pressure of 1×10^{-6} mbar. The depositions were monitored by observing fluctuations in the pressure and the inlet capillary was flushed regularly (with the valve to the deposition chamber closed) to avoid clogging/blockages from the sprayed molecules.

The solutions were fed into the emitter capillary (New Objective Stainless Steel TaperTip) by a syringe pump delivering a flow rate of $0.3\,\mathrm{ml\,h^{-1}}$. Before each deposition the emitter, syringe and tubing were thoroughly flushed with solvent. ∼2 kV was supplied to the emitter with respect to the grounded entrance capillary.

Time-of-flight secondary ion mass spectrometry (ToF-SIMS) was used as an imaging technique. ToF-SIMS utilises ion sputtering to lift fragments off the surface whilst a time of flight mass spectrometer measures mass spectra of the fragments. These spectra can be collected as a function of time and/or space in the x,y plane of the sample. This allows chemical maps of the sample to be constructed, in which each pixel represents a full mass spectrum, making it the ideal technique imaging sub millimetre structures with chemical contrast. The instrument used was an ToF-SIMS IV instrument (IONTOF GmbH) with a 25 keV Bi primary ion source (with a Bi_3^+ cluster beam applied). The primary ion dose was kept below the static limit and an electron flood gun (<20 eV) was used to prevent charging.

X-ray photoelectron spectroscopy (XPS) was used to provide chemical analysis of thin films and bulk samples. By irradiating a sample with X-ray photons, electrons are emitted from the sample into the vacuum (the photoelectric effect).

By measuring the kinetic energy of these emitted photoelectrons, the original binding energy of the electrons can be determined meaning XPS is sensitive to the chemical environment of electrons. XPS therefore allows quantitative measurements of blends of molecules that may contain the same elements existing in different chemical states, and due to its high surface sensitivity (limited to the nanometre range by the escape depth of the photoelectrons), XPS is ideal for studying the chemistry of thin films. In this study, a Kratos Axis Ultra instrument was used with a monochromotised aluminium K_α X-ray source. Charge neutralisation was provided using an electron flood gun. The analyser was set to measure in hybrid mode with a pass energy of 20 eV.

The molecules and solutions used for each of the three experiments are detailed in their respective sections. All were purchased from Sigma Aldrich.

4.3 Methods, results and discussion

4.3.1 Layered deposits of molecules from the same solvent

Multilayer structures of different organic materials are critical in the construction of range of a devices including Bragg reflectors [132], photovoltaic devices such as organic solar cells [25], and drug delivery systems [133]. Techniques like spin casting provide the capability to build high quality multilayer structures from molecules that are compatible with different solvents: Bailey et al have shown, using ToF-SIMS, that alternate spin cast layers of polystyrene (PS) and polyvinylpyrrolidone (PVP) dissolved in toluene and water respectively, can produce multilayer structures that have highly repeatable layer thickness and sharp interfaces [134]. However, these traditional wet chemistry preparation methods are limited to the use of materials dissolved in orthogonal solvents (solvents that will dissolve one species but not another). Solvent free techniques, such as electrospray deposition, provide a potential solution to overcoming this experimental limitation.

A silicon wafer substrate was cleaned via ultrasonication in acetone, methanol and isopropanol. Thin films of fluorescein dye followed by polyvinylpyrrolidone (PVP) were deposited using electrospray onto the passive oxide surface. Both molecules were dissolved in methanol to a concentration of 0.1 % (w.t) and further diluted to 0.05 % (w.t) for deposition. Each deposition lasted an hour and the sample, which was held on a transfer arm 0.5 m away from the exit aperture of the UHV4, was moved slightly between depositions; both depositions were therefore visible but with an overlapping area.

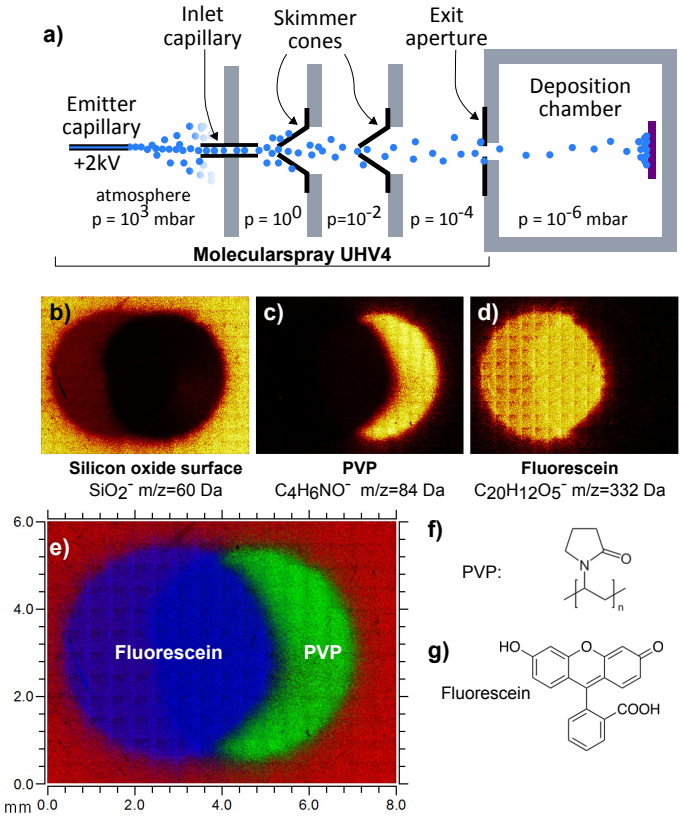


Figure 4.1: a) Schematic of the Molecularspray UHV4 system used to fabricate bi-layer structures. b-d) ToF-SIMS images built using markers for SiO_2, PVP and fluorescein respectively. e) Composite image using the above 3 markers shown in red, green and blue respectively. f-g) chemical structure of PVP and fluorescein.

ToF-SIMs was used to image this fluorescein/PVP bi-layer on the silicon oxide surface. Figure 4.1b-d shows secondary ion images constructed from the intensity of individual peaks in the mass spectra selected as markers for the surface and each molecule. A composite image showing the intensity of the different markers is also included in Figure 4.1e. These images show there is minimal mixing between the layers where the PVP film appears on top of the fluorescein deposit eclipsing the image of the fluorescein (Figure 4.1c) with little signal attributed to the fluorescein in this region. Although, the depositions were very thin, some preliminary depth profiling experiments illustrated the presence of underlying fluorescein (data not shown).

4.3.2 Deposition of immiscible polymer blends

Producing a film containing a blend of molecules from orthogonal solvents can be an experimentally challenging problem. Electrospray deposition provides a

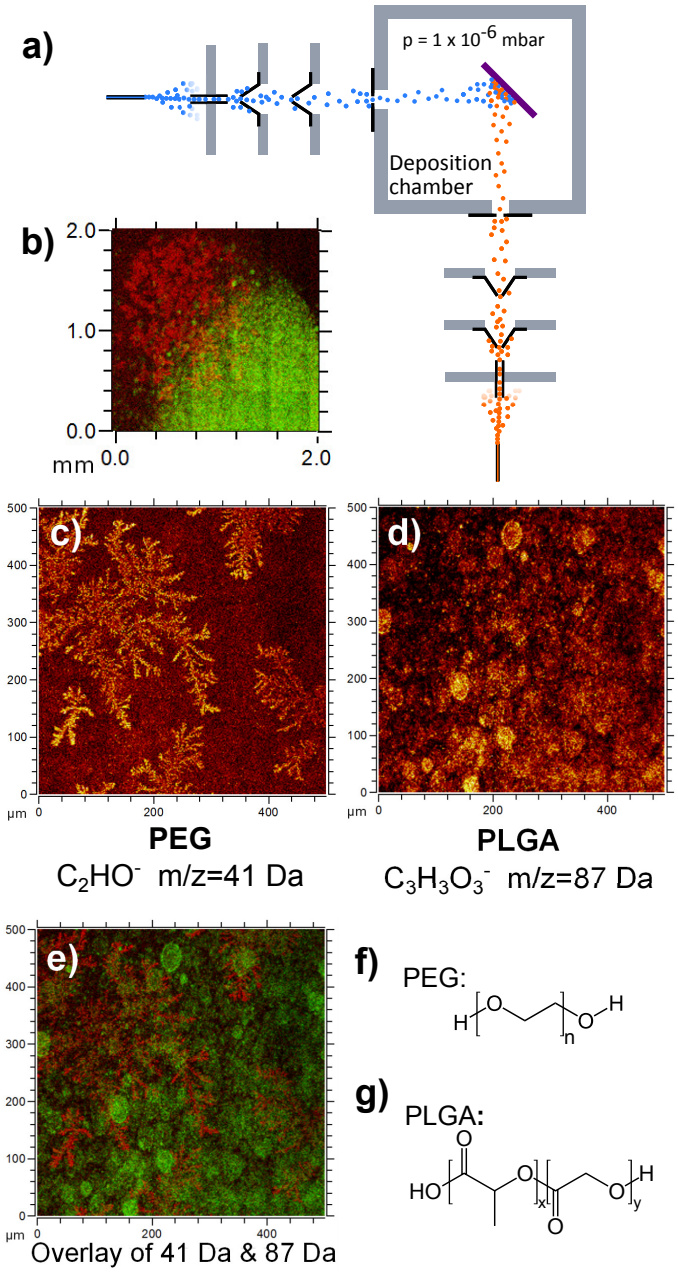


Figure 4.2: a) Geometry used to co-deposit molecules from two solutions using two Molecularspray UHV4 systems. b) ToF-SIMS composite image showing the markers for PEG (red) and PLGA (green). c-e) high resolution images of the overlap region for each of the two markers a composite respectively. f-g) show the chemical structure of PEG and PLGA.

potential solution; as there should be minimal amounts of solvent, simultaneous depositions of the two molecules from different electrospray sources should allow the mixing of the molecules at the surface. This was attempted using the setup shown in Figure 4.2a. Two electrospray sources, of the type used in section 4.3.1,

were placed at 0° and 90° to each other with the sample at 45°. The sources were 8 cm from the surface. It was not possible to monitor the pressure in the chamber during deposition but the system was allowed to pump down sufficiently that the ultimate deposition pressure of $\sim 1 \times 10^{-6}$ mbar was achieved.

The two polymers used were poly(lactic-co-glycolic acid) (PLGA) and Polyethylene glycol (PEG) dissolved in acetone and methanol respectively to a concentration of 0.1 % (w.t.). The PLGA, a co-polymer, had a ratio of 65:35 for the lactide:glycolide monomer components. PLGA and PEG were co-deposited for around 1 hour onto clean silicon wafer (ultrasonicated in acetone, methanol and isopropanol) and the resulting deposition was imaged using ToF-SIMS. A sample of the images collected are shown in Figure 4.2. The two diagnostic secondary ions used are $m/z = 41$ (C_2HO^-) for PEG and $m/z = 87$ ($C_3H_3O_3^-$) for PLGA. A 2 mm area overlay image is shown in Figure 4.2b illustrating the overlapping deposits. A 500 µm area within the overlap region is shown for the PEG and PLGA markers and as an overlay in Figures 4.2c 4.2d and 4.2e respectively. Secondary ion images were also measured away from the overlapping region in areas containing each individual species which showed comparable morphologies.

Firstly it is clear that in the overlapping region there has been some mixing of the two components. The PEG has also formed a large scale fractal structure on the surface. This behaviour implies the molecule is mobile on the surface, which, considering the size of the PEG polymer chains, implies there is likely a small amount of solvent on the surface allowing such structures to form. The same argument could also be made for the "blob" like structure of the PLGA.

Although acetone and methanol are miscible, when the two solutions were mixed, the mixture turned cloudy as the molecules partially drop out of solution. The same experiment does however have the potential to be applied to completely immiscible polymer solutions, for example those soluble exclusively in water and toluene.

4.3.3 Miscible polymer blends for organic photovoltaics

The polymer blend PEDOT:PSS is used in organic photovoltaic devices as a hole conducting layer. It contains a mixture of poly(3,4-ethylenedioxythiophene) and polystyrene sulfonate as shown in Figure 4.3d and 4.3e. Here XPS was used to compare films of PEDOT:PSS deposited using electrospray deposition and the more traditional spin casting directly from solution.

Gold substrates were made by thermally evaporating 10 nm of titanium and 100 nm gold onto silicon wafer. The titanium was used to improve cohesion

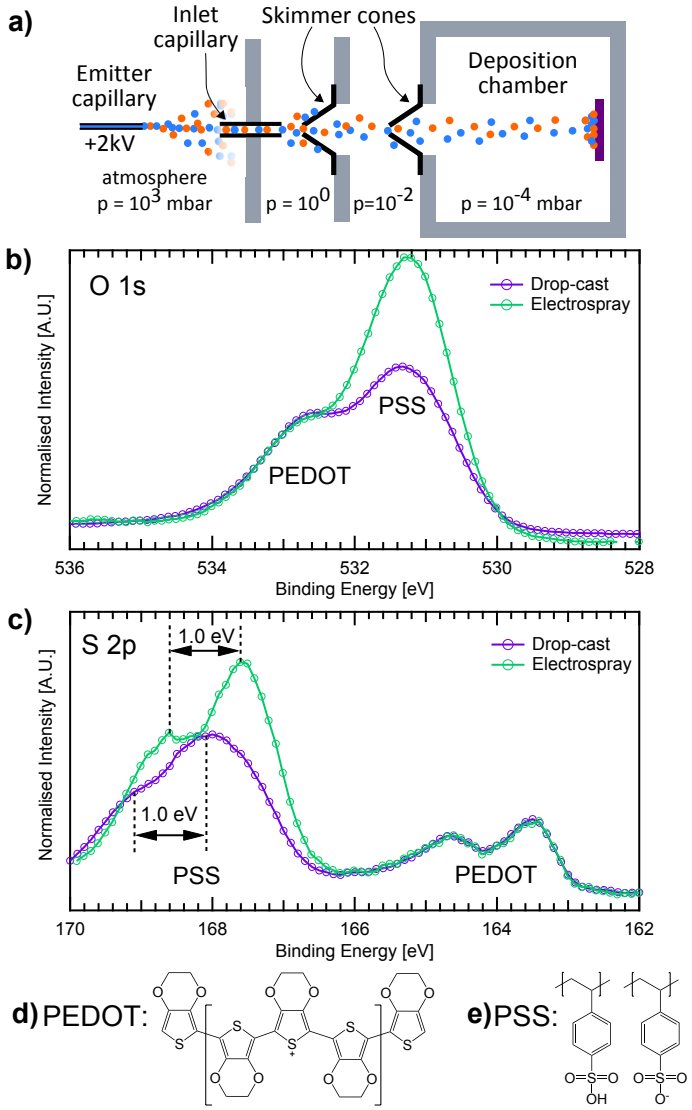


Figure 4.3: a) The electrospray deposition source used to deposit PEDOT:PSS consisted of one less pumping stage than the UHV4 source used in the previous sections. b-c) show O 1*s* and S 2*p* XPS measurements for an electrospray deposited sample and a drop cast sample of the same solution. d-e) show the two components of the PEDOT:PSS polymer blend. PSS is a co-polymer of the two groups shown.

between the gold film and the silicon oxide surface. The silicon wafer was cleaned by ultrasonication in acetone, methanol and isopropanol prior to evaporation. PEDOT:PSS (dry re-dispersible pellets from Sigma Aldrich), was dissolved in deionised water and drop cast onto one substrate. This solution was diluted to 0.01 % (w.t.) and electrosprayed onto another substrate using the apparatus shown in Figure 4.3a. This apparatus contained one fewer pumping stage than the Molecularspray UHV4 (as used in Sections 4.3.1 and 4.3.2) to maximise deposition

flux as low pressures and desolvation were less critical. 10 % methanol added to the solution to improve the quality of the spray.

Figures 4.3b shows XPS measurements of the O 1s region for both the drop cast and electrospray deposition samples (both were prepared ex-situ). The O 1s spectra contains two overlapping peaks that have been attributed to the ethylenedioxy attachment to the thiophene ring of the PEDOT at higher binding energy and the sulfonate side group of the PSS at lower binding energy. Both spectra have been normalised to the PEDOT/thiophene shoulder. There is a clear increase of the PSS/sulfonate contribution for the electrosprayed sample.

Figure 4.3c shows XPS spectra of the S 2p region (measured at the same position on both samples as the O 1s data). There are two doublets resulting from the spin orbit splitting of the 2p states of sulphur in the PEDOT and PSS molecules. These have been attributed the lower binding energy doublet to the sulphur PEDOT's thiophene ring and the much broader feature at higher binding energy to the sulfonate group of the PSS. Again, both spectra are normalised to the PEDOT contribution and there is a clear increase in PSS signal for the electrosprayed sample.

The broadening and binding energy shift of the sulfonate peaks of the drop cast relative to the ESD sample is attributed to charging effects due to the thickness of the drop cast deposit. This could only be present in the PSS and not the PEDOT as the PEDOT is a fully conjugated conductive polymer. Measurement at different sample positions shows the same feature shapes and there was no sign of beam damage between the start and end measurements at a single position.

It is worth noting that two polymers in the PEDOT:PSS blend are individually charged. As shown in Figures 4.3d 4.3e, PEDOT has positive charges on the thiophene backbone whilst PSS has negative charged sulfonate groups. It is possible this could explains why the electrospray technique would preferentially deposit one species over the other - however in this case the experiment was carried out in the positive bias mode and we are seeing potential preferential ionisation of the negative species which is counter-intuitive.

Analysis of the C 1s was hindered by atmospheric carbon contamination (during transport of the samples from the deposition apparatus to the XPS instrument) so is not included here. Carbon spectra were used to provide relative calibration between the two samples where the low binding energy edge of the C 1s region implies a 0.9 eV shift between the two samples. This offset was applied to all the included spectra.

4.4 Summary and conclusions

Three experiments were presented highlighting the capabilities and potential concerns of using electrospray to produce multi-layered structures and blends of materials. Firstly, it has been shown that the solvent contamination on the surface is low enough to build up thin layers of molecules that are compatible with the same solvents without substantial mixing of the films. However, the UHV4 system is not well suited to building up thick deposits and although SIMS is surface sensitive enough to measure surface coverage, conventional sputtering does not allow depth profiling of such thin films (when probed with XPS we find similar deposits are several monolayers thick). With the co-deposition experiment it has been shown there is almost certainly a small solvent contribution to the deposit allowing structure to form on the surface. More sophisticated electrospray instruments have applied techniques such as mass selection and heated inlet capillaries to attempt to combat these issues.

The XPS analysis of the PEDOT:PSS blend is of importance and certainly needs further study. It appears as though the electrospray deposition process preferentially ends up with one species over another being ionised, entering the vacuum system and landing on the surface. Although SIMS has been used to show that a simple UHV4 style electrospray source can be utilised to build the sort of films used in molecular devices, care should be taken if simultaneously depositing multiple species.

Chapter 5

Adsorption and charge transfer interactions of bi-isonicotinic acid on Ag(111)

5.1 Introduction

Understanding the charge transfer of electrons between molecules and surfaces is of critical importance to understanding the operation of molecular devices such as dye-sensitised solar cells [4, 39] and water splitting photoelectrochemical cells [38], and a wide range of molecular electronics. The charge transfer dynamics from a molecule to a surface has been probed on the low femtosecond (fs) time-scale using the core-hole clock implementation of resonant photoemission (RPES), which uses the core-hole decay channels to determine the degree of localization of a resonantly excited core-electron in an unoccupied valence state compared to the core-hole lifetime (typically a few fs). The underlying principle of this technique is to measure the electrons emitted from the core-hole decay process in which the originally excited electron is a direct participant. Charge transfer on the time-scale of the core-hole lifetime is then inferred by the depletion of this core-hole decay channel. Charge transfer in the other direction, from the surface to the molecule, can be probed by a similar approach where the electrons emitted from the core-hole decay process in which the electron transferred from the surface into the lowest unoccupied molecular orbital (LUMO) of the core-excited molecule are measured. This has been previously studied this phenomenon [11, 33, 36], attributing the observed features in the resonant core spectroscopy to either *super-Auger* or *super-spectator* decay [33], where electrons that have transferred from a surface into the LUMO are directly involved in the Auger-like core-hole decay, with or

without a simultaneous transfer of a core-excited electron into the empty density of states of the surface above the Fermi level, respectively. Molecules studied using this method range from fullerenes [33], which can be used in organic photovoltaic devices as an electron acceptor [135], to bi-isonicotinic acid [11], the ligand of the "N3" molecule used in dye sensitised solar cells [136]. Although bi-isonicotinic acid is largely responsible for the bonding between N3 and the titanium dioxide surface in a dye-sensitised solar cell [4] and does itself show evidence of charge transfer between the molecule and a gold surface in both directions [11], N3 has been shown not to exhibit any super-spectator/super-Auger decay due to the geometry of the molecules on the gold surface reducing the spatial overlap of the relevant orbitals and preventing surface-molecule charge transfer [36].

In these examples of super-spectator/super-Auger decay [33, 11], electrons are able to transfer from the metal into the molecule because the LUMO of the core-excited molecule partially overlaps energetically with the Fermi level of the metal surface in the core excited state. This study examines the system of bi-isonicotinic acid on a Ag(111) surface, where the LUMO lies entirely below the Fermi level (in the core excited state) which could, in principle, increase the number of electrons transferred and made available to participate in the super-spectator/super-Auger decay.

5.2 Method

Measurements were carried out at the I311 beamlime [124] on the MAX-II storage ring at *MAX-Lab*, Sweden. This undulator-based beamline has an energy range of $30 - 1500$ eV and was configured to give an energy resolution of 5 meV to 150 meV between 50 eV and 600 eV. The light produced by this beamline was highly elliptically polarized to the extent the polarization was considered linear. The spot of light incident onto the sample had an approximate size of 0.5 mm $\times$ 0.1 mm. The endstation was equipped with an upgraded *Scienta* SES200 hemispherical electron analyser where a straight slit with width 0.8 mm was used giving an analyser resolution of 10 meV and 100 meV for pass energies 20 eV and 50 eV respectively. The base pressures in the preparation and analysis chambers were 1×10^{-9} mbar and 1×10^{-10} mbar, respectively. A single crystal of Ag(111) was mounted on a loop tungsten wire that enabled resistive heating of the sample and a thermocouple junction was spot welded to the side of crystal allowing temperature measurement. The crystal was cleaned using 1 kV Ar^+ ion sputtering and $\sim$550 °C anneal cycles until there was no C 1*s* peak visible in the XPS spectra

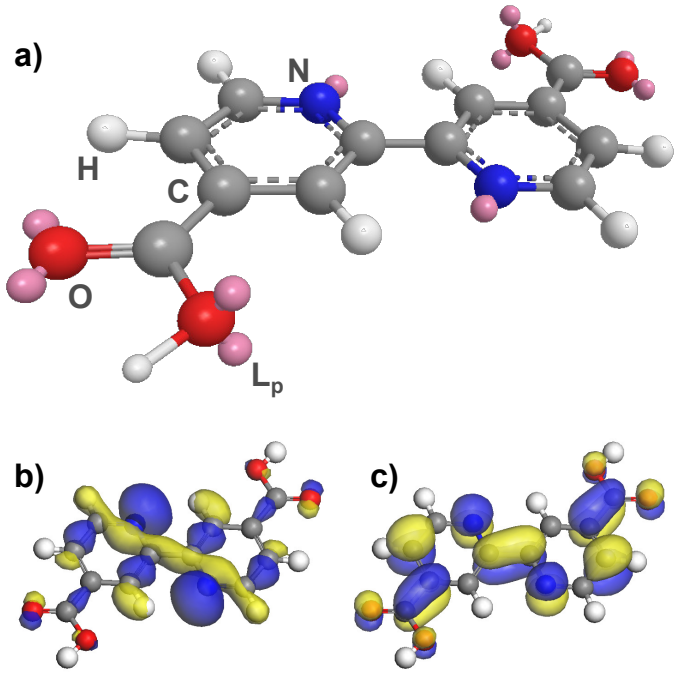


Figure 5.1: Bi-isonicotinic acid (4,4'-dicarboxy-2,2'-bipyridine). Bond angles, lengths etc show the lowest energy configuration of the molecule in the gas phase. Gray, blue, red and white balls represent carbon, nitrogen, oxygen and hydrogen atoms respectively. Lone pair electrons (L_p) are indicated in pink. The bottom left and right figures show the location of the HOMO and LUMO orbitals (Geometry and orbitals simulated using the DMol3 package in Materials Studio, *Accelrys*, using a GGA PBE functional).

and the Ag $3d$ peaks valence structure had their respective characteristic line shapes.

Bi-isonicotinic acid (4,4'-dicarboxy-2,2'-bipyridine from *Alfa Aesar*), shown in Figure 5.1, was deposited onto the surface in-situ by sublimation from a Knudsen-type cell evaporation source. Low coverage and high coverage films (controlled by exposure time) were measured using x-ray photoelectron spectroscopy (XPS), x-ray absorption spectroscopy (XAS) spectroscopy, and resonant photoelectron spectroscopy (RPES). XPS, measured with an undulator gap of 17 mm, was calibrated to the binding energy scale by aligning the silver Fermi edge to 0 eV, giving an uncertainty in the binding energy scale on the order of 0.05 eV. The data presented has been processed by the subtraction of a Shirley background and peak fitting has been performed using a pseudo-Voigt function where a combination of Gaussian and Lorentzian lineshapes were fitted to the data. The Lorentzian width was fixed at 0.3 eV and the Gaussian contribution allowed to vary in the fitting procedure.

XAS and RPES were measured over the N $1s$ absorption edge with a taper applied to the undulator to minimise variations in photon flux at different energies. The photon energy scales were checked using the kinetic energy difference between Ag $3d$ XPS peaks collected using first and second order light. The spectrometer was run in fixed constant final state and constant initial state modes for XAS and RPES measurements respectively and swept mode for XPS. Given the long scan durations (up to two hours), the sample was continually moved during measurements at a rate determined to be safe by beam-damage studies. N $1s$ XAS data was placed on a binding energy scale by subtracting the binding energy position of the N $1s$ core-level (measured using XPS) from the calibrated photon energy values. This method is discussed in detail elsewhere [123].

This paper refers to *monolayer* and *multilayer* coverages - these two datasets correspond to two separate depositions. For the multilayer films, the Ag $3d$ substrate peaks were almost undetectable in the XPS measurements. For the monolayer film, molecules were deposited until the peak ratios in the XPS and the lineshape of the valence band region were consistent with monolayer and sub-monolayer data for these molecules on other surfaces [11, 137]. This method was chosen over that of annealing a multilayer [11, 137] in order to avoid potential damage to the molecules through excessive heating as previously observed in the N $1s$ XAS for bi-isonicotinic acid on the Au(111) surface [11] using this approach.

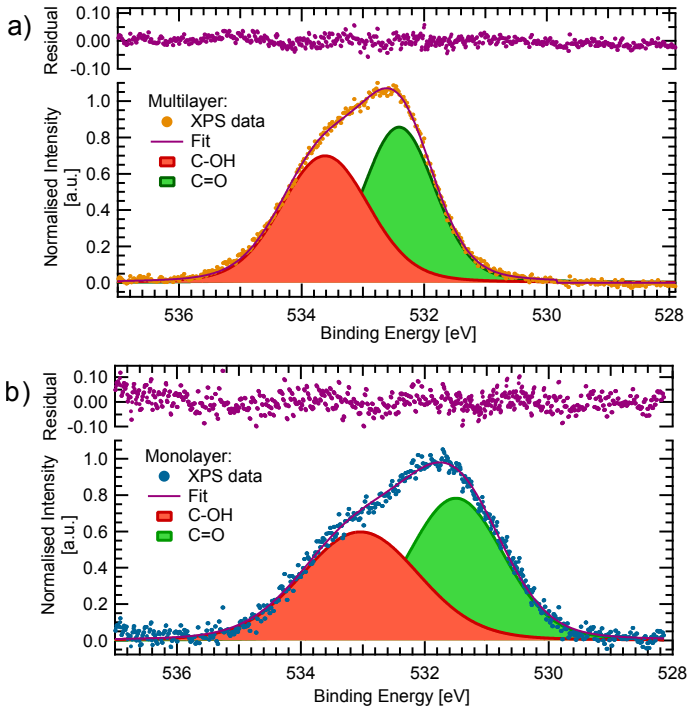


Figure 5.2: O 1*s* XPS spectra for a) multilayer and b) monolayer films of bi-isonicotinic acid on Ag(111). The data has had a Shirley background subtracted. The curve fitting reveals two peaks which we attribute to the carbonyl and hydroxyl oxygen atoms (residual shown above each spectrum). The area under both peaks is equal. The thick film data was collected at normal incidence with a photon energy of 722 eV. The thin film data was collected at a grazing angle of 55° at 600 eV to enhance surface sensitivity.

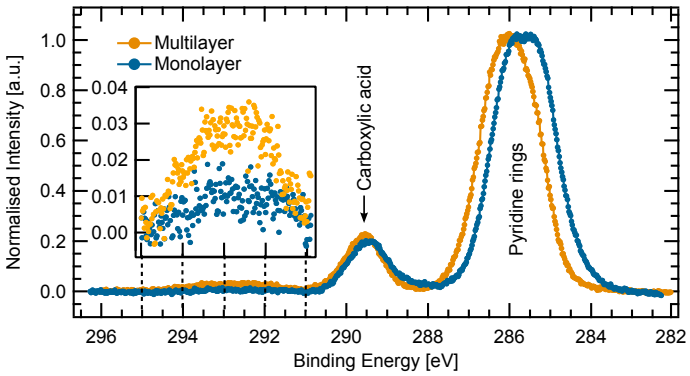


Figure 5.3: C 1*s* XPS spectra for monolayer and multilayer coverage of bi-isonicotinic acid on Ag(111). The peak at 289.5 eV is attributed to the carboxylic acid group and the peak at ∼286 eV to the pyridine ring. A Shirley background was subtracted from both spectra. An excitation energy of 514 eV and 340 eV was used for the multialyer and monolayer, respectively.

5.3 Results and discussion

The photoemission spectra provide an indication of how the bi-isonicotinic acid molecules interact with the surface by comparing the monolayer film, where molecules can interact with the surface, and multilayer where the molecules able to interact with the surface are deeply buried so are not measurable using photoemission). The most dramatic difference between the two is seen in the O 1*s* spectra, shown in Figure 5.2. The multilayer data is shown in Figure 5.2a exhibiting two overlapping peaks at 533.6 eV and 532.4 eV. These are attributed to the oxygen atoms in the hydroxyl (C-OH) and carbonyl (C=O) groups in the carboxylic acid group of the molecule, respectively.[137] For the monolayer coverage there are also two peaks, here at 533.0 eV and 531.5 eV, attributed as for the multilayer. The two peaks each have a normalised area of 0.5, consistent with the stoichiometry of the molecule (a 1:1 ratio of oxygen atoms in the two chemical environments).

There are a few notable features of the O 1*s* spectra. First, the position of the peaks has changed between the monolayer and multilayer coverages - there is a general shift towards lower binding energy for the monolayer. Such shifts are commonly attributed to screening of the core-hole by electrons in the metal surface [101] but one would expect this shift to be uniform across the entire spectrum. Here, the carbonyl peak has shifted relative to the hydroxyl peak by 0.35 eV indicative of a stronger interaction between of carbonyl group with the surface compared to the hydroxyl group. Secondly, the peaks are broader in the monolayer

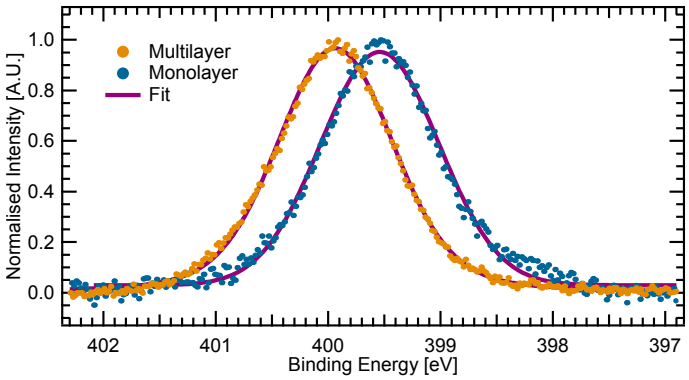


Figure 5.4: N 1*s* XPS spectra for multilayer and monolayer coverages of bi-isonicotinic acid on Ag(111), fitted using identical parameters. Both spectra were measured at normal emission with an excitation energy of ∼500 eV and have had a Shirley background subtracted.

data, most likely due to a number of different possible bonding/interaction sites on the surface.

C 1*s* XPS data is shown in Figure 5.3 for the multilayer and monolayer. There are two clear peaks visible at approximately 286 eV and 289.5 eV and a small peak at ∼293 eV. The latter is shown magnified in the inset. As with previous studies [137], the lower binding energy peak (∼268 eV) has been assigned to the carbon atoms in the pyridine ring and the higher binding energy peak (∼289.5 eV) to the carboxylic group. The low intensity satellite at ∼293 eV is attributed to a shakeup feature [138]. For the pyridine carbon, there is a clear shift of ∼0.35 eV to lower binding energy. As discussed above in the context of the O 1*s* spectra, such a shift can be explained by screening effects. As before, one would expect an equal shift of the entire region – screening alone therefore fails to explain why the shift is only apparent for the pyridine ring and not the carboxyl carbon atoms. Given the O 1*s* data where the carbonyl oxygen is potentially interacting with the surface, we propose that there may be a slight positive charge formed at the carboxyl carbon atom due to the surface interaction drawing electron density away from it. This increases the binding energy of the carboxylic C 1*s* featuring countering the negative binding energy shift caused by screening from the surface.

Taking the oxygen and carbon spectra into consideration, the possibility that the silver is causing deprotonation of the carbonyl group can be ruled out. If deprotonation occurs, there are two possible scenarios. Firstly, for the case of partial deprotonation of the monolayer molecules, one would expect a third, lower binding energy peak in the O 1*s* and a further peak in the C 1*s* region close to the carboxylic group binding energy. Cebula *et al.* [139] have recently studied similar small organic molecules featuring carboxylic acid groups and have seen

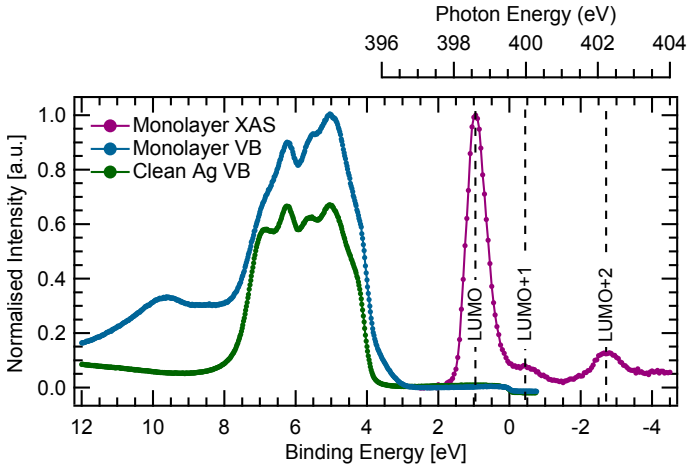


Figure 5.5: Density of states plot of a monolayer of bi-isonicotinic acid on Ag(111) measured at normal emission. The purple line shows an x-ray absorption spectra (measured over the N 1*s* absorption edge) showing unoccupied states placed on a binding energy scale. The blue and green lines shows the valence spectrum of the monolayer and clean surface respectively, measured by photoemission spectroscopy with a photon enegry of 50 eV. All spectra were collected at normal emission.

this behaviour when using electrochemical underpotential deposition. While their XPS findings may not translate directly to the present study (where the deposition technique does not create ionised species by design), the comparison is still of value. For the second scenario, where all the carboxylic groups are deprotonated, one would only see two peaks in the O 1*s*, corresponding to C=O and C-O$^-$, although in practice the binding energies of these two environments are indistinguishable in the O 1*s* and instead are typically observed as a single peak at the C=O binding energy. The C 1*s* would also show two peaks but with the carboxylic group shifted to lower binding energy.

Here, there is no evidence of deprotonation in the C 1*s* spectra. Li *et al.* [140] have also studied isonicotinic acid (half of the bi-isonicotinic acid molecule), deposited via sublimation from a K-cell, on Ag(111) and also measured O 1*s* XPS data consistent with no deprotonation of the monolayer. We can also rule out the possibility that the data may contain a multilayer contribution – attempting to include a second set of peaks into the curve fitting in a way that would be consistent does not lead to a realistic curve-fit. The difference between the monolayer and multilayer data therefore likely represents real shifts in binding energy between the bulk molecule and the adsorbed molecules due to the combined effect of screening and the interaction of the carbonyl moiety with the Ag(111) surface.

The corresponding N 1*s* XPS spectra are shown in Figure 5.4 exhibiting a single peak that is the same shape for the monolayer and multilayer films, which is consistent with the single bonding environment exhibited by nitrogen atoms. There was a small shift, again consistent with screening effects, between the thin and thick film measurements of 0.38 eV (compared to screening shifts of 0.35 eV seen in both the O1 *s* and C1 *s* spectra).

Previous studies have considered the effects of hydrogen bonding between bi-isonicotinic acid molecules (and related pyridine carboxylic acid molecules) and have seen little evidence indicative of hydrogen bonding between bi-isonicotinic acid molecules [141]. This is consistent with what is seen here - there are no shifts or multiple peaks in N 1*s* or O 1*s* that would indicate the presence of N$\cdots$O-H hydrogen bonding. The weak feature at $\sim$398.5 in the monolayer N 1*s* is on the wrong side of the peak to be attributed to hydrogen bonding. The origin of this weak feature is still undetermined.

An experimental density of states for the monolayer is presented in Figure 5.5. This includes the N 1*s*, and the valence band photoemission data measured at 50 eV photon energy. The valence band of the clean silver surface is also included. These measurements were all taken with the surface normal to the analyser. The peaks in the XAS at $BE \approx -0.5$ eV and $BE \approx -2.5$ eV, as marked on the figure, are assigned to the LUMO+1 and LUMO+2 states of the core-excited molecules.

It is clear from Figure 5.5 that the LUMO, the largest peak in the XAS data ($BE = 1$ eV) , lies entirely below the Fermi edge. This, in principle, allows electrons to charge transfer from the silver surface into the LUMO of the core-excited molecule. It is worth noting that this partially filled state is likely to cause slight shifts in the band positioning, and critically, these electrons are able to participate in the relaxation of the molecule back to the ground state after the core-excitation, a process that can be explored in detail using resonant photoemission spectroscopy (RPES).

The resonant photoemission data is shown in Figures 5.6 and 5.7. The 2D plots show the intensity of emitted valence photoelectrons as a function of both incident photon energy and their measured binding energy. Sweeping through a range of photon energies finds points where the incident light is on resonance with an excitation process (the photon energy matches the energy difference between a core level and a molecular orbital) which is measured by an increased flux of emitted photoelectrons. Measuring the binding energy of these emitted electrons allows us to infer the decay channel by which the system relaxed back to its final state.

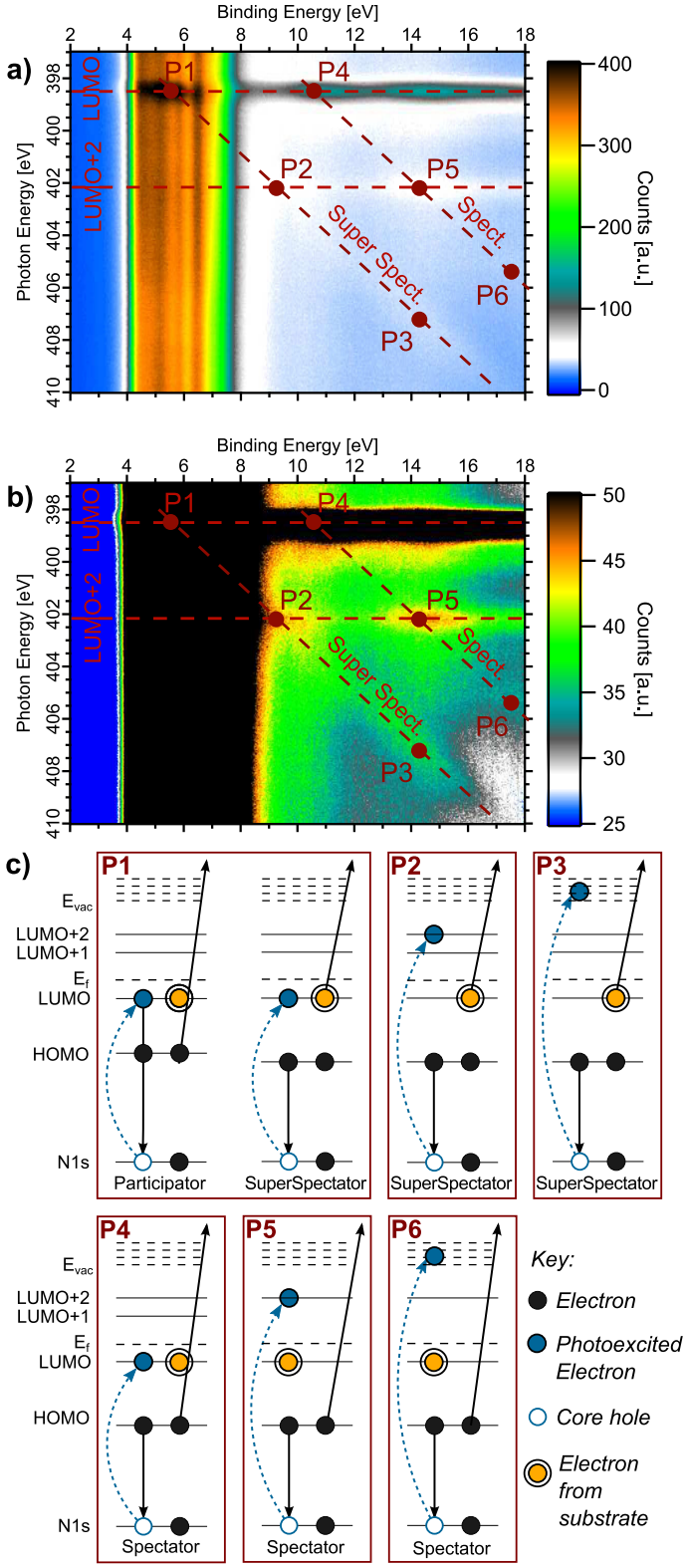


Figure 5.6: Resonant photoemission map of a monolayer of bi-isonicotinic acid on Ag(111) collected at normal emisssion plotted using two colour map scales. The LUMO energy levels are indicated with horizontal dashed lines and the diagonal lines highlight constant kinetic energy features. Figure a) is scaled across the whole range of data and b) to emphasise the spectator and super-spectator features. Figure c) shows schematics of proposed decay mechanisms marked as points P1-P6 (on the RPES data) after excitation of an N 1*s* core electron (shown with a dotted arrow).

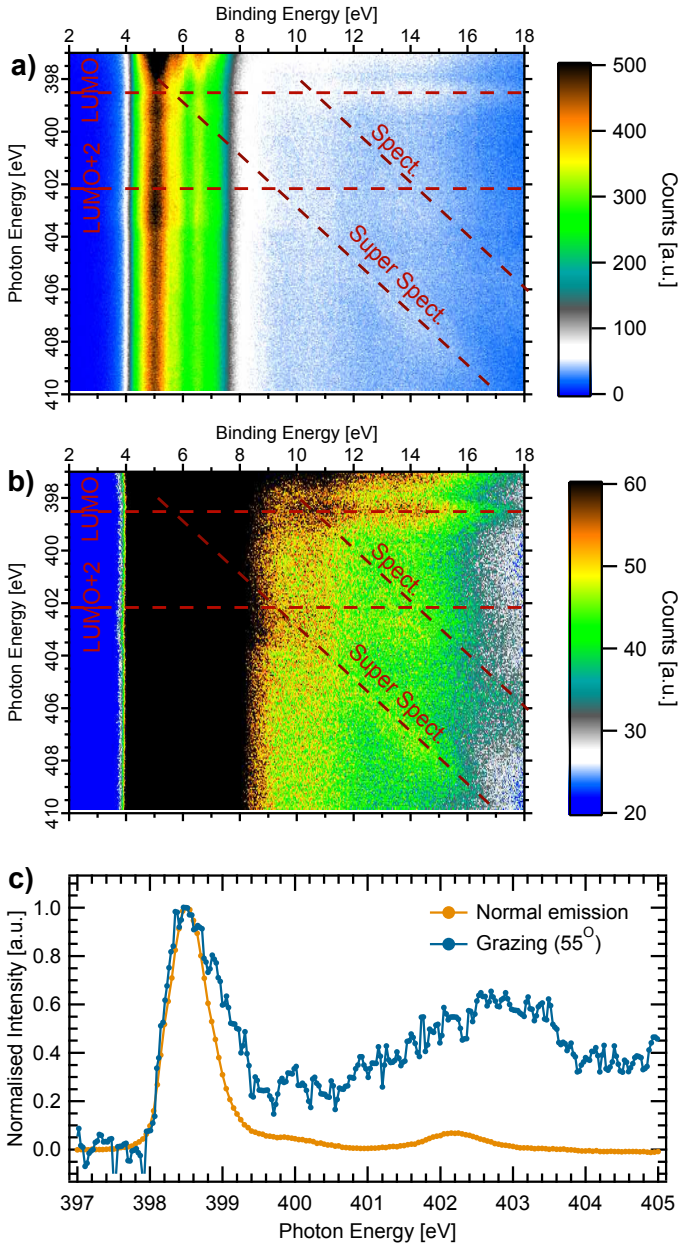


Figure 5.7: Resonant photoemission scan of a monolayer of bi-isonicotinic acid on Ag(111) collected at a grazing angle of 55° from normal emission using two colour map scales. The LUMO energy levels are indicated with horizontal dashed lines and the diagonal lines highlight constant kinetic energy features. Figure a) is scaled across the whole range of data and b) to emphasise the spectator and super-spectator features. Figure c) compares XAS extracted from both this grazing incidence RPES and the normal emission RPES (Figure 5.6).

Figure 5.6 was collected with the surface orientated normal to the analyser (normal emission)and Figure 5.7 with the surface normal to the incident light (55° emission angle). The *horizontal* dashed lines mark the regions of intensity that appear at constant excitation energy - which are attributed to excitation into LUMO states. The LUMO+1 level is not marked as the intensity of features attributed to the LUMO+1 are too weak (see N 1s XAS in Figure 5.5) to be distinguished from the high-photon energy tail of the LUMO. The *diagonal* lines highlight constant kinetic energy features that are have attributed to *spectator* and *super-spectator*/*super-Auger* decay channels. All of these dashed lines are shown in the same places on all the plots. Six key points of interest on these lines (P1-P6) are marked each with associated schematic diagrams at the bottom of the panel (Figure 5.6c). These describe possible decay mechanisms that give rise to the different spectral features, shown with solid arrows, after the initial excitation (shown with dashed arrows) and creation of the core-hole.

The enhancement at P1 – located at the intersection of the HOMO binding energy and the LUMO absorption energy – is due to *participator* electrons. This is a decay mechanism where the originally photoexcited electron recombines with the core-hole and another electron from the HOMO is emitted. For *spectator* decay (P4, P5 and P6) on the other hand, a core electron is excited into an unoccupied molecular orbital and does not further participate in the relaxation of the system into its final state (within the lifetime of the core-hole). Electrons from occupied molecular orbitals undergo an Auger-like decay process where one electron recombines with the core-hole and another is emitted into the vacuum. The kinetic energy of these electrons is constant and must be lower than participator electrons by at least the HOMO-LUMO gap. The intensity around points P4 and P5 on the spectator decay line result from when the incident energy is on resonance with transitions between the N 1s core level and the LUMO and LUMO+2 states respectively. P6 shows the excitation of the core electron into the continuum of states above the vacuum level (including sigma anti-bonding orbitals, σ^*). This again decays via the spectator channel as shown in Figure 5.6c.

As the LUMO lies below the Fermi level, electrons from the silver surface can partially fill this orbital opening up the potential super-spectator and super-Auger decay channel. Super-spectator decay is again an Auger-like like process where the electrons in the LUMO (originally from the surface) along with an electron from an occupied state, are involved in photoemission and recombination with the core-hole. P1, P2 and P3 show this mechanism after excitation of an N 1s core electron into the LUMO, LUMO+2 and above the vacuum level, respectively. The electrons emitted via this process have constant kinetic energy and with a

separation from spectator decay equal to the HOMO-LUMO gap. Therefore at point P1, this process is indistinguishable from participator decay - the final state of both processes is the same and the emitted photoelectron will have the same energy.

A further possibility is a *super-Auger* decay process in which a photoexcited electron in an unoccupied state can charge transfer into the metal as well as an electron simultaneously transferring from the metal to the LUMO. The electron originally from the surface is emitted (as in *super-spectator* decay). The *super-Auger* mechanism is therefore an example of bi-directional charge transfer [142] that can occur when the photoexcited electron is not localised to the unoccupied state within the core-hole lifetime. This mechanism is discussed in detail by Gibson et al. in the context of C_{60} on single crystal metal surfaces [34]. The conceptual picture of this core-hole decay mechanism can be visualised in Figure 5.6c by considering the originally excited electron (shown in blue) as having tunnelled away and plays no further role. This scheme is valid for panels P2 to P6 as these involve states that lie above the Fermi level and therefore overlap with empty states in the conduction band. For panel P1 however this is not the case and the illustrated picture with the originally excited electron localised in the LUMO represents the only available option.

The super-Auger model is consistent with two important observations in the RPES data. Firstly, the diagonal feature associated with this charge-transfer Auger process has a constant kinetic energy. This might imply the absence of a spectator shift arising from the localised electron in the unoccupied valence state, since such an effect should be weaker when the core-electron is excited to a state above the vacuum level, which is just above the LUMO+2 absorption. For a true super-spectator process one might therefore expect a shift to lower kinetic energy when exciting into a localised state compared with excitation into a quasi-bound state. Secondly, as observed in Figure 5.6a, the participator feature is not symmetric around the point where the so-called super-spectator line intersects the LUMO absorption energy at point P1, but rather extends to higher kinetic energy (lower binding energy). Since ultra-fast bi-directional charge transfer is not possible for the LUMO (since it lies entirely below the Fermi level of the metal surface), only the participator and super-spectator processes illustrated in panel P1 of Figure 5.6c are valid. Both of these processes contain both the electron transferred from the surface and the originally excited electron in the LUMO and should therefore be shifted to slightly higher kinetic energy (the so-called spectator shift) than that of the super-Auger intersection at point P1. A super-Auger process is therefore the most likely origin of the high kinetic energy Auger-like feature

observed for states above the Fermi level, while a super-spectator process takes place for the LUMO, which lies entirely below the Fermi level.

Figure 5.7 shows the same experiment carried out at normal incidence, with the electric field vector of the light in the plane of the surface. Here, at the LUMO resonance photon energy there is very little intensity attributed to Auger and Auger-like features - this implies the molecules are laid flat on the surface as in this geometry the π^* orbitals of the planar molecule have a low interaction cross-section with the electric field vector of the incident light. The σ^* orbitals on the other hand lie in the same plane as the surface leading to spectator and super-spectator features being measurable in both orientations. This is further demonstrated in Figure 5.7c) which compares the XAS extracted from the Auger region of both normal and grazing emission datasets. The two plots are normalised to the intensity of the LUMO peak.

The behaviour of bi-isonicotinic acid on Ag(111) as studied here is consistent with the work of Taylor *et al.* who have previously studied the same molecule on the similar Au(111) surface [11]. They showed using angle resolved x-ray absorption measurements that the molecule is almost parallel to the surface (with the ring having an average angle greater than 70° to the surface normal). On Au(111) as Taylor *et al.* demonstrated with their N 1*s* XAS-derived experimental density of states, the LUMO only partially overlaps with the Fermi level of the gold substrate. On Ag(111) however, the entire state lies below the Fermi level providing a clear cut-off between the possibilities for super-spectator and super-Auger decay below and above the Fermi level, respectively.

5.4 Conclusions

This study has presented high resolution XPS and XAS data for bi-isonicotinic acid deposited *in-situ* on a Ag(111) single crystal surface. The XPS suggests an interaction between the carboxyl group and the silver surface. The N 1*s* XAS shows that the LUMO lies below the Fermi level therefore allowing the state to be partially occupied with electrons from the metal. Resonant photoemission measurements allowed us to probe this charge transfer via measurement of the super-spectator and super-Auger decay mechanisms whereby an electron originally from the metal is involved in the decay of the core excited state of the molecule. Due to the energetic alignment of the unoccupied molecular orbitals with respect to the density of states of the underlying surface, super-Auger decay arising from ultra-fast bi-directional charge transfer dominates for states above the Fermi level, while super-spectator decay dominates for the LUMO state that lies below.

5.5 Acknowledgements

We would like to thank the authors of the Taylor et al. study [11] for allowing us access to the RPES data presented in their 2007 paper.

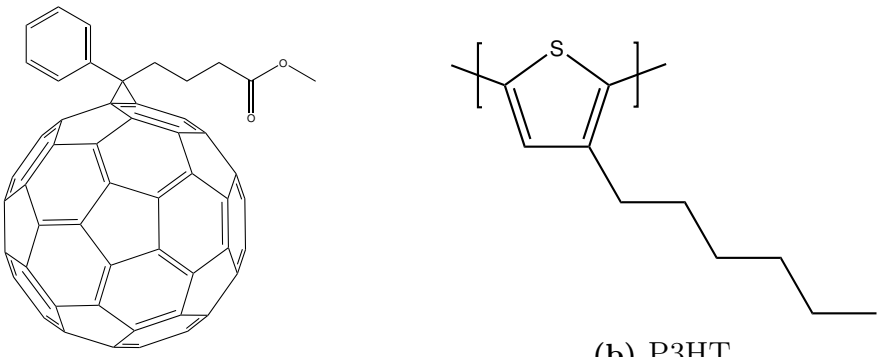
Chapter 6

A photoemission study of PCBM/P3HT films, bi-layers and bulk heterojunctions prepared by electrospray deposition

6.1 Introduction

Organic photovoltaics (OPVs) provide a potential low cost light harvesting solution (see Chapter 1.3) where two of the key molecules used are the fullerene derivative Phenyl-C61-butyric acid methyl ester (PCBM) and the polymer poly(3-hexylthiophene-2,5-diyl) (P3HT). Photoelectron spectroscopies combined with electrospray deposition has become a well tested combination for studying complex molecules for molecular photovoltaics - specifically in the context of dye sensitised solar cells [4, 5, 36]. This chapter aims to apply photoelectron and X-ray absorption spectroscopies to characterise not only these two molecules, but also of model heterojunctions/bi-layers and bulk heterojunctions comparable to those used in organic photovoltaic devices, all deposited in-situ by electrospray deposition.

There is of course existing literature investigating these systems but photoemission data is spread widely across many studies. Existing work does cover XPS (X-ray photoelectron spectroscopy) and NEXAFS (near edge X-ray absorption fine structure) of both PCBM [102, 143, 144] and P3HT [145–148]. Many of these studies aim to address specific issues, such as the stability of the molecules. There has been some work investigating the effects when the two molecules are brought together in both bi-layers [149] and bulk heterojunctions [150]. Although



(a) PCBM **(b)** P3HT

Figure 6.1: Structure Phenyl-C61-butyric acid methyl ester (PCBM) and Poly(3-hexylthiophene-2,5-diyl) (P3HT).

there has been some interest in using ambient electrospray deposition to fabricate organic photovoltaics devices [130, 151–155], there are no existing studies that have constructed model OPV heterojunction devices in UHV using electrospray. P3HT has however been deposited using vacuum electrospray onto the indium tin oxide surface [156]. One of the aims of this chapter is to provide a comprehensive XPS and NEXAFS study of the molecular system - PCBM and P3HT both individually and in heterojunctions - deposited in situ in UHV by electrospray.

There has been one previous attempt to use resonant photoemission to study PCBM [103] but this has not been attempted for P3HT. The second objective of this chapter is therefore to use resonant photoemission to attempt to probe charge transfer between the individual molecules and their surface, as well as charge transfer between the two molecules when in a heterojunction (which no-one has attempted previously). The final aim is to investigate the energy shifts of the core levels, by careful measurement of their ionisation potential (see Chapter 2.4.1), when the the molecules are brought together into a heterojunction. This may allow us to infer the positions of the valence band maximum of each of the two molecules in the heterojunction to investigate any band bending that may occur.

We have selected the Au(111) surface as gold is used as an electrode in the devices, it is not an oxide allowing us to easily study the oxygen environment of PCBM monolayers and we have experience measuring the related C_{60} molecule on this surface [34].

6.2 Methods

A range of instruments were used to measure these molecular systems using X-ray photoemission spectroscopies including two beamlines at MAX IV Laboratory. Two separate weeks of beamtime at D1011 were used for XPS and XAS (X-ray absorption spectroscopy) measurements. The first of which was used for was preliminary measurements, the second of which was dedicated to collecting good statistics and ionisation potential calibrations. Resonant photoemission, as well as supporting XPS and XAS, was measured at beamline I311 to try and probe charge transfer dynamics where C_{60} was also deposited, via electrospray, for comparison. For comparison a series of ex-situ samples were also produced, using spin casting and electrospray, and measured using Kratos Axis Ultra instruments.

XPS binding energy scales were calibrated by placing the Au $4f_{7/2}$ peak at 83.95 eV [157] or by placing the gold Fermi edge at 0 eV where possible. The position of the Au $4f_{7/2}$ peak was confirmed by our own measurements. For the case of very thick spin cast films, the C $1s$ peak was used for calibration. Curve fitting was done using a pseudo-voigt function with a fixed Lorentzian width of 0.2 eV. The Gaussian contribution was allowed to vary as a parameter in the fit.

It is worth highlighting that this work refers to monolayer and multilayer coverages of molecules. An intrinsic feature of the electrospray system is that it does not produce perfectly uniform films, allowing multiple coverages to be explored (assuming you have a small X-ray spot size/analysis area) on a single sample. "Multilayer" coverages were defined by the burying of the substrate peaks in the XPS to ensure measurements represented isolated molecules not under the influence of the surface. "Monolayer" coverages, have been classified as monolayer-like by the presence of molecule features with surface features still being dominant in the XPS. It is unlikely that any of the "monolayers" presented here are perfect monolayers, but instead were most likely sub-monolayers or in some cases slightly more than one monolayer. But regardless of how complete the "monolayer" films were, the measured signal from the molecule was dominated by molecules interacting with the surface.

6.2.1 Synchrotron experiments

On I311, the carbon dip was severe and subtraction of a background was required for all XAS and RPES (resonant photoelectron spectroscopy) measurements. The background used, which was collected by measuring a C K edge absorption spectra on a clean gold crystal, is shown in Figure 6.2 with an example RPES map before

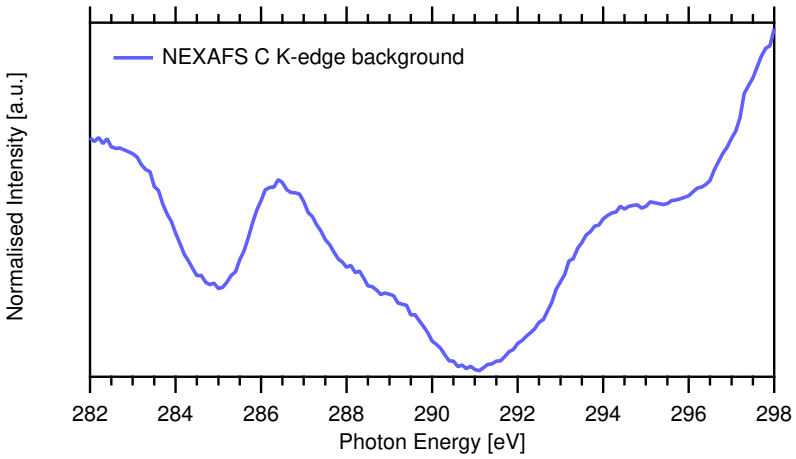
and after dividing through each vertical strip of data through by this background. In pretty much every case, it was not possible to fully compensate for the dip, even with artificially produced backgrounds, as further compensation over compensates in the low binding energy region adding intensity where there should not be any. Therefore the carbon dip is still visible in the Auger region of the maps. The NEXAFS spectra presented were generally collected at D1011 where the carbon dip was minimal - here the background adjusted for the shape rather than trying to add in huge amounts of intensity that is not there.

Photon energies were calibrated by measurement of a core level (typically either C $1s$ or Au $4f$) using first and second order light. The binding energy axis of RPES maps was calibrated against valence band XPS data (which in turn was calibrated to the gold Fermi edge) or from the position of the second order XPS peak.

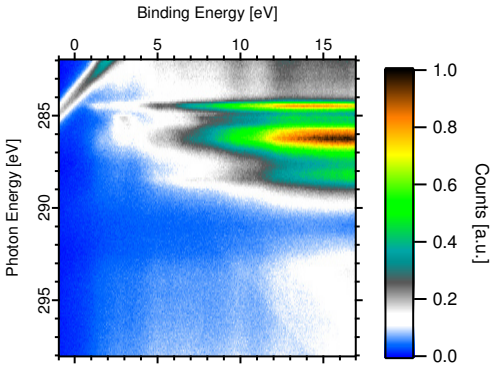
On D1011 the beamline and spectrometer were carefully optimised to obtain the best possible resolution at the count rates required to get good statistics. For XAS, the partial yield detector was used with a retardation potential of 200 eV applied to the grid. For core level and valence band XPS there was little resolution benefit in using pass energies below 100 eV and 50 eV, respectively, with a 0.8 mm curved slit. At I311 XPS was typically measured with a pass energy of 50 eV (or below) as the beamline is both higher resolution and much more brilliant due to the insertion device. For RPES and XAS, the hemispherical analyser was used in constant initial state and constant final state modes respectively with a pass energy of 200 eV. Both beamlines have an angle between the incident X-ray beam and the spectrometer of 55°. All measurements taken using I311 were taken at normal incidence. At D1011, normal emission was used.

As well as binding energy calibration to the gold Fermi edge, the D1011 data was also calibrated to the vacuum level by measurement of the secondary electron cut-off. To do this a bias of -6 V was applied to the sample using a Keithley voltage source to shift the XPS spectrum (and secondary electron cut-off) to a kinetic energy where they were distinct from the analyser cut-off. This process is explained in Chapter 2.4.1.

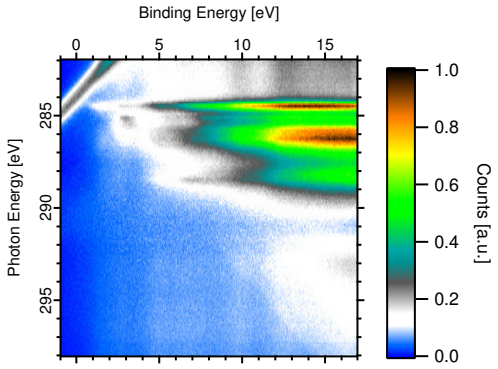
PCBM and C_{60} were dissolved to a concentration of $\sim$0.05 % (w.t.) - the molecules had dissolved completely after around 30 minutes. 10% methanol was then added to allow it to be sprayed. P3HT was also dissolved in toluene but, due to its poor solubility, the preparation was slightly more involved. 4 mg was placed in toluene and left for 10 hours. At this stage, the solution appeared saturated (the colour had not changed for several hours) but there was still precipitate left in the vial which was left to separate out. The solution was decanted, and



(a) I311 carbon dip



(b) Original RPES map before background subtraction



(c) RPES map after background subtraction

Figure 6.2: X-ray absorption background subtraction at beamline I311. Figure **a** shows the carbon dip - a NEXAFS measurement over the carbon K edge on a clean Au(111) substrate where no carbon was visible in XPS measurements. Figures **b** and **c** show an example RPES map, of PCBM, before and after the subtraction of the background shown in **a** respectively.

again 10% methanol was added to allow electrospray deposition. This preparation method meant it was not possible, using the facilities available, to determine the concentration of the solution.

There was always some precipitate left regardless of how much P3HT molecule was initially added to the toluene leading us to suspect the toluene was only dissolving shorter polymer chains. The same behaviour was observed under gentle heating. When sonicated, the colour changed dramatically from a yellow to a deep red, but the same yellow solution was obtained by passing the "solution" through a filter (so sonication was just creating a suspension). These methods were not used to produce the solutions used in the experiments - filtering the "real" solutions was not possible as the filters available were made of a material that was not compatible with toluene.

PCBM and C_{60} could be cleaned off the Au(111) crystal by a few rounds of sputter and anneal cycles. Argon ion sputtering was generally run for 10 minutes at 2 kV followed by 10 minutes at 1 kV. Electron beam bombardment on the back of the sample plate was used to heat the sample to 600 °C for each 20 minute anneal cycles. P3HT had to be cleaned off, ex-situ, via ultrasonication in toluene. It appeared the polymer chains were too large to be sputtered at these energies with single argon ions and annealing caused the polymer to damage and blend into the crystal.

6.2.2 Lab-source experiments

For comparison, a series of ex-situ samples were also produced, on gold substrates, and measured using the Kratos Axis Ultra XPS system. A Silicon wafer was cleaved into $\sim$1 cm^2 substrates then cleaned by ultrasonication in acetone, methanol and IPA before the thermal evaporation of 10 nm of titanium followed by 100 nm gold (the titanium aided adhesion of the gold). The first set of samples were made by drop casting the same solutions made for the second D1011 experiment onto gold substrates with the aim of comparing to the in-situ electrosprayed measurements. These measurements were made several months later but the solutions seemed stable and were stored in the dark in case they were photosensitive.

A second set of ex-situ samples were made by both electrospray deposition and spin casting from chlorobenzene solutions. For this experiment stock solutions of 1 % (w.t.) of P3HT and PCBM were made. Both molecules were easily soluble in chlorobenzene, to notably higher concentrations than this, by gently heading to $\sim$80 °°C on a hot plate. Mixtures of the two molecules were made with ratios 1:0.8, 1:1 and 2:1 of P3HT:PCBM. These were spin cast onto the gold substrates

at 2000 rpm. Electrosprayed samples were made by diluting these solutions to 0.01 % (w.t.) and adding 20 % acetone to make them compatible with electrospray ionisation. Methanol caused the P3HT to drop out of solution fairly rapidly while using acetone made the solutions stable for the duration of the experiments. The spin cast samples were very thick, so the charge neutraliser was required for these XPS measurements.

6.3 PCBM and C_{60}

6.3.1 XPS

In the PCBM/P3HT system, understanding of the O 1*s* is important as it is the unique species for PCBM. A sample of O 1*s* spectra from all the deposits measured (over all the experiments) are shown in Figure 6.3. In order to make comparison of the shape easier, the spectra have been aligned on top of each other (there are small energy shifts in the raw data due to film thickness variations) and normalised to the lower binding energy peak, centred at 532.7 eV which is attributed to the carbonyl (C=O) oxygen environment. The higher binding energy shoulder, at ∼534 eV, is attributed to the methoxy (-C-O-CH_3) environment. There is some minor variation in the relative size of the methoxy peak, most likely as a result of beam damage to the molecule. The spectra have had a Shirley background subtracted, and although some of the intensity variation may be as a result of a background shape that the Shirley method does not account for, one would expect this effect to be much less significant than is apparent here. Other types of background subtraction (linear, Tougaard etc) did not change the presented results significantly.

Curve fitting for the I311 multilayer sample is shown in Figure 6.4 where the fit produces two peaks with areas with a 1:1 ratio which is consistent with the stoichiometry of the molecule. For the samples with a lower methoxy peak, it was not possible to fit a 1:1 area ratio (by letting the Gaussian width vary) so it is therefore unlikely it is a broadening of the peak but a genuine loss of that species.

Understanding the carbon spectra can be aided by comparison to the related C_{60} molecule which was also deposited onto the gold surface via electrospray. C 1*s* spectra for multilayer films of both molecules are presented in Figure 6.5. C_{60} has a single peak followed by a complex shake-up structure. PCBM contains some broadening of the main peak on the higher binding energy side which has been attributed to carbon-carbon environments in the ligand. The curve fitting of this spectra, which has had a Shirley background subtracted, also supports this

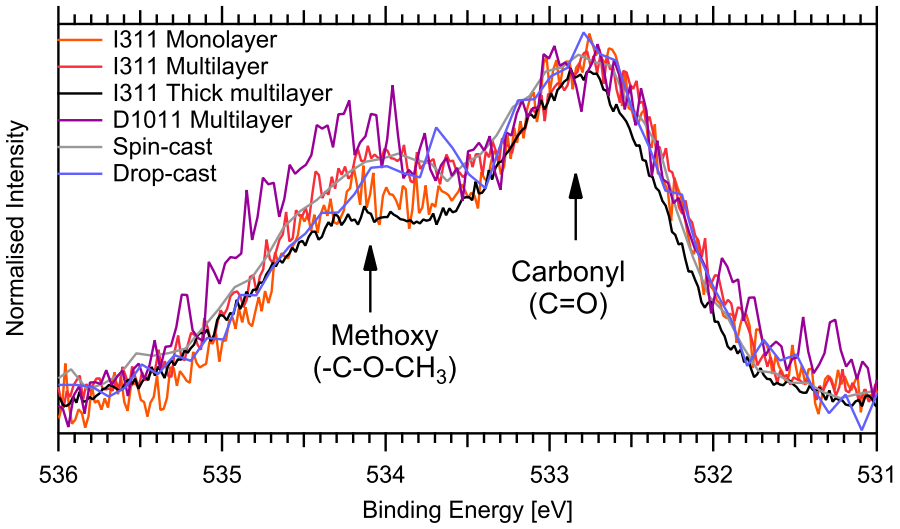


Figure 6.3: Normalised and aligned O 1*s* spectra measured from a range of different PCBM on Au(111) samples. The I311 and D1011 measurements were taken at $h\nu$ =650 eV whilst the spin and drop cast samples using $h\nu$ = 1486 eV light.

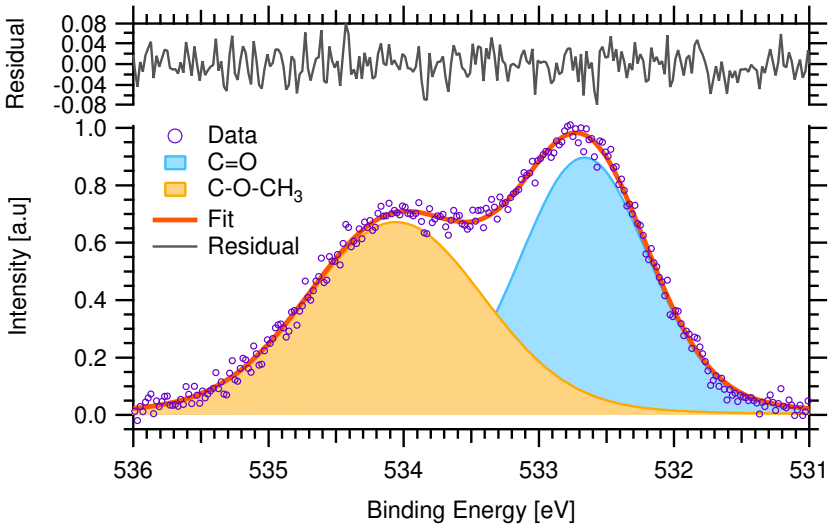


Figure 6.4: PCBM multilayer measured on I311 with $h\nu$ = 650 eV. Proposed peak fitting of the spectra, which has a Shirley background subtracted, show a two peaks at ∼354 eV and ∼352.7 eV of equal areas.

which is also included in Figure 6.5. Fitting two peaks with only the Lorentzian contribution fixed produced peaks with normalised areas of 0.85 and 0.15, centred at 285 eV and 285.8 eV, which has been assigned to the cage and ligand carbon atoms respectively. This is consistent with the stoichiometry of the molecule.

We would expect to find the two carbon-oxygen environments within the shake-up structure. Monolayer C 1*s* data is presented in Figure 6.6 alongside the same multilayer spectrum shown in Figure 6.5 (both collected at I311). As the background is so complex, a linear and Shirley background were subtracted sequentially (despite it being unconventional it is the only approach found that produced a relatively flat background). Both spectra are normalised to the main peak. The shoulder at ∼287.2 eV and the peak at ∼289.4 eV do not change intensity with coverage. The peak at ∼291.5 eV however does get larger for the monolayer. One would expect the shakeup structure to be reduced for the monolayer coverage as the symmetry is broken by interactions with the surface, which is the opposite of what we see here. Our peak assignments are all however consistent with those in the literature [103].

The valence band of PCBM and C_{60} for both monolayer and multilayer coverages are presented in Figure 6.7. For both coverages, the molecules show very similar features indicating the valence structure of PCBM is dominated by the C_{60} cage. The HOMO (highest occupied molecular orbital) and HOMO-1 peaks are found at ∼2.5 eV and ∼4.0 eV respectively. Indicated with a black arrow is a subtle increase in PCBM's intensity that can not be attributed to the C_{60} and is localised on the ligand. The PCBM orbitals are very broad compared to the series of very well defined HOMO peaks of the C_{60} molecule. This is known to be due to addition of the ligand; the electronic states of which can interact with the C_{60} cage in a number of ways including breaking degeneracy, mixing of electronic states and hybridisation of the orbitals between the cage and ligand [158].

It is finally worth noting the precise binding energy values of the orbitals is meaningless for the multilayer spectra as they were calibrated by measurement of the Au Fermi edge on a clean area of the crystal. The calibration therefore does not account for shifts due to film thickness. It is also a possibility, as this sort of charging effect can also affect the line-width of photoemission peaks, that the film thickness could be contributing to the broadening out of the spectral features. This is however improbable as we see minimal broadening effects when comparing the widths of the multilayer and monolayer core levels leading us to believe the broadening is dominated by the ligand-cage interaction.

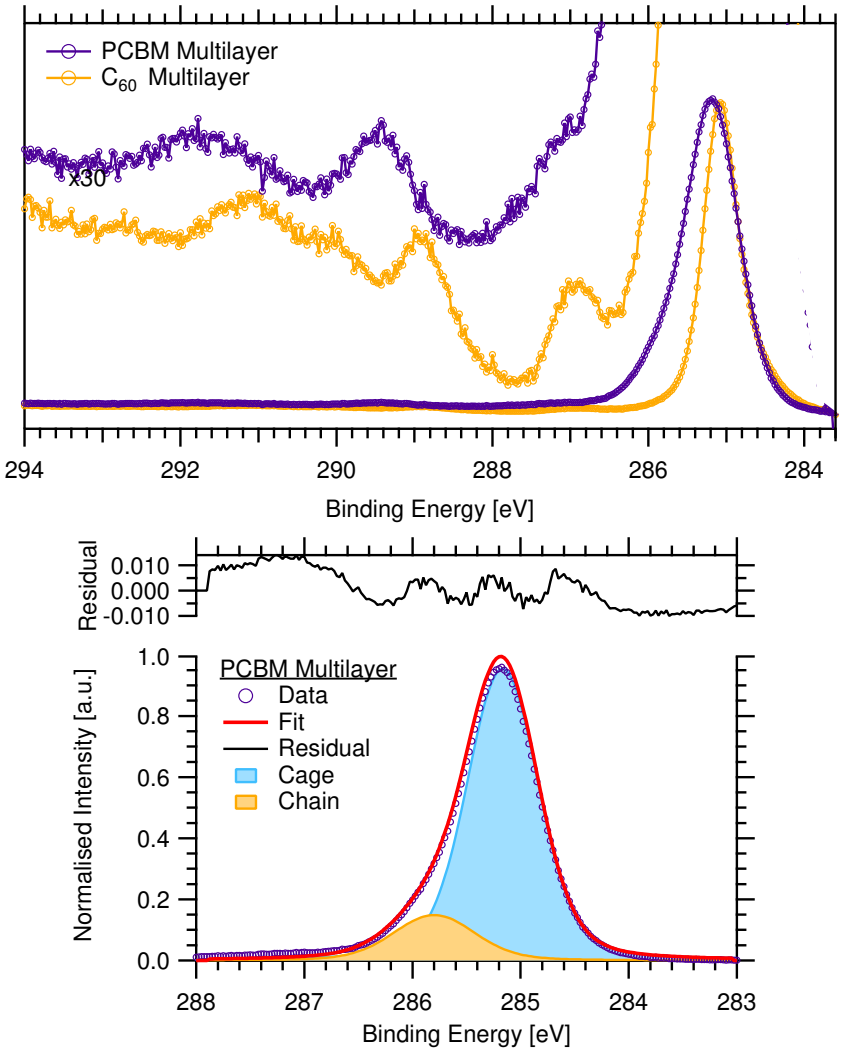


Figure 6.5: C 1*s* spectra of multilayers of PCBM and C_{60} measured on I311 showing the shake-up structure of both molecules. Peak fitting of the PCBM spectra is included below which produced normalised area's of 0.85 and 0.15 matching the stoichiometry of the molecule. Both spectra were measured at $h\nu = 340$ eV.

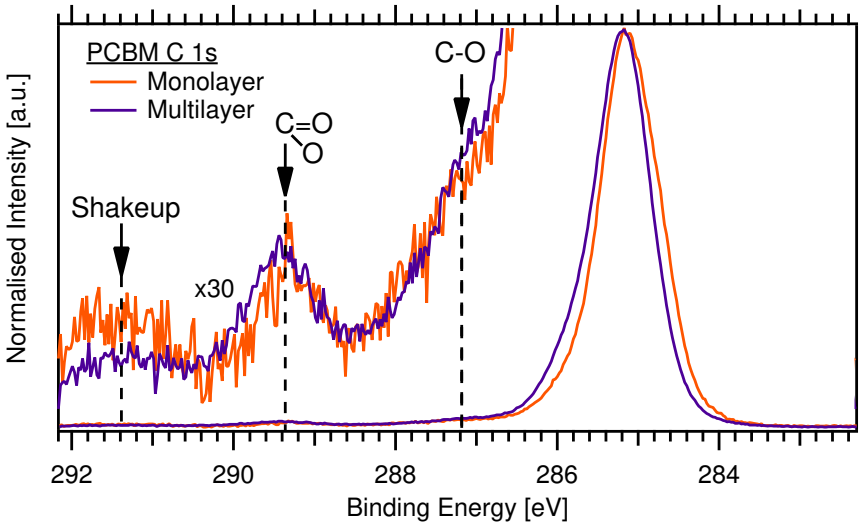


Figure 6.6: C 1*s* spectra of monolayer and multilayer coverages of PCBM on Au(111). Measurement were taken on I311 using an photon energy of $h\nu = 340$ eV. Both spectra have had a linear and Shirley background subtracted.

6.3.2 Density of states

XAS of PCBM was measured at D1011. Which can be combined with valence band XPS to produce density of states plots where the XAS is placed on a common binding energy scale via the method discussed in Chapter 2.5.2 and elsewhere [123]. Density of states for PCBM is included in Figure 6.8. Multilayer and monolayer valence band spectra are included but only multilayer XAS (the monolayer and multilayer NEXAFS are identical). A comparison density of states plot for a C_{60} multilayer is shown in Figure 6.9. For both molecules these plots show that the LUMO (lowest unoccupied molecular orbital) overlaps with the surface's Fermi edge (0 eV binding energy) so charge transfer from the surface to the LUMO could be possible. The valance band XPS data is discussed in the previous section. The NEXAFS gives an indication of the positions of the unoccupied molecular orbitals. It is worth noting that the measured NEXAFS doesn't necessarily represent the true density of states of the sample: not all states may be accessible to x-ray absorption due to the dipole selection rules and the measurement is in the core excited state where the existence of the core hole can cause shifts in the measured orbital position [159].

The valance band XPS data is discussed in the previous section. The

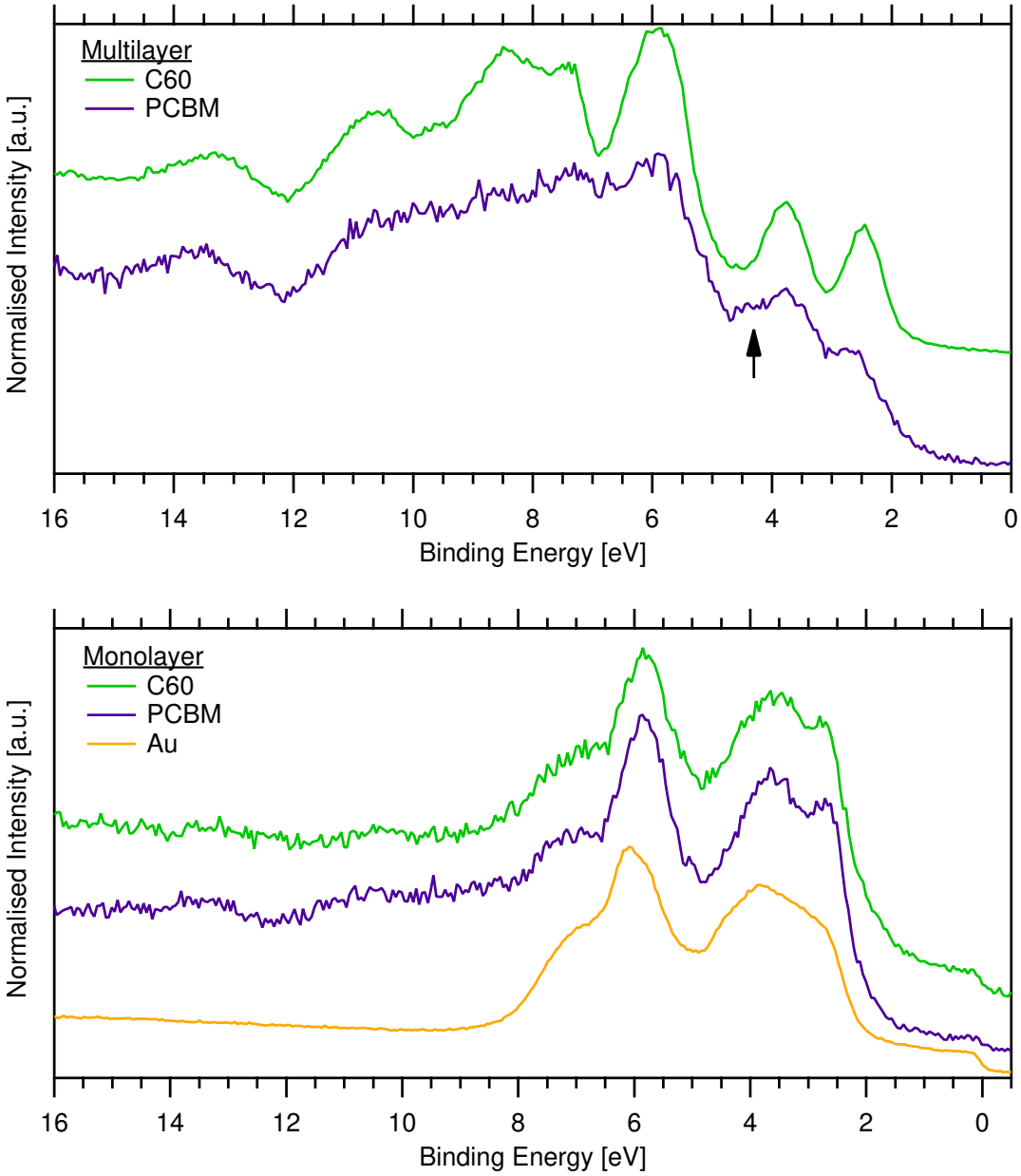
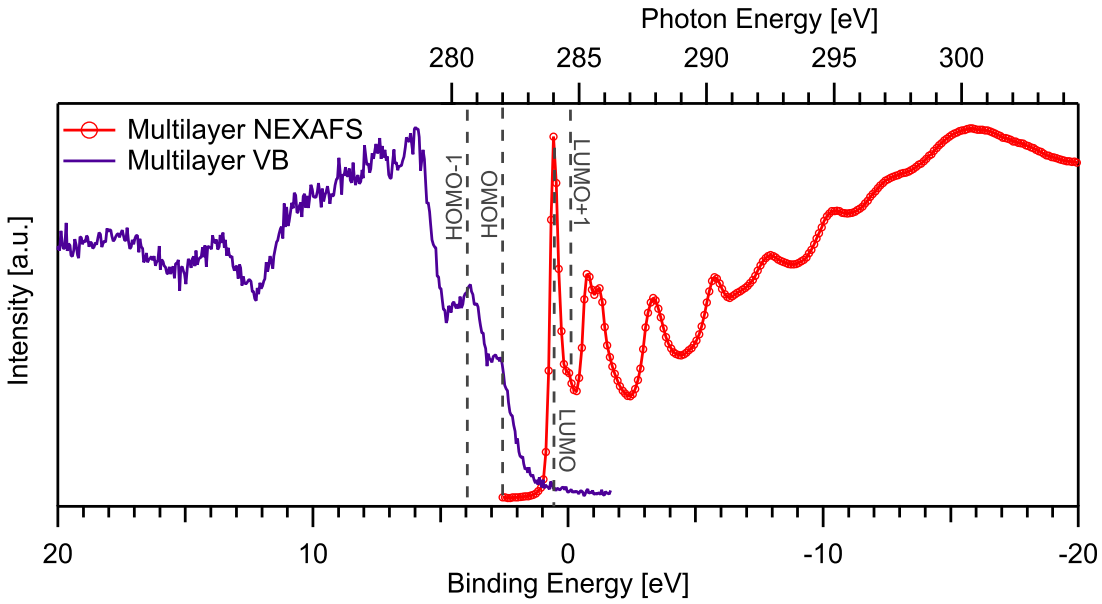
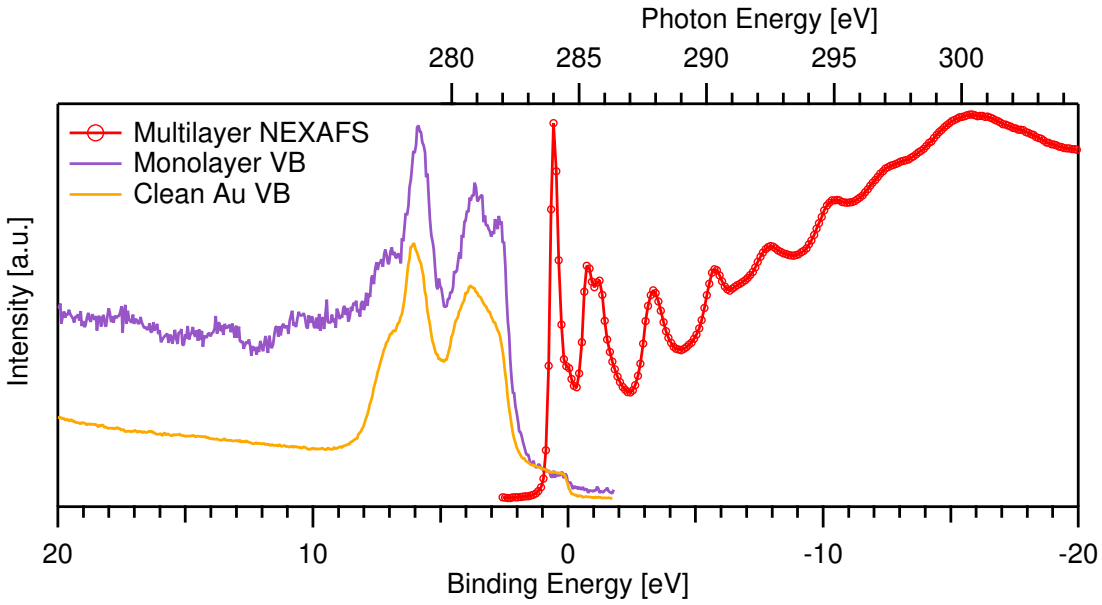


Figure 6.7: Valence bands of PCBM and C_{60} multilayer and monolayer coverages on Au(111). All were measured using $h\nu = 50$ eV light on I311. The arrow indicates some intensity that can not be attributed to the C60 cage.



(a) PCBM multilayer



(b) PCBM monolayer

Figure 6.8: Density of states plots of, (a) PCBM multilayer and (b) PCBM monolayer on Au(111) produced by combining valence band XPS and XAS. Valence bands were measured at $h\nu = 50$ eV.

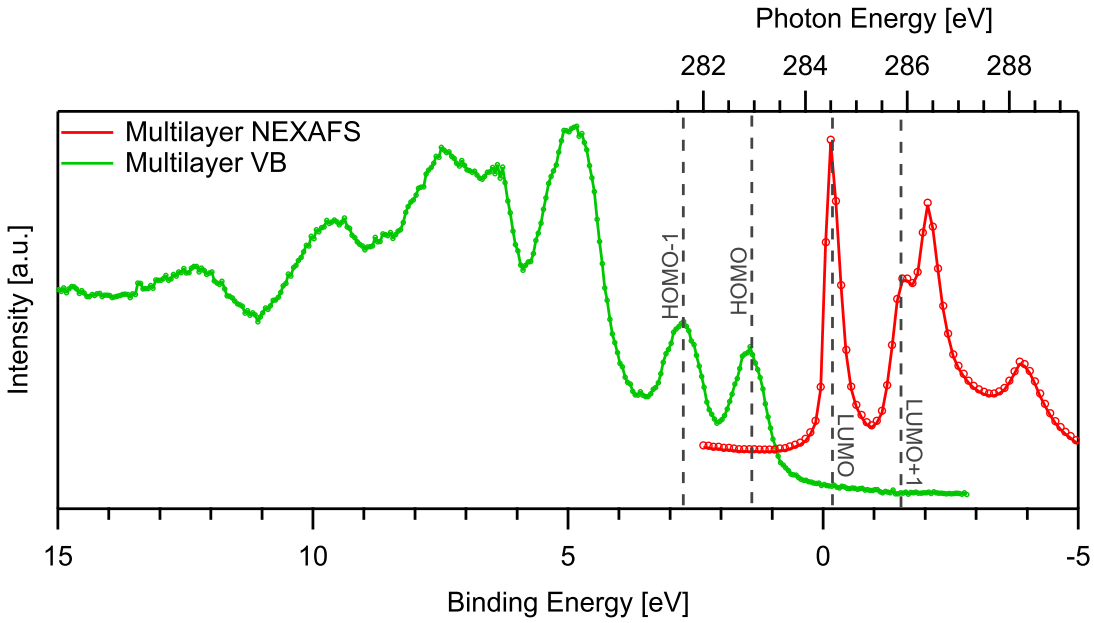


Figure 6.9: C_{60} multilayer density of states plot. The valance band XPS was measured at $h\nu = 50$ eV.

6.3.3 Resonant photoemission

RPES maps of a monolayer, multilayer and an intermediate coverage of PCBM are included in Figure 6.10. There is very little change in the map as the coverage increases. The stand-out feature is the very strong participator enhancement near the HOMO-1 (BE∼4 eV) at the LUMO+1 resonance ($h\nu = 285.5$ eV), which ignoring the HOMO-1 enhancement is a very weak state. This feature is examined further in Figure 6.11 using the multilayer dataset where we have zoomed in on the region and taken line profiles at key photon and binding energies. The pink dashed lines show resonant photoemission of the valence band on the LUMO (284.5 eV), LUMO+1 (285.1 eV) and LUMO+2 (285.9 eV) resonances. An "off resonance" line between the LUMO+1 and LUMO+2 at 285.5 eV is also shown. Vertical line profiles are also included showing NEXAFS spectra constructed with electrons from the HOMO, HOMO-1 and HOMO-2 states (indicated by red arrows). These are compared to the NEXAFS spectra extracted from the Auger region which should effectively represent partial electron yield. All of these line profiles are plotted out below the RPES map where the resonant photoemission intensity is taken directly from the RPES MAP. The constant binding energy (constant initial state) NEXAFS have been normalised to the height of the LUMO peak.

Firstly, considering the resonant photoemission spectra, it can be seen that the LUMO+1 state (see the green line) only couples with what appears to be the HOMO-1 (peak at $BE = 4$ eV). However comparing the position of this

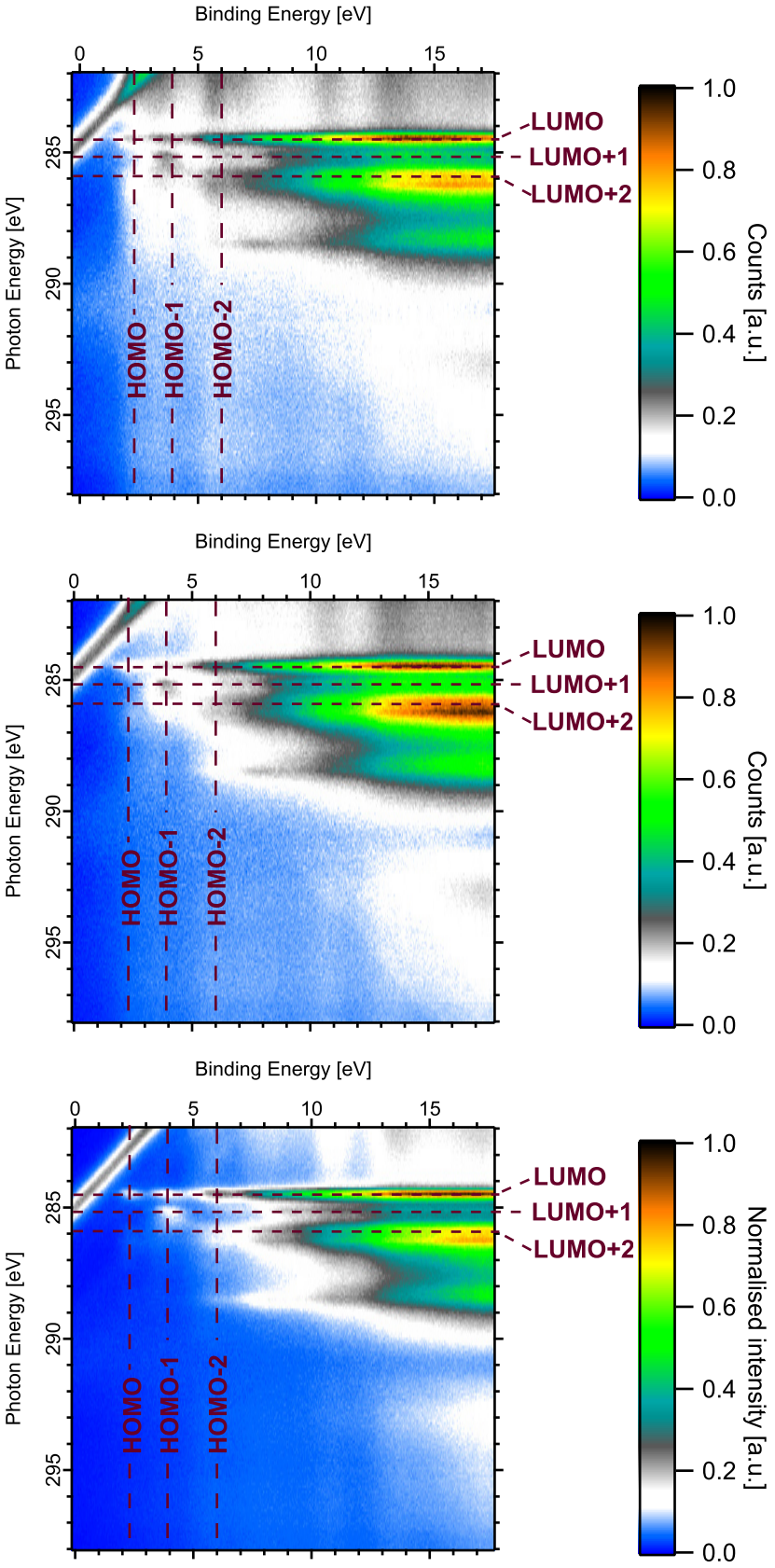


Figure 6.10: RPES maps of PCBM on Au(111) measured over the C K edge increasing in coverage from monolayer (top) to multilayer(bottom).

enhancement with the participator enhancement of the HOMO-1 at the LUMO (blue line) and LUMO+2 (purple line) resonance, the LUMO+1 enhancement appears at a slightly higher binding energy. This is comparable to the feature observed in the valence band (Figure 6.7) where a small amount of intensity slightly above the HOMO-1 was attributed to being a state on the ligand rather than the fullerene cage (see Section 6.3.1). Given this state only seems to be enhanced at the LUMO+1 resonance, it implies that the LUMO+1 is also located exclusively on the ligand and not the fullerene otherwise one would expect to see enhancements of this state at other resonances. This assignment is consistent with Richter's PCBM resonant photoemission study [103].

It is also interesting that this feature continues beyond the LUMO+1 resonance for quite some distance and appears to drift to high binding energy with increasing photon energy. The intensity has hardly diminished when between the LUMO+1 and LUMO+2 resonances (see the red line) and does not decrease much until we reach the LUMO+2, where the feature at $\sim$4 eV binding energy is broadened out and has shifted back to the slightly lower binding energy of the the true HOMO-1. At the LUMO+2 energy we start to see coupling with the HOMO. This is again consistent with the state of this LUMO+1 enhancement being separated from the other molecular states (both occupied and unoccupied). The shape of the feature is consistent with vibronic coupling, which has been previously observed for C_{60} using resonant photoemission [160]. It is also possible that the participator enhancement of the HOMO at the LUMO resonance shows a similar asymmetry and drift to higher binding energy, but a higher resolution map would be required to make that claim definitively.

The second noteworthy observation in the monolayer (top) map presented in Figure 6.10 is the lack of super-spectator or super-Auger decay lines which, if present, would manifest themselves as constant kinetic energy diagonal lines in the RPES map. This is particularly significant given that the density of states at a first glance shows overlap between the LUMO and the Fermi edge, and given that we have previously shown C_{60} on Au(111) to present these features [33, 34]. There are however a couple of experimental differences between this previous C_{60} work and this study: Firstly, the samples in this study were prepared by electrospray deposition and the previous work by sublimation from a Knudsen-cell. Secondly, the monolayer in the previous work was achieved by depositing a multilayer and carefully heating the sample to desorb all but the single layer of molecules physisorbed to the surface. To address the possibility that the sample preparation may be significant two different C_{60} monolayer samples were prepared using electrospray. Firstly we simply deposited until the coverage resembled a monolayer

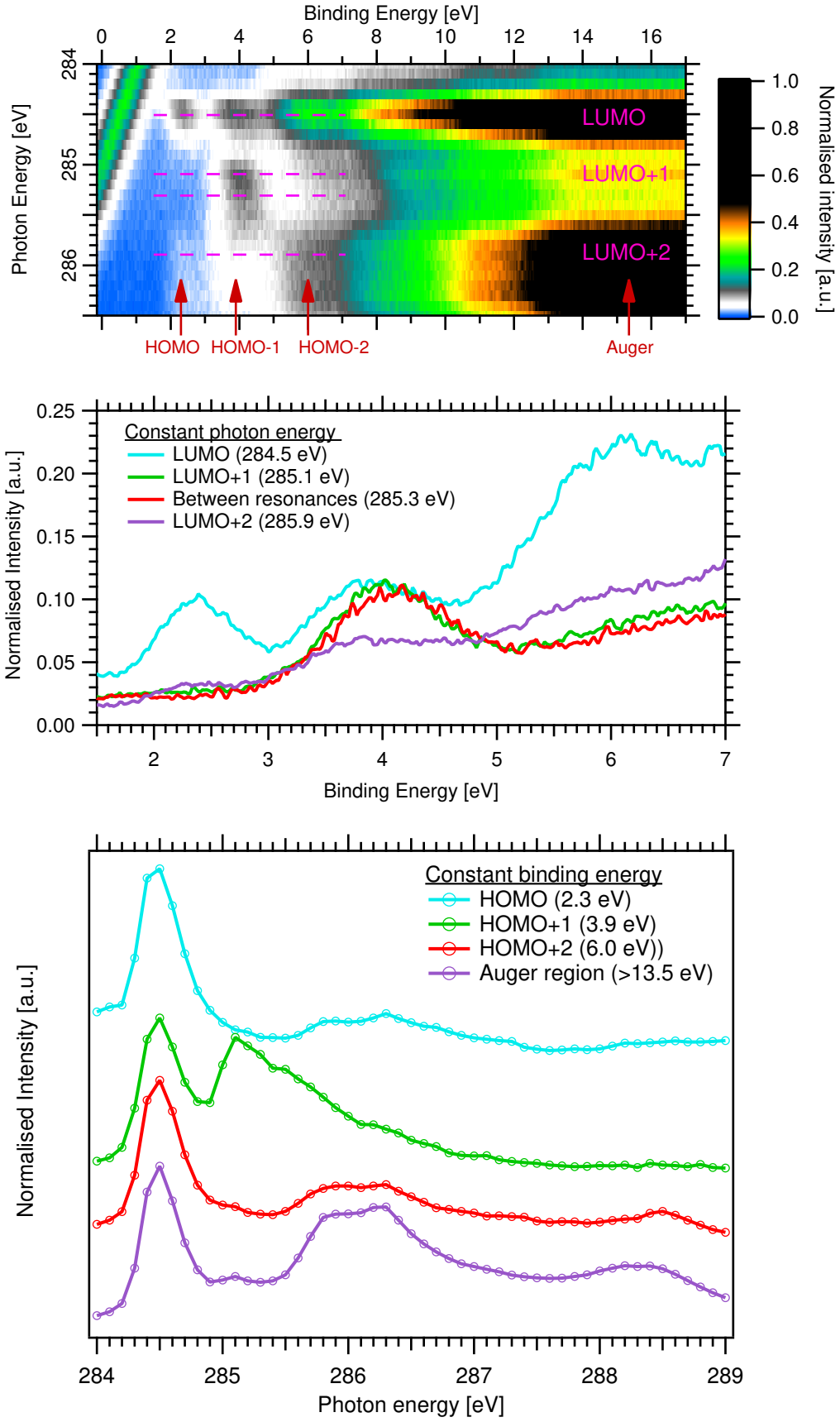


Figure 6.11: The participator region of the PCBM RPES map along with constant photon energy and constant binding energy line profiles exploring the enhancement at the LUMO+1 resonance of a feature near the HOMO-1.

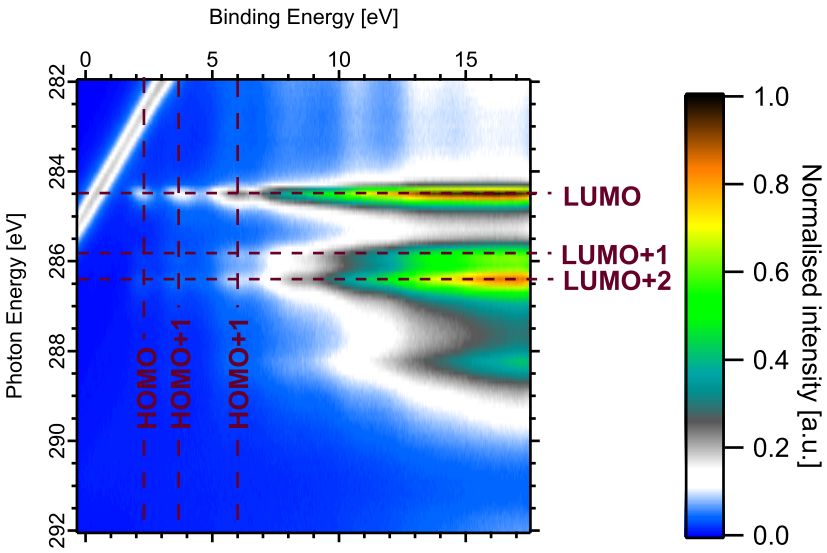
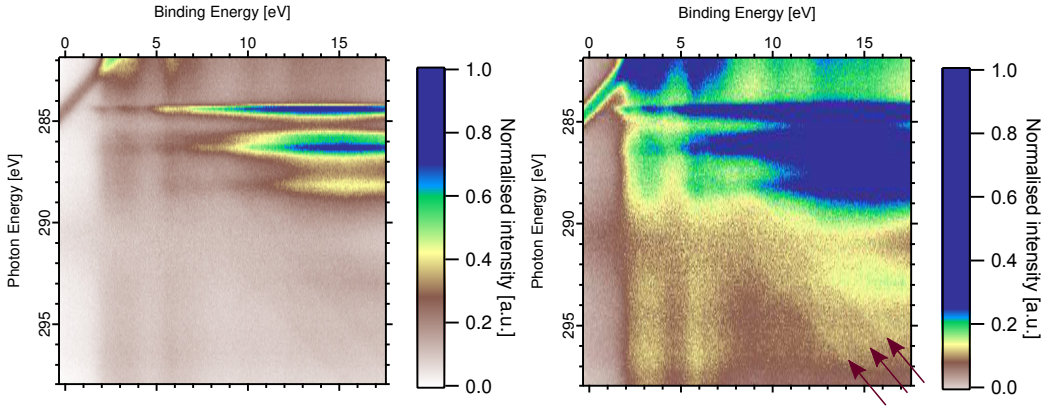


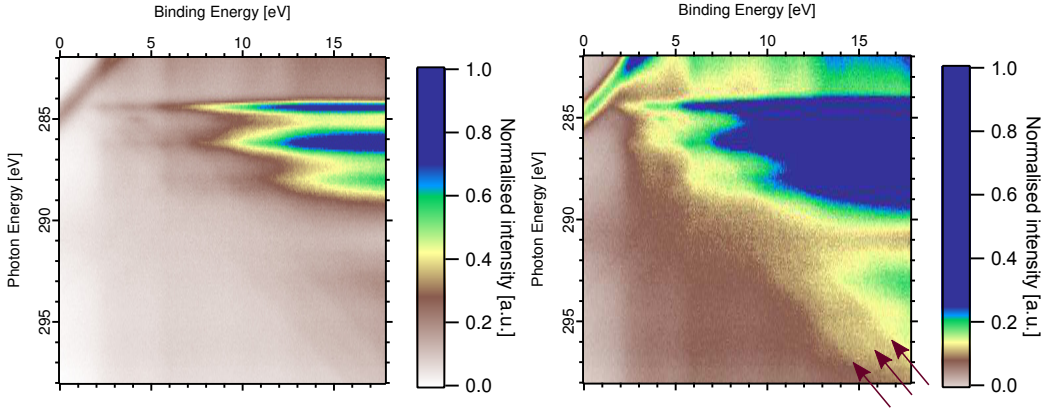
Figure 6.12: RPES map of a C_{60} multilayer.

(referred to as "direct preparation"). Secondly, we deposited a multilayer, where after measuring it, the sample was heated to desorb the multilayer leaving behind a monolayer (referred to as a "desorbed multilayer").

C_{60} RPES maps are presented in Figure 6.12 for the multilayer and in Figure 6.13 for both monolayer preparations. In each case the same map is shown twice with different intensity/colour scales. In both the direct and desorbed monolayer cases, as indicated in the figure with arrows, we see constant kinetic energy features consistent with super-spectator/super-Auger decay. For reference Figure 6.14 shows the RPES map for the PCBM monolayer is shown, with the same colour map scaling, where no constant kinetic energy features are visible. It follows that the lack of these features for PCBM is real and not as a result of the sample preparation technique (such as the annealing of the film).



(a) Direct preparation **(b)** Direct preparation



(c) Desorbed multilayer **(d)** Desorbed multilayer

Figure 6.13: RPES maps showing monolayers of C_{60} on Au(111) prepared using electrospray by (a,b) direct deposition and (c,d) by desorbing a multilayer. Two intensity scales are included to highlight the presence of super-spectator/super-Auger features (labelled with arrows.)

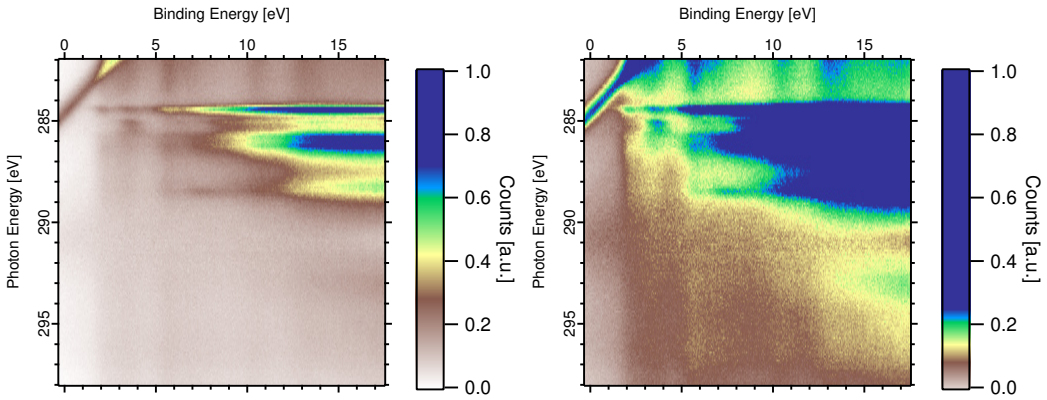


Figure 6.14: RPES map of a monolayer of PCBM on Au(111).

6.4 P3HT

6.4.1 XPS

C 1s spectra for monolayer and multilayer coverages of P3HT on Au(111) are shown in Figure 6.15. Both were collected on I311 and have had a linear background subtracted. In both cases the data shows a single peak but with the multilayer spectrum shifted to slightly higher binding energy by 0.27 eV due to charging. The inset shows the multilayer spectra shifted down by this amount showing the peak shapes are very similar. The slight increase in intensity on the lower binding energy side of the monolayer peak is likely due to some minor contamination on the surface due to the increased base pressure during deposition. It is possible to fit three peaks corresponding to carbon environments in the molecule, C-S in the thiophene, C-C in the thiophene and C-C in the alkane chain with areas that match the stoichiometry of the molecule. However, given the spectra just contains a single peak, there is little evidence in the data to suggest any one of the many possible fits are correct so fitting is not included here. The two carbon environments in the thiophene backbone would be distinct, but side ligands adds a third carbon environment between the two thiophene peaks making them unresolvable [161].

The S 2p spectra are included in Figure 6.16 again having had a linear background subtracted. The multilayer and monolayer spectra are again similar shapes but with a shift towards higher binding energy for the multilayer. This is most likely due to charging. The inset shows the same data, with the multilayer spectra shifted in X by the separation of the C 1s peaks in Figure 6.15, showing there is a slight change in shape. This could perhaps be caused by degradation of the molecule by oxidation - other studies have shown the degradation of P3HT by exposure to UV light [147], ozone [162] and water [148] to be evident in the S 2p. It is unlikely to be due to an interaction with the surface as for sexithiophene (a polythiophene with no ligand group) the S 2p has been shown to not change shape with film thickness [161].

The valence bands are shown in Figure 6.17 for the multilayer and monolayer coverages. The valence band of the clean Au(111) surface is included for reference. Unlike the fullerene molecules, the P3HT features are very broad making it difficult to accurately identify positions of individual molecular orbitals.

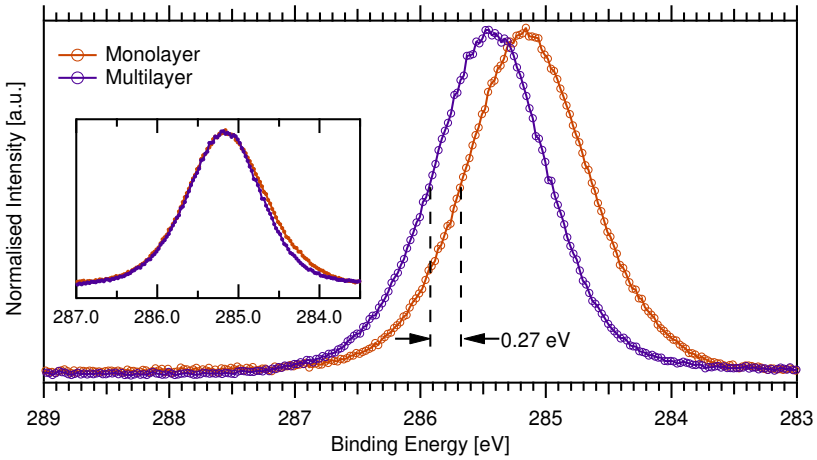


Figure 6.15: C 1*s* spectra of multilayer and monolayer coverages of P3HT on Au(111). Both spectra were collected at I311 with $h\nu = 340$ eV. The inset shows a -0.27 eV shift applied to the multilayer spectrum.

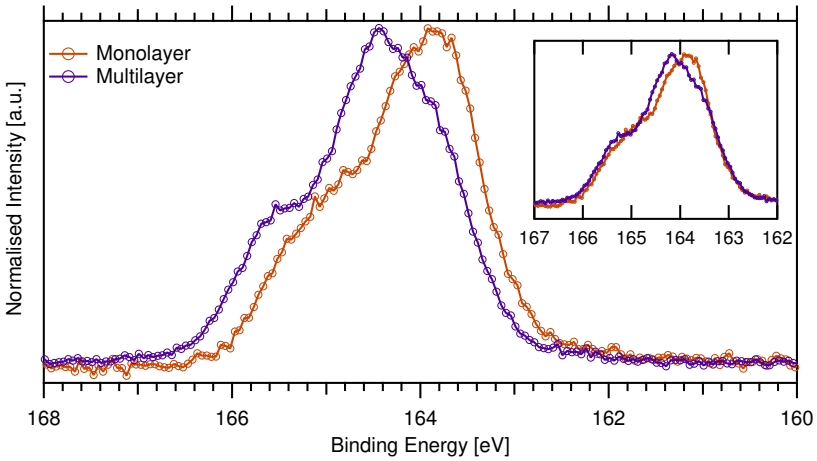


Figure 6.16: S 2*p* spectra of multilayer and monolayer coverages of P3HT on Au(111). The inset shows a -0.27 eV shift applied to the multilayer spectrum (the offset measured between C 1*s* spectra). Both spectra were collected at I311 with $h\nu = 220$ eV

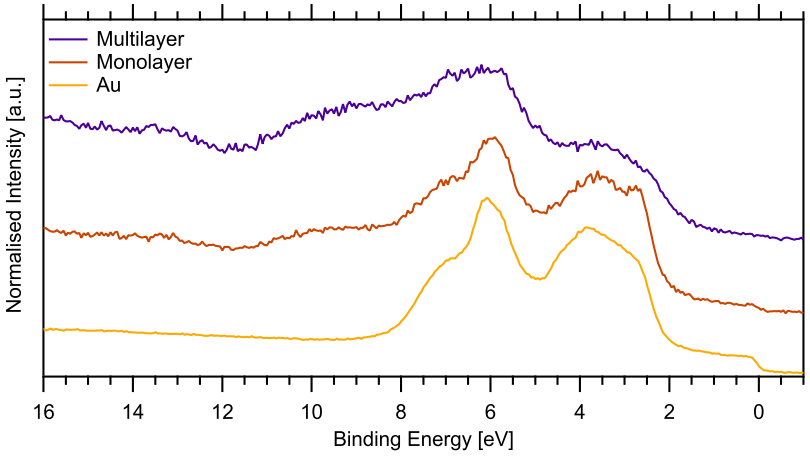


Figure 6.17: Valence band XPS (measured at I311 with $h\nu = 50$ eV) of multilayer P3HT, monolayer P3HT and the clean Au(111) surface.

6.4.2 Density of states

As before, NEXAFS can be mapped onto a common binding energy scale with the valence band to give show the relative position of occupied and unoccupied states. For the multilayer this is shown in Figure 6.18. In the NEXAFS there is only one clear π^* peak - at higher photon energies the features are much broader, consistent with σ^* resonances. This is consistent with other angle resolved NEXAFS measurements [146] that assign the LUMO peak at ∼285 eV to be the C $1s \rightarrow \pi^*$ transition from atoms in the thiophene backbone, the peak at ∼287 eV to C-H and C-S σ^* orbitals and the peak at ∼284 eV to be C-C σ^*. DFT simulations of the molecule show no LUMO density on the ligand [146].

6.4.3 Resonant photoemission

C $1s$ RPES maps for three different coverages of P3HT on Au(111) are included in Figure 6.19, including monolayer (top), multilayer (bottom) as well as an intermediate coverage. These maps again show some participator enhancement, which is explored further for the monolayer and multilayer in Figures 6.20 and 6.21 respectively. Here horizontal and vertical line profiles have been extracted from the maps to show resonant photoemission of the valence band and NEXAFS constructed from electrons with a specific initial state. The NEXAFS plots are constructed from electrons from the HOMO and HOMO-1 states and compared to the region dominated by carbon Auger emission (marked with black arrows). The photoemission is measured on resonance with the LUMO and LUMO+1 as well as a spectra inbetween the two resonances (marked with dashed lines). The intensities in the photoemission graphs directly represent the intensity from the

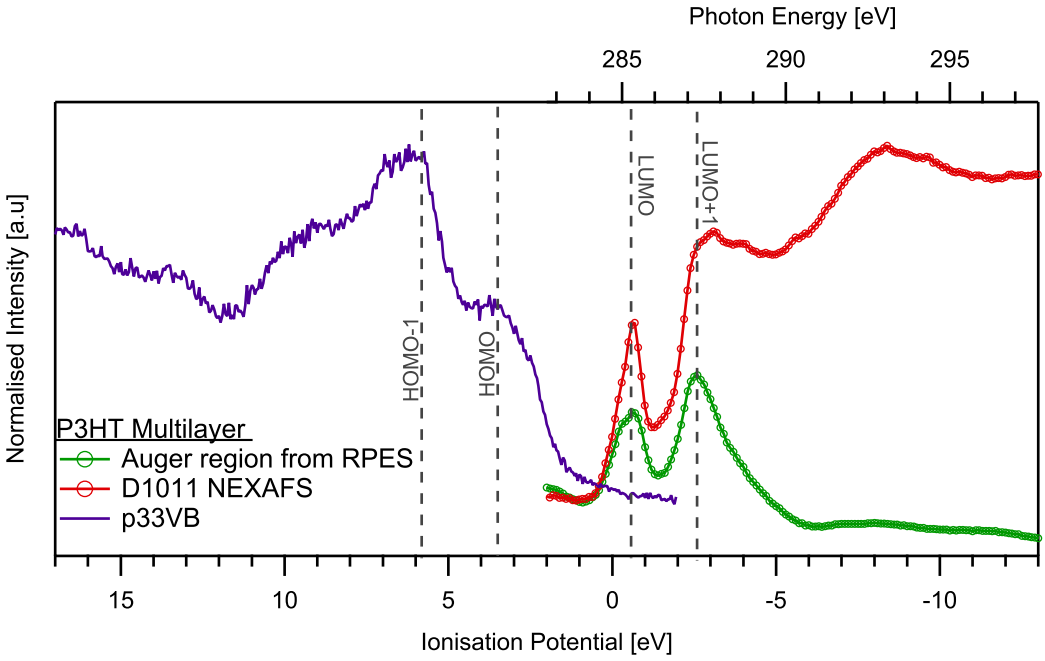


Figure 6.18: Density of states plot for a P3HT multilayer. As well as the valence band, XAS measured using the PYD at D1011 along with NEXAFS extracted from the Auger region of multilayer RPES map.

RPES maps. In the case of the monolayer resonant photoemission graph, a linear background has been subtracted to allow comparison of the feature heights. For the multilayer case, a background subtraction was not necessary but the spectra have been shifted vertically so they have the same baseline.

In both cases, there is participator enhancement of the HOMO at the LUMO resonance. However the spectra do not imply any strong coupling between the LUMO and the HOMO-1. In the monolayer, it at first looks like there is a strong enhancement of the HOMO-1 at the LUMO+1 resonance. However, comparing the intensity of the HOMO and HOMO-1 features on the LUMO+1 resonance (purple line) with the spectra between resonances (yellow line), shows the majority of this apparent enhancement is just due to the feature sitting on top of the gold valence band. In the multilayer, there is some increase of the HOMO-1 intensity at the LUMO+1 resonance that is not present on the LUMO resonance or between resonances.

For both coverages, there is a potential enhancement just below the LUMO+1 at the HOMO. This can be seen in the NEXAFS constructed with electrons from the HOMO (blue line - the dashed line show this 5x magnified) as a peak appearing $\sim$0.5 eV below the LUMO+1 (visible in the other two spectra).

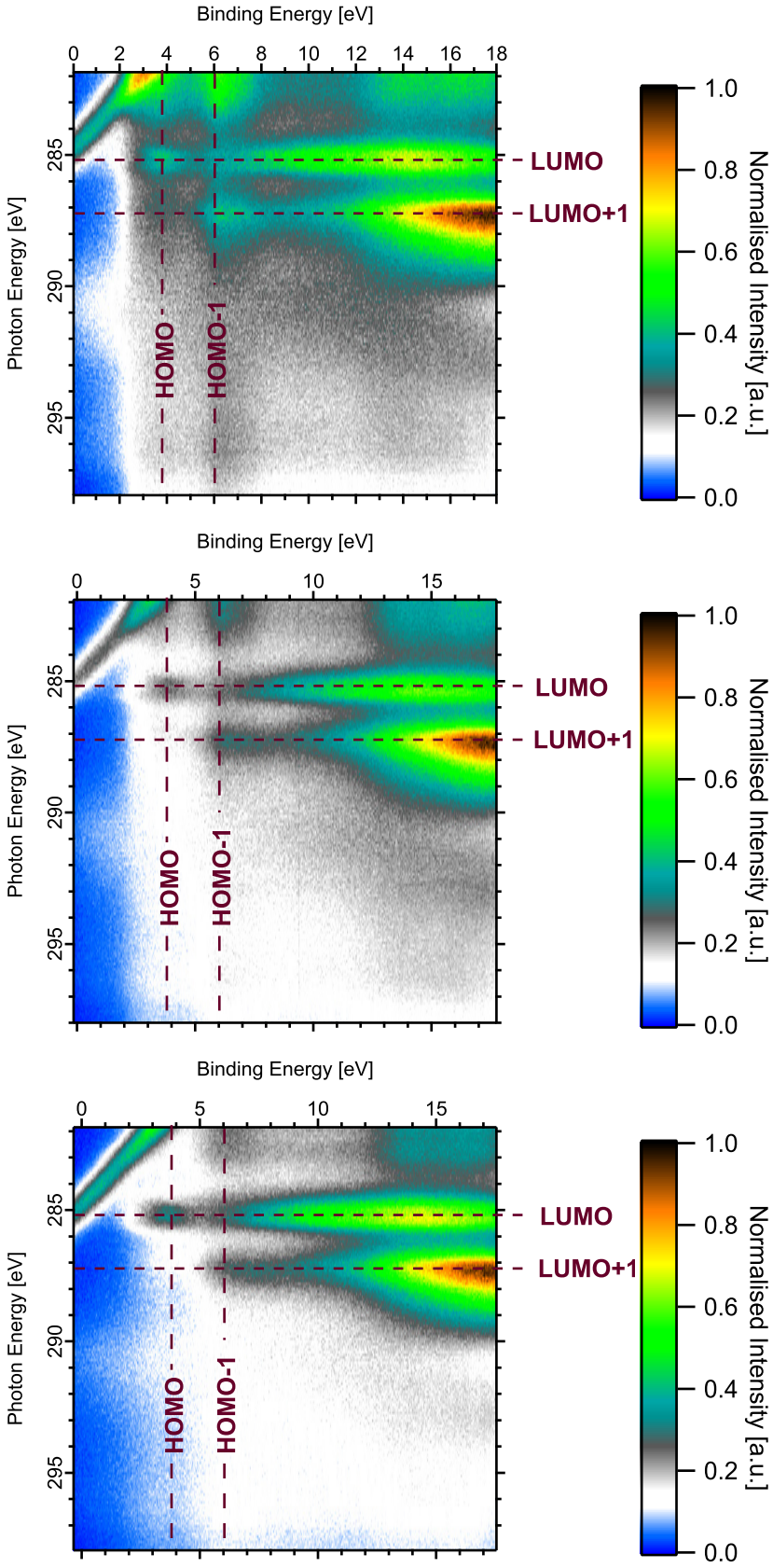


Figure 6.19: RPES maps, measured over the carbon K edge, of P3HT on Au(111) increasing in coverage from monolayer (top) to multilayer (bottom)

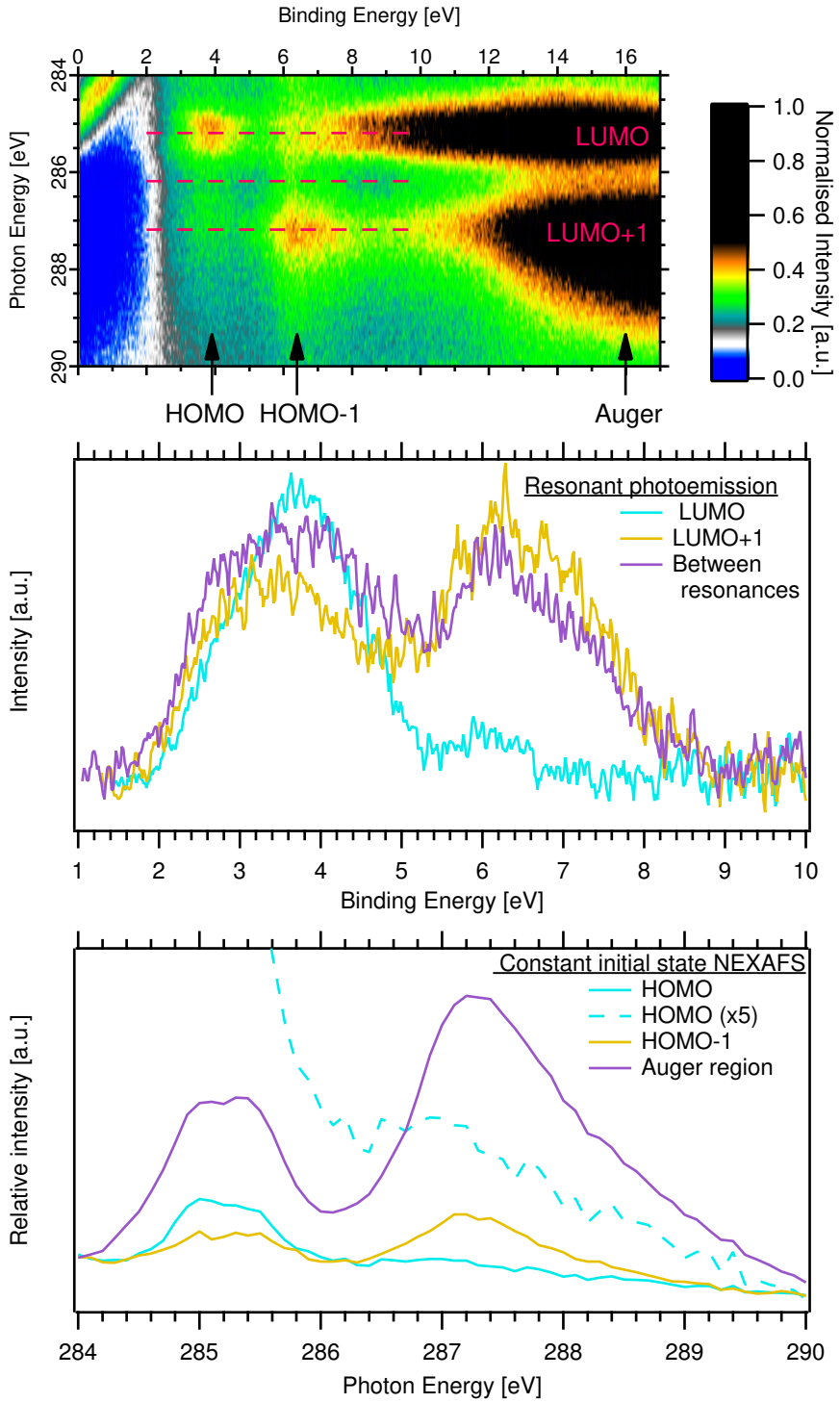


Figure 6.20: P3HT monolayer RPES map zoomed in on the participator regions with constant photon energy and constant binding energy line profiles extracted to explore potential enhancements.

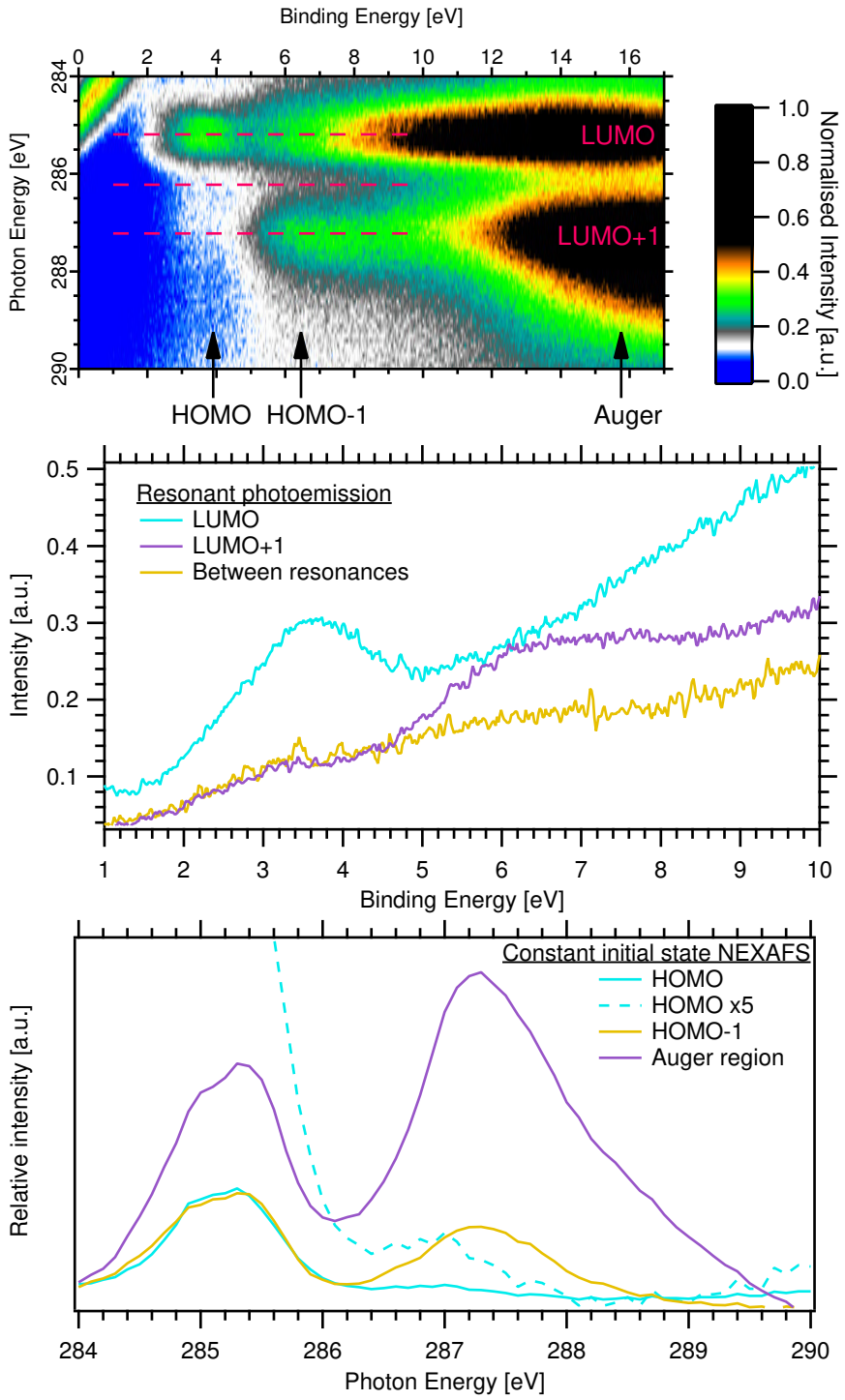


Figure 6.21: P3HT multilayer RPES map zoomed in on the participator regions with constant photon energy and constant binding energy line profiles extracted to explore potential enhancements.

6.5 Bi-layer: P3HT on PCBM

A thick film of PCBM was deposited onto Au(111) and P3HT was deposited on top, all in-situ using electrospray at I311. The aim was to see if RPES shows any evidence of charge transfer between the two organic films.

6.5.1 XPS

Binding energy calibration was problematic for this dataset. Firstly comparing exact binding energy positions is almost meaningless due to the simultaneous variation in thickness of both layers causing an unpredictable level of steady state charging. Additionally, the gold signal is buried under the film so there is no reference, and we unfortunately did not measure the gold Fermi edge or core level elsewhere on the crystal between every scan. The peak shape and relative shifts can however be examined but the precise binding energy values presented here are inaccurate.

In order to get a feel for the four different P3HT coverages measured, looking at the valence band gave the best indication as it contains distinct features from both molecules in the same spectra. Figure 6.22 shows valence bands of the thick PCBM multilayer, coverages 1 to 4 of P3HT and a "pure" P3HT multilayer for reference. The coverages are numbered in order of increasing intensity of the P3HT features in the valence band relative to the PCBM features. This was predominately judged by the strength of the characteristic HOMO and HOMO-1 PCBM peaks at ∼2.5 eV and ∼4 eV respectively (marked with dotted lines). The spectra were pseudo-calibrated by manual alignment to the previously calibrated P3HT and PCBM spectra meaning shifts in the entire spectra would not be visible.

Uncalibrated S $2p$ data is shown in Figure 6.23. The first observation is that the doublet consists of two sharp peaks whereas for the P3HT multilayer there is some broadening or perhaps sub-structure. This indicates either the resolution has increased, or in both the monolayer and multilayer films presented in Section 6.4, there was a chemical iteration, possibly with the Au surface, smearing out the doublet; the effect of which is quenched when the P3HT is grown on the PCBM film.. The second interesting feature is the slight increase in intensity of the 4th coverage (orange dots) between the doublets (marked with an arrow at ∼165 eV) and on the lower binding energy of the S $2p_{3/2}$ peak (∼163.5 eV). This represents the greatest coverage of P3HT and is perhaps consistent with the shape presented in the multilayer spectrum (purple dots). Unfortunately as the energy axis is

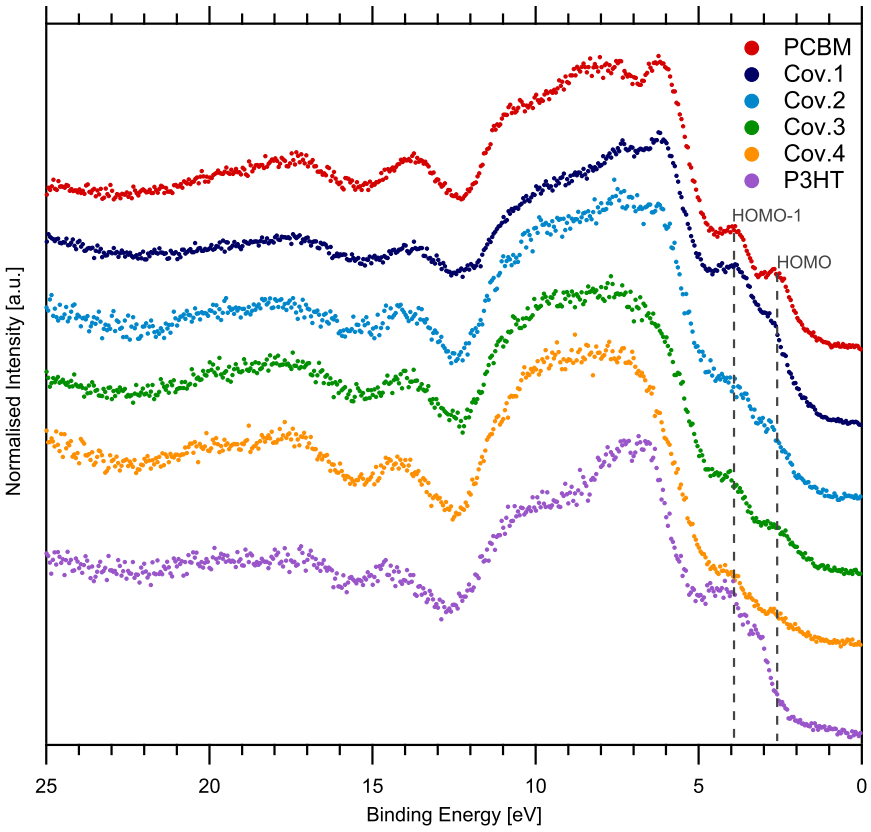


Figure 6.22: Valence band XPS of 4 coverages of P3HT grown on a thick multilayer of PCBM (also shown). The valence band of a P3HT multilayer is also included for reference. All spectra were measured with $h\nu = 50$ eV. Dashed lines show the position of the PCBM HOMO and HOMO-1.

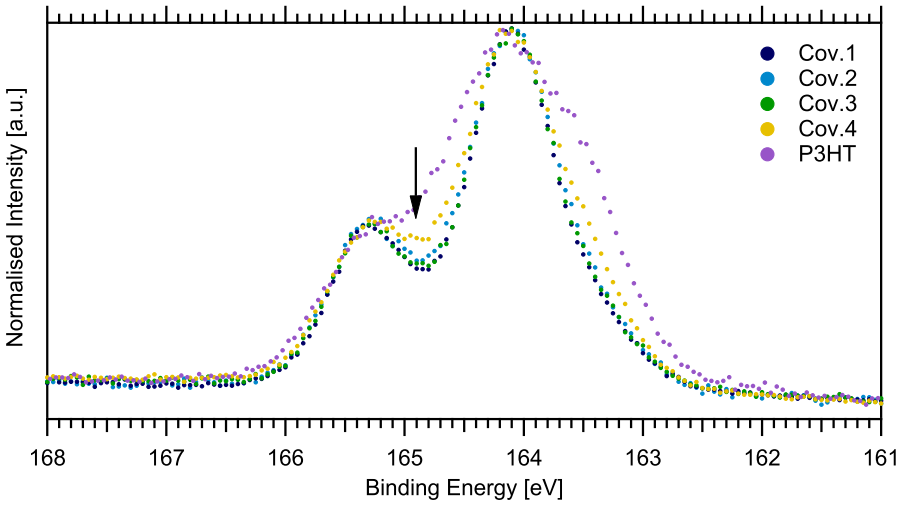


Figure 6.23: S 2*p spectra* of the four coverages of P3HT grown on a thick multilayer of PCBM (also shown). Spectra measured at $h\nu = 220$ eV.

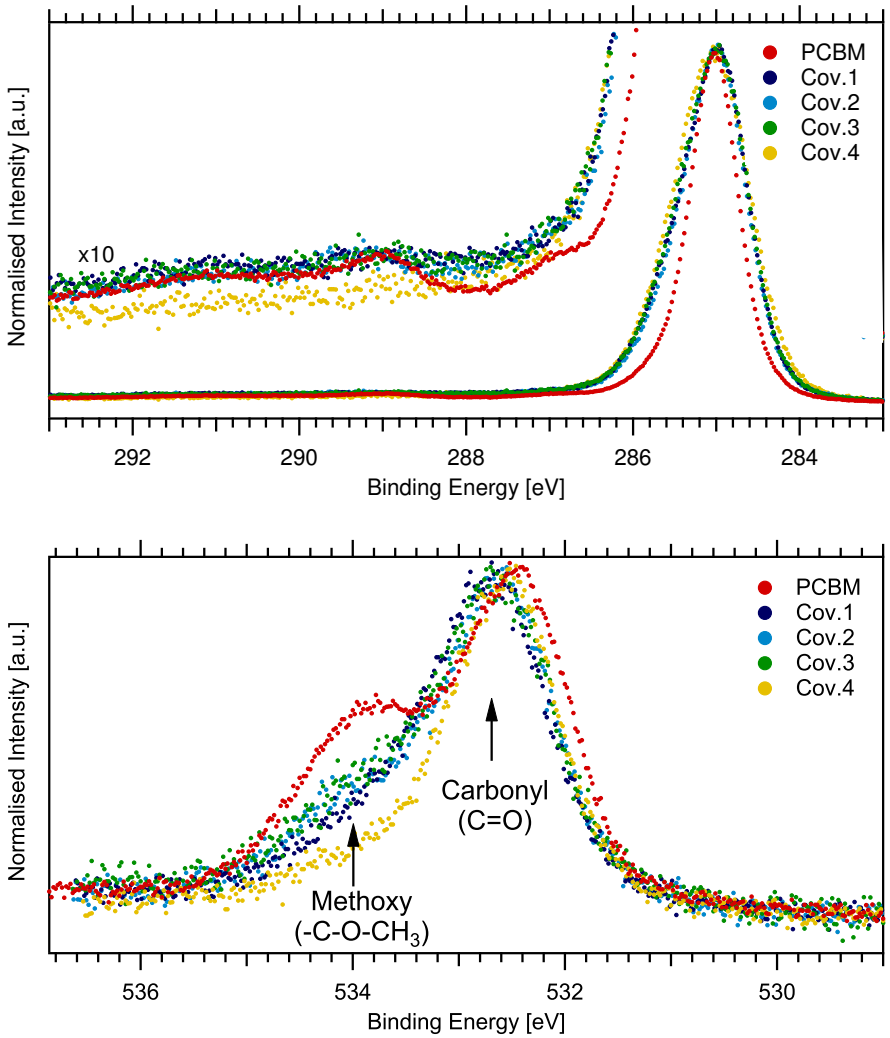


Figure 6.24: C 1*s* (top) and O 1*s* (bottom) spectra collected for 4 coverages of P3HT on top of a thick multilayer of PCBM. Both spectra were measured at $h\nu = 650$ eV and the carbon shifted to be centred at $BE = 285$ eV. The same shifts were applied to the O 1*s* spectra.

calibrated, this can not be concluded with certainty - careful calibration to the vacuum level would be required to make this claim.

Figure 6.24 includes C 1*s* and O 1*s* spectra for the same 4 coverages. These were both measured at the same photon energy of 650 eV so the relative position between each C 1*s* and its corresponding O 1*s* is therefore meaningful. The C 1*s* peaks were manually positioned to be centred at 285 eV binding energy and the same shifts applied to the corresponding O 1*s*. In the C 1*s* there is very little variation in shape where every coverage has a similar shape. The shake-up structure and carbon-oxygen peaks behave as expected, where the thicker the film the weaker this structure (which originates from the PCBM).

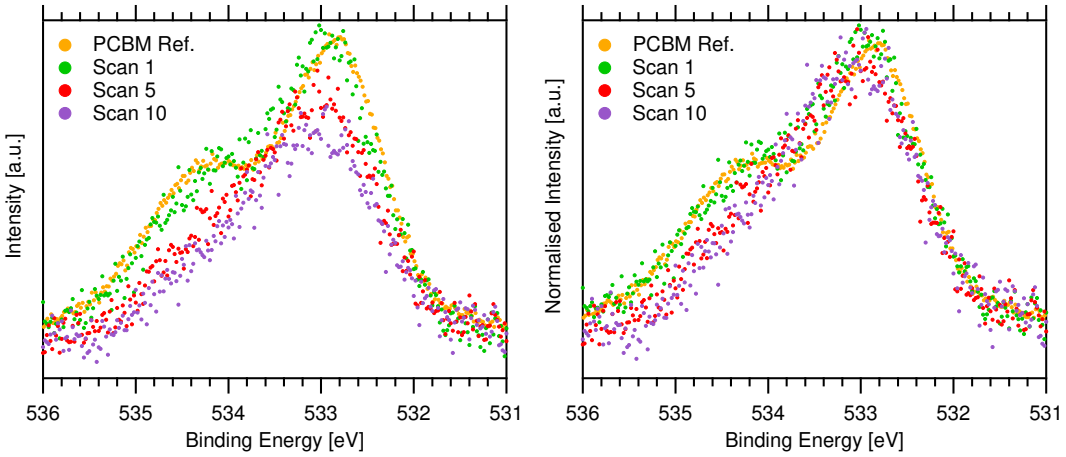


Figure 6.25: Beam-damage study for the PCBM P3HT bi-layer measured at I311. 10 consecutive scans (the first middle and last are shown) over the O 1s region on an area of previously unmeasured sample measured at $h\nu = 650$ eV. The original PCBM spectra is included for reference. The left plot shows the intensity drop with exposure time and the right plot shows the same spectra normalised allowing comparison of the shape.

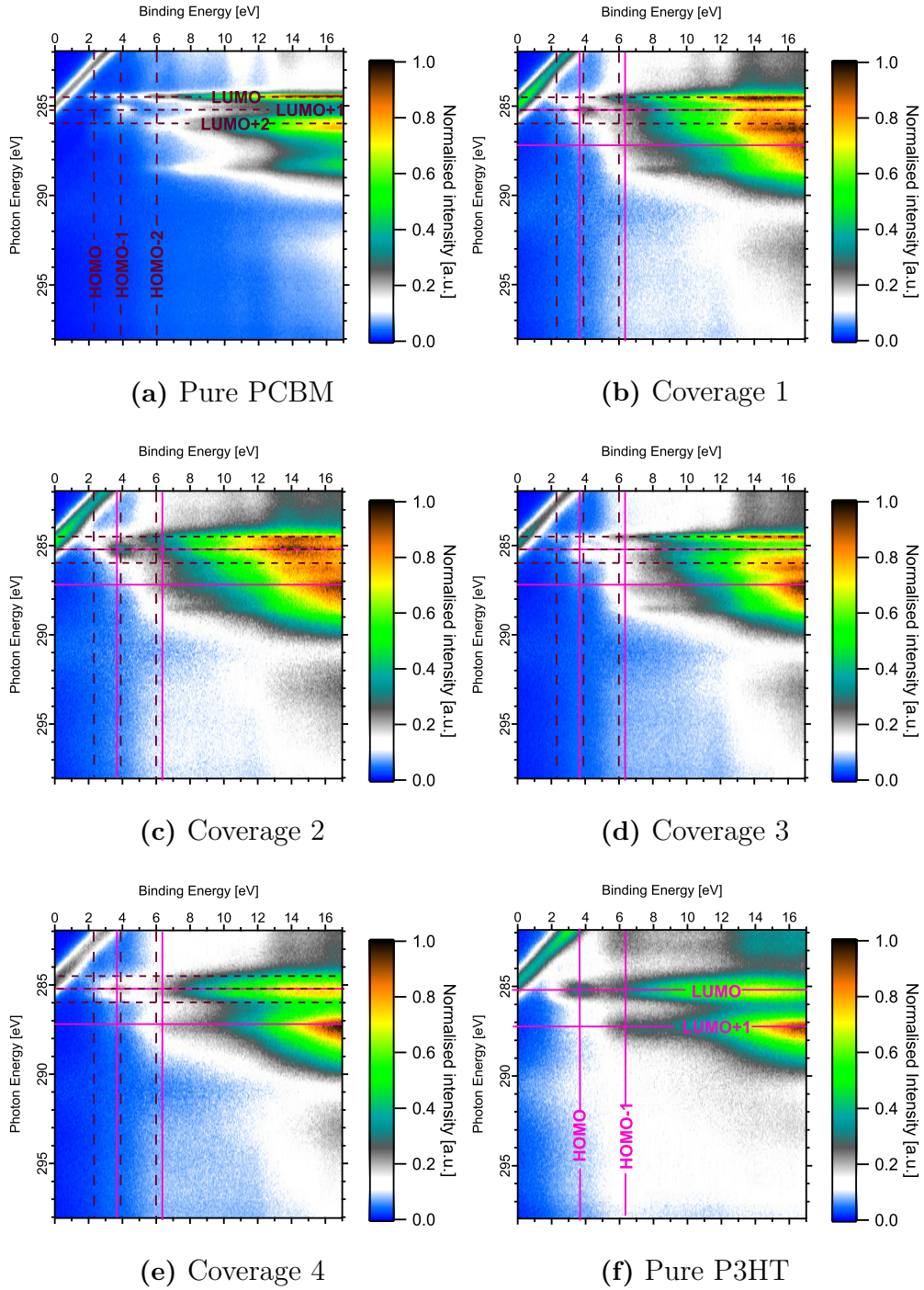
The O 1s in Figure 6.24 shows a large variation in the relative size of the methoxy peak (higher binding energy) compared to the carbonyl peak (lower binding energy). There is no trend between the decrease of the methoxy signal with P3HT thickness but it is a significant decrease in all four cases. Beam-damage would not account for this alone as there is no correlation with the duration of light exposure before the O 1s measurements. For example, coverage 2 (pale blue points) and the original PCBM multilayer (red points) were both one sweep with the same dwell time, with the same exposure prior to measurement of the spectra (a single wide scan, at the same energy). Furthermore, the ring current and thus light intensity had dropped by $\sim$10 % between the two PCBM measurement and the measurement of coverage 2. This naturally leads to the tentative conclusion that this could be a real effect.

The extent of beam-damage was investigated by measuring ten concurrent O 1s scans over an area of previously unmeasured sample. Scans 1, 5 and 10 are plotted out in Figure 6.25. This shows that unfortunately beam-damage did happen and it happened quickly. The spectra show an overall reduction in counts and a change in shape. In conclusion, the variations in oxygen are likely due to a combination of beam damage and some undetermined chemical effect - there is however no evidence of this in any other core levels.

6.5.2 Resonant photoemission

RPES maps are presented in Figure 6.26 for the underlying PCBM film, the four coverages in ascending order of P3HT thickness, and a P3HT multilayer for reference. The features match up with those explored for the separate molecules presented in Sections 6.3.3 and 6.4.3. Figure 6.27 shows two cases where RPES maps of monolayer and multilayer P3HT have been added to the map for multilayer PCBM. In the former, we see a map closely resembling coverage 1 and in the latter coverage 3.

We unfortunately see no definitive features showing electron movement from the P3HT's LUMO into PCBM's LUMO. This may have manifested itself, for example, as a reduction of the participator enhancement of P3HT's HOMO at the LUMO resonance if there were ultra-fast electron transfer into the PCBM from the core-excited P3HT. In the maps, this feature (at $BE \approx 3.5$ eV and $h\nu \approx 285.5$) does appear slightly weaker for coverages 3 and 4 than it does for the P3HT film. For the lower coverages, that region of the map is dominated by the PCBM HOMO-1 enhancement. Despite this potential observation, repeat measurements are certainly required to draw a definitive conclusion especially considering the confirmed beam damage of the molecule. We have not investigated the effect of this damage on the occupied or unoccupied states which could impact these observations.

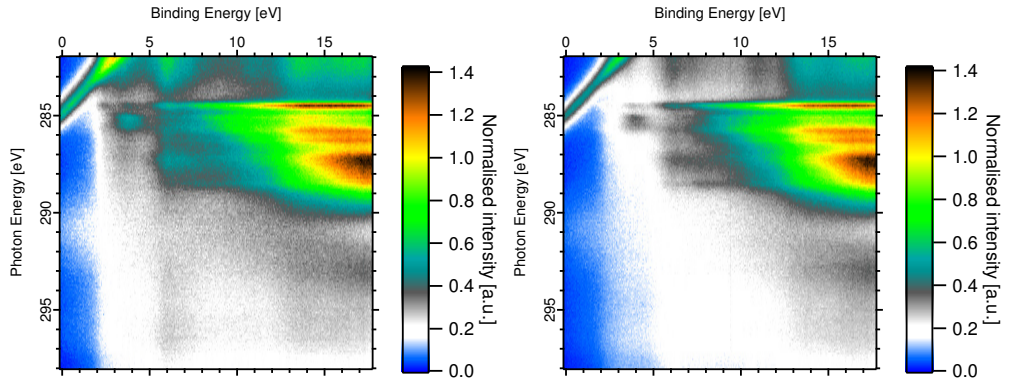


(a) Pure PCBM **(b)** Coverage 1

(c) Coverage 2 **(d)** Coverage 3

(e) Coverage 4 **(f)** Pure P3HT

Figure 6.26: C K-edge RPES maps of P3HT deposited on a thick multilayer of PCBM. (a) shows the pure PCBM film. (b-e) show increasing coverages of P3HT on the PCBM film. (f) shows a thick P3HT film for reference. Dashed (dark red) and solid (pink) lines show HOMO and LUMO positions for PCBM and P3HT respectively.



(a) PCBM multilayer + P3HT monolayer

(b) PCBM multilayer + P3HT multilayer

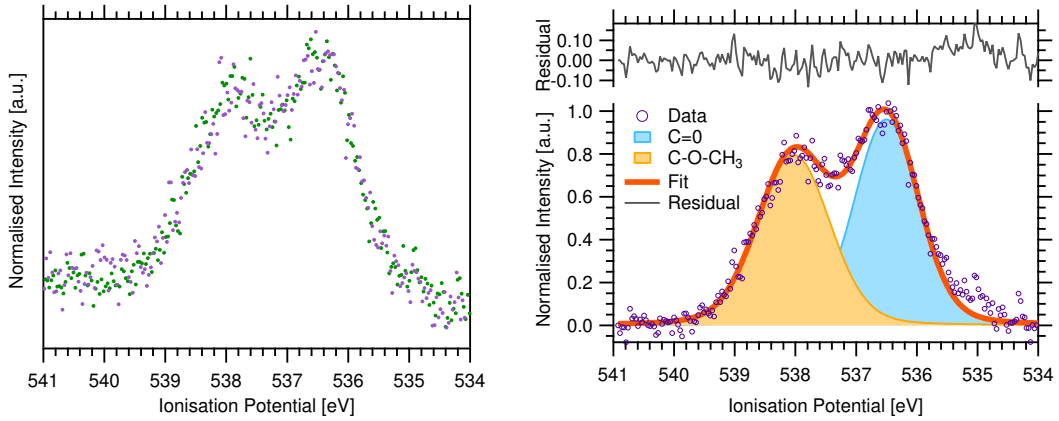
Figure 6.27: Artificially produced RPES maps of a PCBM-P3HT bi-layer for comparison to measured maps in Figure 6.26. Created by adding maps measured for the two individual films as indicated

6.6 Ionisation potential measurements

Using D1011, single layer, bi-layer and bulk heterojunction structures of PCBM and P3HT were made in-situ and measured on an ionisation potential scale. This reference to the vacuum level rather than the surface Fermi level is absolute and should not vary with steady state charging and other local effects due to film thickness. The method used to calibrate the energy scale is discussed in Chapter 2.4.1. All peak positions were measured by fitting Gaussian curves and edges (secondary electron cut-off, Fermi edge) were defined as the centre point of a linear fit. As before, photon energies were measured from the kinetic energy difference between core level spectra produced from first and second order light. All measurements presented below are multilayer deposits on Au(111) taken at normal emission.

6.6.1 Beam-damage

On D1011, where the brilliance of the light incident on the sample is much less than that at I311, beam damage was less of a concern. The complete set of spectra were measured twice in every position to ensure no damage occurred. Figure 6.28 shows two such O 1*s*, measured approximately 1 hour apart, for a PCBM multilayer along with peak fitting of the stoichiometric correct 1:1 areas for the two oxygen environments. There was no other evidence of beam damage in any spectra.



(a) Beam-damage check **(b)** Peak fitting

Figure 6.28: O 1*s* ionisation potential XPS spectra for a PCBM multilayer measured at D1011 with $h\nu = 650$ eV. (a) the same region measured many scans later to confirm the molecules are not damaged by the light. (b) Peak fitting of the spectra with relative areas of 1:1 between the two chemical environments.

6.6.2 Bi-layer

A multilayer of P3HT was deposited, annealed to 150 °C before depositing a monolayer of PCBM. The O 1*s* and S 2*p* are shown in Figures 6.30 and 6.30. The O 1*s* shows a small reduction of the methoxy peak (IP=538 eV) and a slight shift to higher ionisation potential when compared to a pure PCBM deposit. The sulphur is shown both before and after annealing as well as after the PCBM deposition. The peaks become sharper and shift to higher ionisation potential after heating by ∼0.3 eV and move back down, but retaining the sharpness of the peaks, after having a thin film of PCBM deposited on top.

6.6.3 Bulk heterojunctions

Here, the two stock solutions of P3HT and PCBM were mixed together in the ratios of 1:1, 5:1 and 20:1 (P3HT:PCBM) before deposition onto Au(111) by electrospray. The resulting O 1*s* spectra are shown in Figure 6.31 with the spectrum from the pure multilayer deposit for reference. There is again a definitive loss of the methoxy peak. However there does not seem to be a trend as to how much it is reduced and with the ratios of the two molecules. The carbonyl peak (IP=536.3 eV) shows minor energy shifts - the trend (if any) seems to be the more the methoxyl group is lost, the greater the increase in the carbonyl ionisation potential.

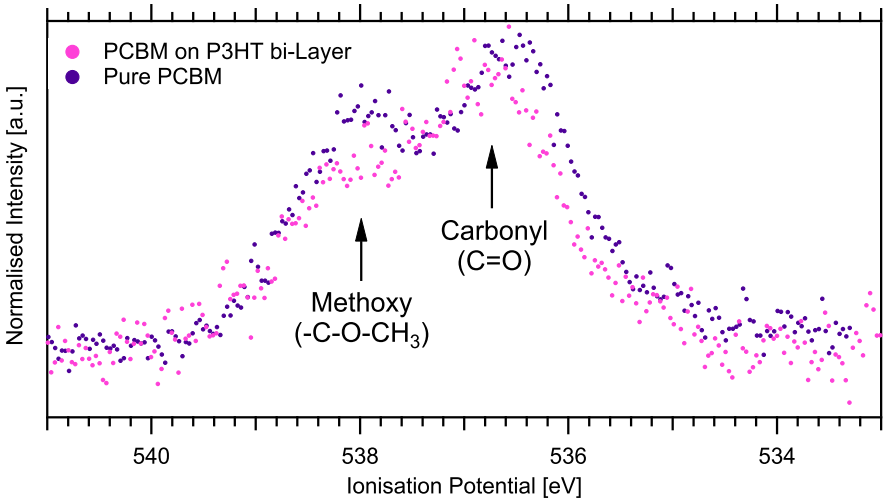


Figure 6.29: Ionisation potential XPS measurements of the O 1*s* core level for a bi-layer heterojunction of PCBM on P3HT. The spectra for pure PCBM is included for comparison.

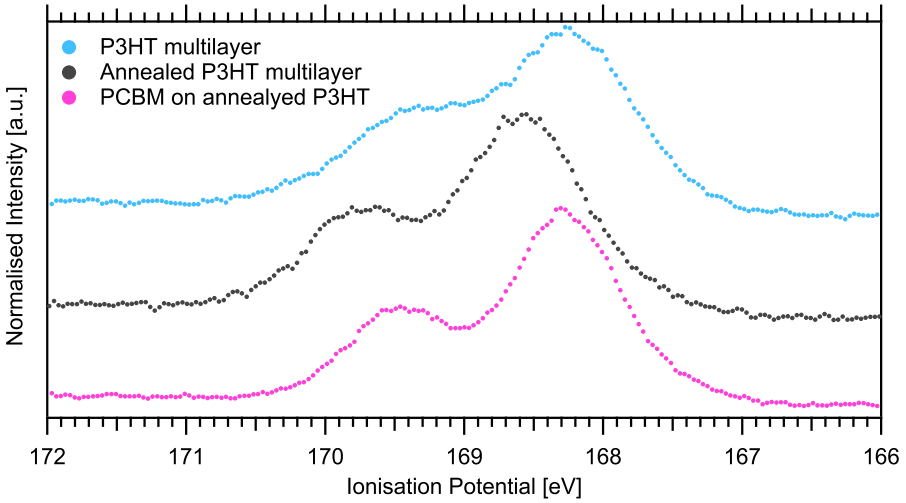


Figure 6.30: Ionisation potential XPS measurements of the S 2*p* core level for a thick film of P3HT before and after annealing and a bi-layer heterojunction of PCBM deposited on the annealed P3HT film.

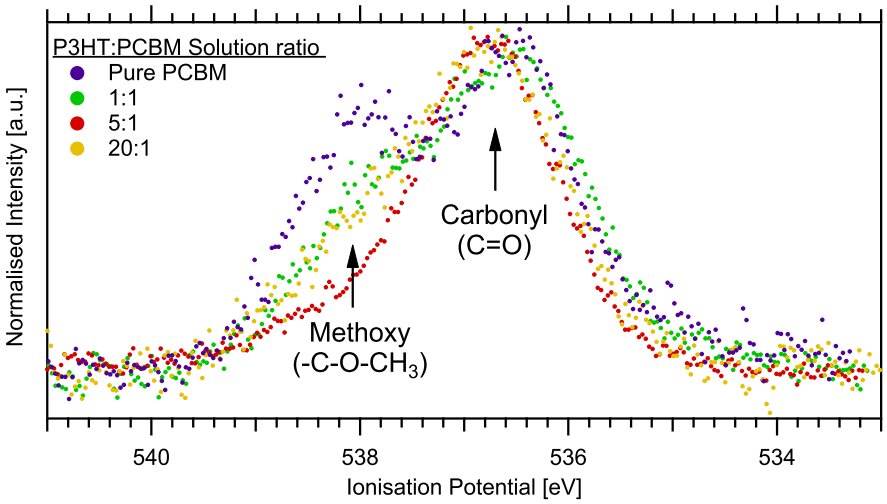


Figure 6.31: Ionisation potential XPS measurements of the O 1*s* core level for the three bulk heterojunctions measured. The spectra for pure PCBM is included for comparison.

The S 2*p* is presented in Figure 6.32 which again shows shifts in ionisation potential that again do not correlate with the ratio of solutions. The sharpness of the peaks does however tend to increase with the proportion of PCBM.

C 1*s* was also measured but not discussed here as it is was not possible to infer useful information as the PCBM and P3HT features were largely indistinguishable.

6.6.4 Summary of results and Kraut's method

All of the results discussed above, along with measurement of the valence band maxima for the individual molecule films, are included in the band diagram in Figure 6.33. This includes the positions of the carbonyl and methoxy O 1*s* peaks and the position of the S $2p_{3/2}$ peak for all deposits and the valence band maxima for the films of individual molecules. The error bars estimate the maximum uncertainty in the calibration of the spectra - typically $\sim$0.05 eV. The numbers for each band describe the centroid (obtained by peak fitting) for the case of core levels or the centre of a line of best fit through the leading edge of the valence band for the case of valence band maxima (VBM). The bold lines are predictions of the valence band maxima of the P3HT and PCBM components in the heterojunction calculated using the method of Kraut et al. [163] explained below.

For our application, Kraut's method is simplified as all the spectra are calibrated to the vacuum level, but the principle is very much the same. The technique relies on each species in the heterojunction having unique core levels - the position of which can act as a marker for the molecule. In our case, for PCBM we have

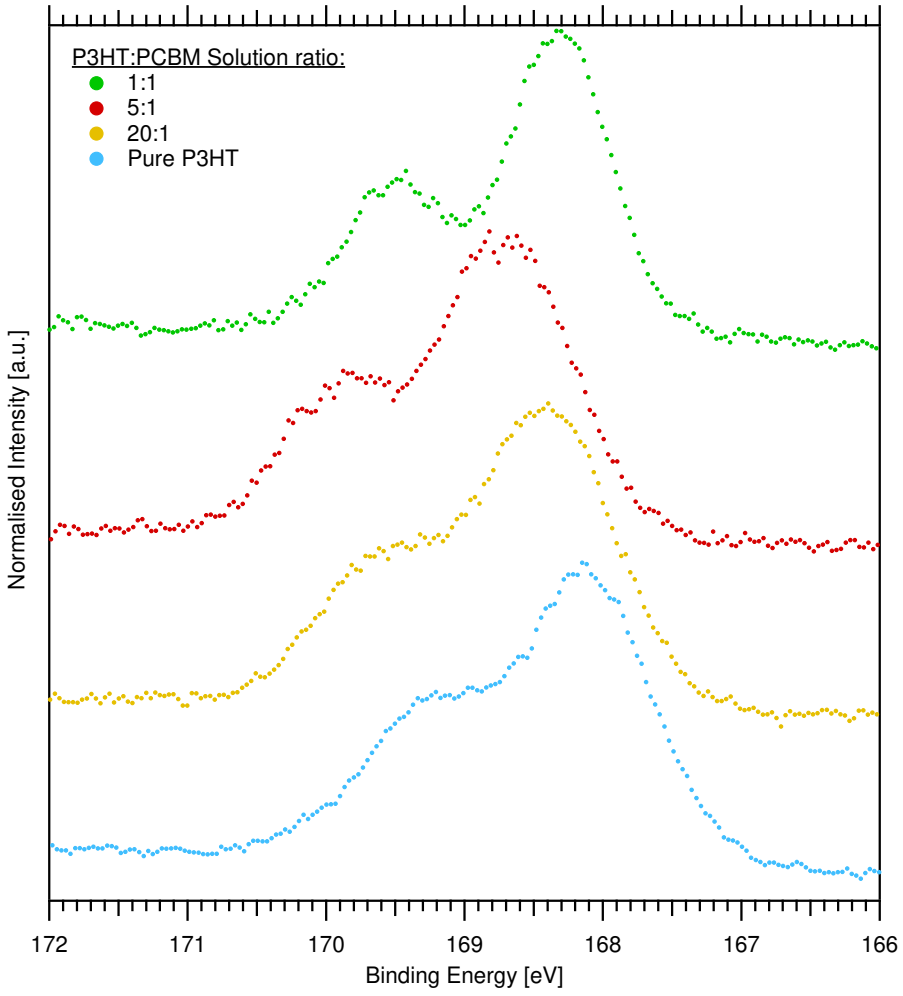


Figure 6.32: Ionisation potential XPS measurements of the S $2p$ core level for the three bulk heterojunctions measured. The spectra of pure P3HT is included for comparison.

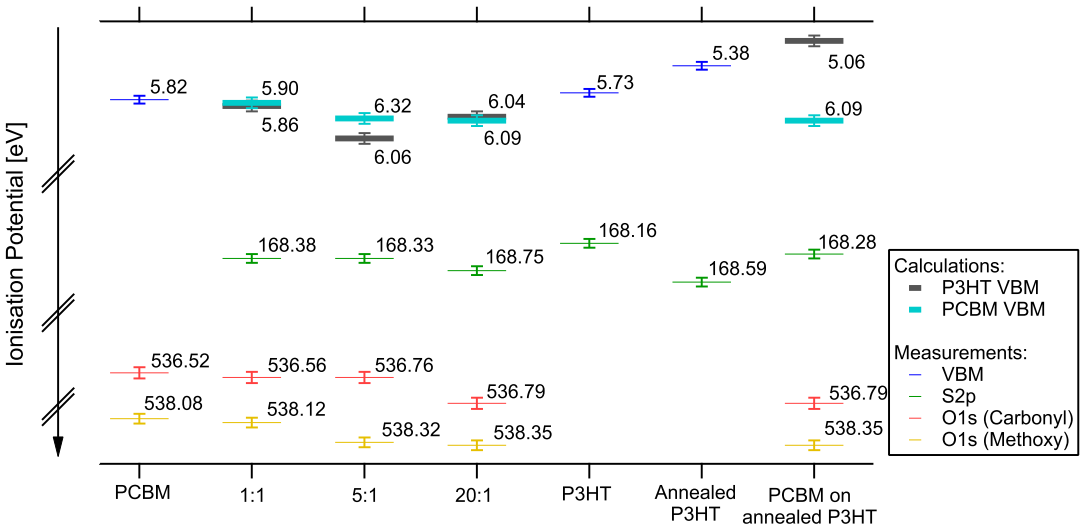


Figure 6.33: Band diagram summarising the acquired ionisation potential measurements

measured the positioning of the O 1s core levels and for P3HT the S $2p_{3/2}$ core level. In both cases the position of the valence band maximum were measured. For the heterojunctions, the position of the two core levels was measured, but the positioning of the valence band maximum for each molecule in the heterojunction was unknown. Our variation on Kraut's method is that when comparing the individual molecules to the heterojunction, the valence band maxima will have shifted in energy by the same amount as the core levels.

For example, for the 1:1 bulk heterojunction the measurements show the O 1s peak to be at 538.12 eV. For the pure molecule, the O 1s peak was at 538.08 eV so the heterojunction has caused a shift of 0.04 eV. The valence band maximum of PCBM was measured at 5.82 eV so Kraut's method implies that this should be shifted by the same amount as the core level, allowing us to calculate the position of the PCBM valence band maximum, in the 1:1 bulk heterojunction, to be at an ionisation potential of 5.86 eV.

It is difficult to draw any definitive conclusions from the ionisation potential measurements and calculations presented in Figure 6.33. It appears there is a trend of increasing ionisation potential for PCBM's methoxyl and carbonyl O 1s core levels with increasing amounts of P3HT in the bulk heterojunction. There is however no equivalent trend visible for P3HT's S 2p level. The valance band maximum (VBM) positions tell a similar story where the PCBM VBM does appear to shift to higher ionisation potential with increasing amounts of P3HT in the heterojunction, whereas the P3HT VBM does not present a trend. Annealing the

P3HT film appeared to shift both the S $2p$ and VBM to higher and lower ionisation potentials respectively. In the case of the bi-layer heterojucntion, consisting of a monolayer of PCBM on a multilayer of annealed P3HT, the PCBM features (both O $1s$ and VBM) appear at comparably high ionisation potentials to the bulk heterojunction with a high P3HT content. In both cases the all PCBM molecules are likely in contact with P3HT. In the bi-layer, the P3HT VBM appears at a much lower ionisation potential whereas the S $2p$ is at a comparable energy to the bulk heterojunction.

The summary is the data arguably contains trends in the energy of the PCBM features with increased levels of P3HT, but no corresponding trends in the P3HT data. We can offer no explanation as to why this is the case. It is possible this molecular system does not behave like a typical semiconductor heterojunction (what Kraut's method is typically intended for). We therefore think there is a good case for a simpler future study, where smaller, simpler molecules can be deposited using traditional methods without electrospray, to confirm the validity of the method.

6.7 Ex-situ samples

As mentioned, measurements were attempted on drop cast samples of the solutions measured on D1011 with the aim of comparing the results to the in-situ depositions at the synchrotron. The initial objective was to perform a quantitative analysis to see if the in-situ depositions yielded the same ratio of species as were originally in the solutions - i.e. to confirm the electrospray was not preferentially depositing one species over another. Unfortunately, the films produced were thin as the solutions were very dilute and, due to the ex-situ sample preparation, surface contamination meant this analysis was not possible - the results are therefore not presented here.

Another objective was to investigate whether the variation in the methoxy/carbonyl peak heights (present across all the synchrotron O $1s$ measurements) also occurred with solution process samples. This would help determine if it is a genuine interaction between the molecules in real devices, or whether it is an effect of the electrospray ionisation process. As previously discussed, the approach was to move to chlorobenzene as a solvent allowing us to produce more concentrated solutions that were deposited ex-situ by both electrospray and spin casting. Spin cast films of the two individual molecules were measured along with 3 ratios of 1:1, 1:0.8 and 2:1 blends of the P3HT:PCBM solutions. The three blends were also deposited by electrospray and measured.

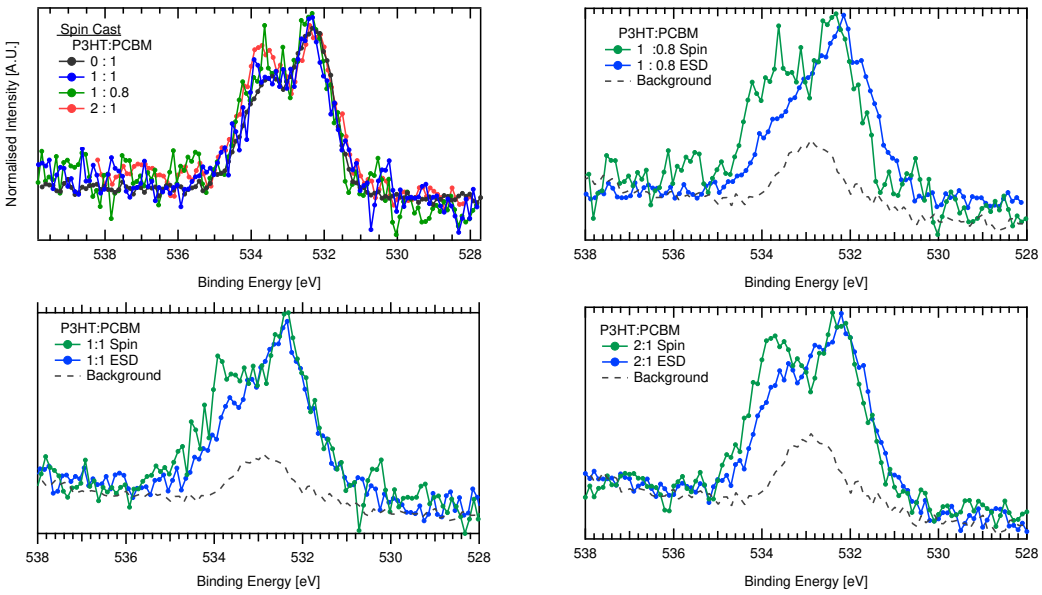


Figure 6.34: O 1*s* spectra measured for the ex-situ samples, prepared by spin coating and by electrospray. The first graph shows a comparison of all the spin case samples, including a pure PCBM film and the three bulk heterojunctions. The following three plots compare each spin cast sample with the electrospray deposit from the same solution. The dashed line shows the position of the surface oxygen contamination at an arbitrary intensity.

Figure 6.34 shows the O 1*s* data. The first sub-figure shows a comparison of the spin cast samples. All have the same shape (within the noise level). This is pretty convincing evidence that the loss of the methoxy group is not an effect that happens in solution. The following 3 figures compare the electrosprayed and spin-cast samples for each ratio. The dashed line shows the position of the background oxygen contamination, measured off a deposition spot on the gold surface, that may contribute slightly to the shape of the electrospray spectra (the intensity the peak is shown at is arbitrary). As with the synchrotron studies there appears to be a reduction in the methoxy peak.

Wide scans for the electrospray samples are included in Figure 6.35 and are normalised to the height of the C 1*s* peak. As can be seen in the inset zoomed in on the Au 4*f* peaks, the 0.8:1 is the thickest molecule coverage of the three meaning the surface oxygen contamination should be less dominant here. The corresponding O 1*s* in Figure 6.34 shows this is the sample with the most dramatic difference in methoxy and carbonyl peaks indicating that the surface contamination, if anything, masks this effect rather than enhancing it.

We therefore unfortunately have to conclude that this behaviour of the oxygen species is somehow linked to the electrospray process. This can be broken down

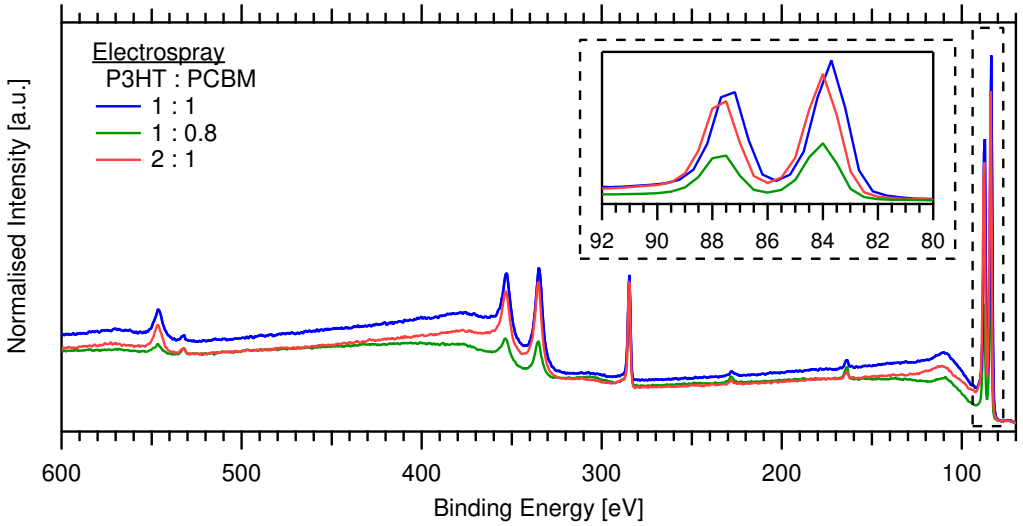


Figure 6.35: Wide scans for the three heterojunctions deposited by electrospray. All three spectra are normalised to the C 1s peak so allow comparison of the coverage by the strength of the gold signal (the Au 4f region is shown in the inset).

into either being caused by the electrospray ionisation process itself or from the solution processing required. The former is unlikely as we have not seen the electrospray instrument damage molecules previously. The alternative explanation is that it is happening in solution - in order to electrospray toluene or chlorobenzene solutions either methanol or acetone was added respectively. The possibility these additional solvents are causing a chemical change in the solution prior to deposition is something that needs further investigation.

6.8 Summary and conclusions

We have presented a wide range of photoelectron spectroscopy data of the PCBM/P3HT molecular system, where samples were prepared in-situ by electrospray deposition. These included films of the individual molecules, bi-layer structures and bulk heterojunctions on the Au(111) surface. Comparison of XPS data collected for monolayer and multilayer coverages of the individual molecules show no convincing evidence of chemical interactions with the surface. XAS has allowed us to map out the density of states for both the molecules in the core excited state.

RPES allowed us to investigate charge transfer between the molecules and the surface. For PCBM, given the LUMO lies below the underlying Au(111) Fermi edge, we were anticipating seeing ultra-fast bi-directional charge transfer in the

form of super-spectator and super-Auger decay. There was however no evidence of this. For comparison, C_{60}, which is known to exhibit these decay mechanisms on Au(111) when sublimed onto the surface [34], was deposited using electrospray and the superspectator/super-Auger lines were visible. This confirmed the lack of these features in the RPES was not a result of the preparation method. Unfortunately it remains unknown as to why PCBM does not decay from the core excited state via these channels. This is certainly worthy of future study - perhaps via PRES studies of related fullerenes. Azafullerenes, for example, contain one or more nitrogen atoms in place of carbon atoms breaking the symmetry (and thus electronic structure) of the molecule without adding a ligand. RPES was also measured for P3HT and a bilayer structure, which again showed no sign of charge transfer behaviour.

XPS of bi-layers and bulk heterojunctions alluded to an interaction between P3HT and the oxygen group terminated ligand of the PCBM where the carbonyl environment was repeatedly suppressed. This suppression was seemingly random based on the sample and does not, for example, correlate with the relative quantities of the two molecules. Measurement of spin cast films of the two molecules in chlorobenzene (rather than toluene) show this is not an interaction that happens between the molecules outside of the conditions of our electrospray experiments. Further investigation is needed into the effects of acetone/methanol on the chlorobenzene/toluene based solutions.

Chapter 7

Conclusions and future work

This thesis aims to investigate molecular photovoltaic devices via the measurement of model systems constructed on surfaces, in-situ, in UHV. It starts by presenting two instruments developed to aid the characterisation and future development of electrospray, followed by a series of three experiment demonstrating the unique capabilities of in-vacuum electrospray to make layered deposits and films consisting of blends of materials. This move towards fabricating these types of structure used in "real" devices is a natural progression from past work where we have used electrospray to study complex molecules, such as the N3 dye [6], on surfaces. The thesis then moves onto an investigation of the bonding and charge transfer interactions of of bi-isonicotinic acid, a common anchoring ligand for organometallic complexes that are designed to to titania, on Ag(111). This is achieved through a range of soft X-ray synchrotron based spectroscopies including X-ray photoelectron spectroscopy (XPS), Near Edge X-Ray Absorption Fine Structure (NEXAFS) spectroscopy and resonant photoemission spectroscopy (RPES). Finally, these same techniques are then applied to a more complex molecular system: heterostructure structures of phenyl-C61-butyric acid methyl ester (PCBM) and poly(3-hexylthiophene-2,5-diyl) (P3HT). These structures, which sit in the heart of organic photovoltaic devices, were deposited onto Au(111), in-situ, using electrospray deposition.

Chapter 3 provides an overview of two experimental approaches to aid in the development of electrospray. Firstly, an ultra-fast exposure imaging system was developed that produced stunning images of the electrospray ionisation process. Although the imaging system was a success, the electrospray set-up proved to be a limiting factor in the usefulness of the instrument due to repeatability problems - overcoming this would lead to many interesting studies helping understand the very complex physics of electrospray ionisation. Secondly, an image charge

detection instrument was built, potentially allowing real time monitoring of the charge and velocity distributions of ions in a high vacuum electrospray instrument. The preliminary measurements have been presented here and a final instrument been constructed facilitating future studies where charge/velocity information about the ions beam is valuable, for example investigating the geometry of the electrospray/vacuum interface where the free jet expansion process should determine the velocity of ions.

Chapter 4 shows, via time of flight secondary ion mass spectrometry, that electrospray can be used to make bi-layer structures with little mixing between the layers even when the two molecular films were deposited from the same solvent. Then, using two electrospray sources, we show that it is possible to simultaneously deposit two species on the surface that are not compatible with the same solvent. Finally, the conductive polymer blend, PEDOT:PSS, was deposited by drop casting and electrospray. We show that the electrospray preferentially deposits the PSS component. This behaviour is worthy of future study - it is critical to the long term application of electrospray as a deposition source for ever more complex molecular systems to understand any potential circumstances where the resulting deposit is not representative of the original solute.

Chapter 5, investigating the adsorption and charge transfer of bi-isonicotinic acid on Ag(111), provides evidence of an interaction between the carboxyl group on the molecule with the silver surface. The measured density of states, obtained via calibration of valance band XPS and NEXAFS onto a common energy axis, shows the positioning of the LUMO (lowest unoccupied molecular orbital) in the core excited state to be below the Fermi edge of the surface. This opens up the possibility of ultra-fast, bi-directional charge transfer between the molecule and surface which was probed via resonant photoemission. We see evidence of this via the super-spectator and super-Auger decay channels from the core excited state which dominate after photoexcitation into states below and above the Fermi edge respectively.

Chapter 6 starts by studying C_{60}, PCBM and P3HT on the Au(111) surface by electrospray. The measured density of states shows that the LUMO and PCBM does lie below the Fermi level, but unlike C_{60} does not show signs of super-spectator or super-Auger decay from the core excited state when probed using resonant photoemission. This study has shown that C_{60} does decay via these mechanisms, as we have previously demonstrated for sublimed monolayers [34], when prepared using electrospray. This leads to conclusion that the lack of the features for PCBM is real and it is unlikely an effect of the deposition method. Resonant photoemission of a bi-layer structure shows no conclusive evidence

of charge transfer between the two molecular films. XPS is used to probe the individual molecules, bi-layer heterojunctions and bulk heterojunctions deposited by electrospray. We see an interesting reduction of the methoxyl peak in the O $1s$ when the molecules are in contact in either type of heterojunction. Measurement of spin cast films shows this is not the case for films prepared directly from solution, creating suspicion the effect may be caused by the additional solvents required for electrospray. This should certainly be the focus of a future study. We finally, via measurement of the ionisation potential of core levels, try and predict the valance band maxima position of the PCBM and P3HT components in the heterojunction. This was unsuccessful, potentially due to the nature of the interfaces between the molecules. A potential follow-up investigation would be to attempt to prove the validity of this approach with a simpler molecular system.

Overall, this thesis has demonstrated the capabilities of electrospray deposition and furthered its usage to the complex chemical structures used in many molecular electronic devices, including organic photovoltaics, facilitating measurement using X-ray spectroscopies and other UHV techniques.

References

[1] European Comission, "Energy Roadmap 2050 - COM(2011) 885 final," 2011.

[2] UK Department of Energy and Climate Change, "UK Renewable Energy Roadmap," 2011.

[3] B. O'Regan and M. Grätzel, "A low-cost, high-efficiency solar cell based on dye-sensitized colloidal TiO_2 films," *Nature*, vol. 353, pp. 737–740, 10 1991.

[4] L. C. Mayor, J. Ben Taylor, G. Magnano, A. Rienzo, C. J. Satterley, J. N. O'Shea, and J. Schnadt, "Photoemission, resonant photoemission, and x-ray absorption of a Ru(II) complex adsorbed on rutile TiO_2(110) prepared by in situ electrospray deposition," *The Journal of chemical physics*, vol. 129, p. 114701, 9 2008.

[5] L. C. Mayor, A. Saywell, G. Magnano, C. J. Satterley, J. Schnadt, and J. N. O'Shea, "Adsorption of a Ru(II) dye complex on the Au(111) surface: Photoemission and scanning tunneling microscopy," *Journal of Chemical Physics*, vol. 130, no. 16, 2009.

[6] A. J. Gibson, R. H. Temperton, K. Handrup, M. Weston, L. C. Mayor, and J. N. O'Shea, "Charge transfer from an adsorbed ruthenium-based photosensitizer through an ultra-thin aluminium oxide layer and into a metallic substrate," *The Journal of chemical physics*, vol. 140, no. 23, p. 234708, 2014.

[7] L. Patthey, H. Rensmo, P. Persson, K. Westermark, L. Vayssieres, A. Stashans, A. Petersson, P. A. Bruhwiler, H. Siegbahn, S. Lunell, and N. Martensson, "Adsorption of bi-isonicotinic acid on rutile TiO_2(110)," *The Journal of Chemical Physics*, vol. 110, pp. 5913–5918, 3 1999.

[8] J. Schnadt, J. N. O'Shea, L. Patthey, J. Schiessling, J. Krempaský, M. Shi, N. Mårtensson, and P. a. Brühwiler, "Structural study of adsorption of isonicotinic acid and related molecules on rutile TiO_2(110) II: XPS," *Surface Science*, vol. 544, no. 1, pp. 74–86, 2003.

[9] J. Schnadt, A. Henningsson, M. P. Andersson, P. G. Karlsson, P. Uvdal, H. Siegbahn, P. A. Bruhwiler, and A. Sandell, "Adsorption and Charge-Transfer Study of Bi-isonicotinic Acid on In Situ-Grown Anatase TiO_2 Nanoparticles," *The Journal of Physical Chemistry B*, vol. 108, pp. 3114–3122, 3 2004.

[10] J. Schnadt, P. A. Bruhwiler, L. Patthey, J. N. O'Shea, S. Södergren, M. Odelius, R. Ahuja, O. Karis, M. Bässler, P. Persson, H. Siegbahn, S. Lunell, and N. Mårtensson, "Experimental evidence for sub-3-fs charge transfer from an aromatic adsorbate to a semiconductor," *Nature*, vol. 418, pp. 620–623, 8 2002.

[11] J. B. Taylor, L. C. Mayor, J. C. Swarbrick, J. N. O'Shea, C. Isvoranu, and J. Schnadt, "Adsorption and charge transfer dynamics of bi-isonicotinic acid on Au(111)," *The Journal of chemical physics*, vol. 127, p. 134707, 10 2007.

[12] C. E. McCusker and F. N. Castellano, "Design of a Long-Lifetime, Earth-Abundant, Aqueous Compatible Cu(I) Photosensitizer Using Cooperative Steric Effects," *Inorganic Chemistry*, vol. 52, pp. 8114–8120, 7 2013.

[13] Y. Liu, P. Persson, V. Sundstrom, and K. Warnmark, "Fe N -Heterocyclic Carbene Complexes as Promising Photosensitizers," *Accounts of Chemical Research*, vol. 49, pp. 1477–1485, 8 2016.

[14] P. Chábera, Y. Liu, O. Prakash, E. Thyrhaug, A. E. Nahhas, A. Honarfar, S. Essén, L. A. Fredin, T. C. B. Harlang, K. S. Kjær, K. Handrup, F. Ericson, H. Tatsuno, K. Morgan, J. Schnadt, L. Häggström, T. Ericsson, A. Sobkowiak, S. Lidin, P. Huang, S. Styring, J. Uhlig, J. Bendix, R. Lomoth, V. Sundström, P. Persson, and K. Wärnmark, "A low-spin Fe(III) complex with 100-ps ligand-to-metal charge transfer photoluminescence," *Nature*, vol. 543, pp. 695–699, 3 2017.

[15] S. A. Haque, E. Palomares, H. M. Upadhyaya, L. Otley, R. J. Potter, A. B. Holmes, and J. R. Durrant, "Flexible dye sensitised nanocrystalline semiconductor solar cells," *Chemical Communications*, no. 24, p. 3008, 2003.

[16] P. Wang, B. Wenger, R. Humphry-Baker, J.-E. Moser, J. Teuscher, W. Kantlehner, J. Mezger, E. V. Stoyanov, S. M. Zakeeruddin, and M. Grätzel, "Charge Separation and Efficient Light Energy Conversion in Sensitized Mesoscopic Solar Cells Based on Binary Ionic Liquids," *Journal of the American Chemical Society*, vol. 127, pp. 6850–6856, 5 2005.

[17] J. J. Concepcion, J. W. Jurss, M. R. Norris, Z. Chen, J. L. Templeton, and T. J. Meyer, "Catalytic Water Oxidation by Single-Site Ruthenium Catalysts," *Inorganic Chemistry*, vol. 49, pp. 1277–1279, 2 2010.

[18] M. Hiramoto, H. Fujiwara, and M. Yokoyama, "Three-layered organic solar cell with a photoactive interlayer of codeposited pigments," *Applied Physics Letters*, vol. 58, pp. 1062–1064, 3 1991.

[19] G. Yu, J. Gao, J. C. Hummelen, F. Wudl, and A. J. Heeger, "Polymer Photovoltaic Cells: Enhanced Efficiencies via a Network of Internal Donor-Acceptor Heterojunctions," *Science*, vol. 270, pp. 1789–1791, 12 1995.

[20] C. W. Tang, "Two-layer organic photovoltaic cell," *Applied Physics Letters*, vol. 48, no. 2, pp. 183–185, 1986.

[21] H. Hoppe and N. S. Sariciftci, "Organic solar cells: An overview," *Journal of Materials Research*, vol. 19, no. 07, pp. 1924–1945, 2004.

[22] B. P. Lyons, N. Clarke, and C. Groves, "The relative importance of domain size, domain purity and domain interfaces to the performance of bulk-heterojunction organic photovoltaics," *Energy & Environmental Science*, vol. 5, no. 6, p. 7657, 2012.

[23] G. J. Hedley, A. Ruseckas, and I. D. W. Samuel, "Light Harvesting for Organic Photovoltaics," *Chemical Reviews*, p. acs.chemrev.6b00215, 2016.

[24] E. Peeters, P. A. van Hal, J. Knol, C. J. Brabec, N. S. Sariciftci, J. C. Hummelen, and R. A. J. Janssen, "Synthesis, Photophysical Properties, and Photovoltaic Devices of Oligo(p-phenylene vinylene)-fullerene Dyads," *The Journal of Physical Chemistry B*, vol. 104, pp. 10174–10190, 11 2000.

[25] B. Kippelen and J.-L. Brédas, "Organic photovoltaics," *Energy & Environmental Science*, vol. 2, no. 3, p. 251, 2009.

[26] G. Dennler, M. C. Scharber, and C. J. Brabec, "Polymer-fullerene bulk-heterojunction solar cells," *Advanced Materials*, vol. 21, no. 13, pp. 1323–1338, 2009.

[27] C.-Z. Li, H.-L. Yip, and A. K.-Y. Jen, "Functional fullerenes for organic photovoltaics," *Journal of Materials Chemistry*, vol. 22, no. 10, p. 4161, 2012.

[28] N. Kaur, M. Singh, D. Pathak, T. Wagner, and J. M. Nunzi, "Organic materials for photovoltaic applications: Review and mechanism," *Synthetic Metals*, vol. 190, pp. 20–26, 2014.

[29] M. T. Dang, L. Hirsch, and G. Wantz, "P3HT:PCBM, Best Seller in Polymer Photovoltaic Research," *Advanced Materials*, vol. 23, pp. 3597–3602, 8 2011.

[30] R. Steim, F. R. Kogler, and C. J. Brabec, "Interface materials for organic solar cells," *Journal of Materials Chemistry*, vol. 20, no. 13, pp. 2499–2512, 2010.

[31] K. Walzer, B. Maennig, M. Pfeiffer, and K. Leo, "Highly Efficient Organic Devices Based on Electrically Doped Transport Layers," *Chemical Reviews*, vol. 107, pp. 1233–1271, 4 2007.

[32] F. Deschler, D. Riedel, B. Ecker, E. von Hauff, E. Da Como, and R. C. I. MacKenzie, "Increasing organic solar cell efficiency with polymer interlayers," *Physical Chemistry Chemical Physics*, vol. 15, no. 3, pp. 764–769, 2013.

[33] A. J. Britton, A. Rienzo, J. N. O'Shea, and K. Schulte, "Charge transfer between the Au(111) surface and adsorbed C_{60}: Resonant photoemission and new core-hole decay channels," *The Journal of chemical physics*, vol. 133, p. 094705, 9 2010.

[34] A. Gibson, R. Temperton, K. Handrup, and J. O'Shea, "Resonant core spectroscopies of the charge transfer interactions between C_{60} and the surfaces of Au(111), Ag(111), Cu(111) and Pt(111)," *Surface Science*, vol. 657, 2017.

[35] J. Taylor, L. Mayor, J. Swarbrick, J. N. O'Shea, and J. Schnadt, "Charge-Transfer Dynamics at Model Metal-Organic Solar Cell Surfaces," *Journal of Physical Chemistry C*, vol. 111, pp. 16646–16655, 11 2007.

[36] A. J. Britton, M. Weston, J. B. Taylor, A. Rienzo, L. C. Mayor, and J. N. O'Shea, "Charge transfer interactions of a Ru(II) dye complex and related ligand molecules adsorbed on Au(111)," *The Journal of chemical physics*, vol. 135, p. 164702, 10 2011.

[37] M. Weston, T. J. Reade, A. J. Britton, K. Handrup, N. R. Champness, and J. N. O'Shea, "A single centre water splitting dye complex adsorbed on rutile TiO_2(110): photoemission, x-ray absorption, and optical spectroscopy," *The Journal of chemical physics*, vol. 135, p. 114703, 10 2011.

[38] M. Weston, K. Handrup, T. J. Reade, N. R. Champness, and J. N. O'Shea, "Experimental observation of sub-femtosecond charge transfer in a model water splitting dye-sensitized solar cell," *The Journal of chemical physics*, vol. 137, p. 224706, 12 2012.

[39] M. Weston, A. J. Britton, and J. N. O'Shea, "Charge transfer dynamics of model charge transfer centers of a multicenter water splitting dye complex on rutile TiO_2(110)," *The Journal of chemical physics*, vol. 134, p. 054705, 2 2011.

[40] P. A. Bruhwiler, O. Karis, and N. Martensson, "Charge-transfer dynamics studied using resonant core spectroscopies," *Reviews of Modern Physics*, vol. 74, pp. 703–740, 7 2002.

[41] F. Lord Rayleigh, "On the equilibrium of liquid conducting masses charged with electricity," *Philosophical Magazine Series 5*, vol. 14, no. 87, pp. 184–186, 1882.

[42] J. Zeleny, "The electrical discharge from liquid points, and a hydrostatic method of measuring the electric intensity at their surfaces," *Physical Review*, vol. 3, no. 2, pp. 69–91, 1914.

[43] J. Zeleny, "On the conditions of instability of electrified drops, with applications to the electrical discharge from liquid points," *Proceedings of the Cambridge Philosophical Society*, vol. 18, pp. 71–83, 5 1915.

[44] J. Zeleny, "Instability of electrified liquid surfaces," *Physical Review*, vol. 10, no. 1, pp. 1–6, 1917.

[45] M. Dole, "Molecular Beams of Macroions," *The Journal of Chemical Physics*, vol. 49, no. 5, p. 2240, 1968.

[46] J. Fenn, M. Mann, C. Meng, S. Wong, and C. Whitehouse, "Electrospray ionization for mass spectrometry of large biomolecules," *Science*, vol. 246, pp. 64–71, 10 1989.

[47] P. Kebarle and U. H. Verkerk, "Electrospray: from ions in solution to ions in the gas phase, what we know now," *Mass spectrometry reviews*, vol. 28, no. 6, pp. 898–917, 2009.

[48] M. Wilm, "Principles of electrospray ionization," *Molecular & cellular proteomics*, vol. 10, p. M111.009407, 7 2011.

[49] G. Taylor, "Disintegration of Water Drops in an Electric Field," *Proceedings of the Royal Society A: Mathematical, Physical and Engineering Sciences*, vol. 280, no. 1382, p. 383, 1964.

[50] J. N. Smith, "Droplet Evaporation and Discharge Dynamics," pp. 9957–9967, 2000.

[51] L. Konermann, E. Ahadi, A. D. Rodriguez, and S. Vahidi, "Unraveling the Mechanism of Electrospray Ionization," *Analytical Chemistry*, vol. 85, pp. 2–9, 1 2013.

[52] J. V. Iribarne, "On the evaporation of small ions from charged droplets," *The Journal of Chemical Physics*, vol. 64, no. 6, p. 2287, 1976.

[53] B. A. Thomson and J. V. Iribarne, "Field induced ion evaporation from liquid surfaces at atmospheric pressure," *The Journal of Chemical Physics*, vol. 71, no. 11, p. 4451, 1979.

[54] L. L. Mack, P. Kralik, A. Rheude, and M. Dole, "Molecular Beams of Macroions. II," *The Journal of Chemical Physics*, vol. 52, pp. 4977–4986, 5 1970.

[55] L. Konermann, A. D. Rodriguez, and J. Liu, "On the formation of highly charged gaseous ions from unfolded proteins by electrospray ionization," *Analytical Chemistry*, vol. 84, no. 15, pp. 6798–6804, 2012.

[56] J. B. Fenn, M. Mann, C. K. Meng, S. F. Wong, and C. M. Whitehouse, "Electrospray ionization-principles and practice," *Mass Spectrometry Reviews*, vol. 9, pp. 37–70, 1 1990.

[57] S. Nguyen and J. B. Fenn, "Gas-phase ions of solute species from charged droplets of solutions," *Proceedings of the National Academy of Sciences of the United States of America*, vol. 104, pp. 1111–7, 1 2007.

[58] S. J. Gaskell, "Electrospray: Principles and Practice," *Journal of Mass Spectrometry*, vol. 32, pp. 677–688, 7 1997.

[59] M. Pauly, M. Sroka, J. Reiss, G. Rinke, a. Albarghash, R. Vogelgesang, H. Hahne, B. Kuster, J. Sesterhenn, K. Kern, and S. Rauschenbach, "A hydrodynamically optimized nano-electrospray ionization source and vacuum interface," *The Analyst*, vol. 139, pp. 1856–67, 3 2014.

[60] H. Pauly, *Atom, Molecule, and Cluster Beams I: Basic Theory, Production and Detection of Thermal Energy Beams*. Springer Series on Atomic, Optical, and Plasma Physics, Springer Berlin Heidelberg, 2012.

[61] M. Barr, K. M. O'Donnell, A. Fahy, W. Allison, and P. C. Dastoor, "A desktop supersonic free-jet beam source for a scanning helium microscope (SHeM)," *Measurement Science and Technology*, vol. 23, p. 105901, 10 2012.

[62] S. Rauschenbach, F. L. Stadler, E. Lunedei, N. Malinowski, S. Koltsov, G. Costantini, and K. Kern, "Electrospray ion beam deposition of clusters and biomolecules," *Small (Weinheim an der Bergstrasse, Germany)*, vol. 2, pp. 540–7, 4 2006.

[63] O. Hadjar, P. Wang, J. H. Futrell, Y. Dessiaterik, Z. Zhu, J. P. Cowin, M. J. Iedema, and J. Laskin, "Design and performance of an instrument for soft landing of biomolecular ions on surfaces," *Analytical Chemistry*, vol. 79, no. 17, pp. 6566–6574, 2007.

[64] C. Hamann, R. Woltmann, I.-P. Hong, N. Hauptmann, S. Karan, and R. Berndt, "Ultrahigh vacuum deposition of organic molecules by electrospray ionization," *Review of Scientific Instruments*, vol. 82, no. 3, p. 033903, 2011.

[65] R. T. Kelly, A. V. Tolmachev, J. S. Page, K. Tang, and R. D. Smith, "The ion funnel: theory, implementations, and applications," *Mass spectrometry reviews*, vol. 29, no. 2, pp. 294–312, 2010.

[66] M. Szilagyi, *Electron and Ion Optics*. Springer Science & Business Media, 2012.

[67] P. E. Miller and M. B. Denton, "The quadrupole mass filter: Basic operating concepts," *Journal of Chemical Education*, vol. 63, p. 617, 7 1986.

[68] C. S. Kley, C. Dette, G. Rinke, C. E. Patrick, J. Čechal, S. J. Jung, M. Baur, M. Dürr, S. Rauschenbach, F. Giustino, S. Stepanow, and K. Kern, "Atomic-Scale Observation of Multiconformational Binding and Energy Level Alignment of Ruthenium-Based Photosensitizers on TiO_2 Anatase," *Nano Letters*, vol. 14, pp. 563–569, 2 2014.

[69] M. Weston, T. J. Reade, K. Handrup, N. R. Champness, and J. N. O'Shea, "Adsorption of Dipyrrin-Based Dye Complexes on a Rutile $TiO_2(110)$ Surface," *The Journal of Physical Chemistry C*, vol. 116, pp. 18184–18192, 8 2012.

[70] A. Rienzo, L. C. Mayor, G. Magnano, C. J. Satterley, E. Ataman, J. Schnadt, K. Schulte, and J. N. O'Shea, "X-ray absorption and photoemission spectroscopy of zinc protoporphyrin adsorbed on rutile $TiO_2(110)$ prepared by in situ electrospray deposition," *The Journal of Chemical Physics*, vol. 132, p. 084703, 2 2010.

[71] C. J. Satterley, L. M. a. Perdigão, A. Saywell, G. Magnano, A. Rienzo, L. C. Mayor, V. R. Dhanak, P. H. Beton, and J. N. O'Shea, "Electrospray deposition of fullerenes in ultra-high vacuum: in situ scanning tunneling microscopy and photoemission spectroscopy," *Nanotechnology*, vol. 18, p. 455304, 11 2007.

[72] J. N. O'Shea, J. B. Taylor, J. C. Swarbrick, G. Magnano, L. C. Mayor, and K. Schulte, "Electrospray deposition of carbon nanotubes in vacuum," *Nanotechnology*, vol. 18, p. 035707, 1 2007.

[73] M. C. O'Sullivan, J. K. Sprafke, D. V. Kondratuk, C. Rinfray, T. D. W. Claridge, A. Saywell, M. O. Blunt, J. N. O'Shea, P. H. Beton, M. Malfois, and H. L. Anderson, "Vernier templating and synthesis of a 12-porphyrin nano-ring," *Nature*, vol. 469, pp. 72–75, 1 2011.

[74] D. V. Kondratuk, L. M. A. Perdigao, M. C. O'Sullivan, S. Svatek, G. Smith, J. N. O'Shea, P. H. Beton, and H. L. Anderson, "Two vernier-templated routes to a 24-porphyrin nanoring," *Angewandte Chemie - International Edition*, vol. 51, no. 27, pp. 6696–6699, 2012.

[75] M. B. Wieland, L. M. A. Perdigão, D. V. Kondratuk, J. N. O'Shea, H. L. Anderson, and P. H. Beton, "Height dependent molecular trapping in stacked cyclic porphyrin nanorings," *Chemical Communications*, vol. 50, no. 55, p. 7332, 2014.

[76] D. V. Kondratuk, J. K. Sprafke, M. C. O'Sullivan, L. M. A. Perdigao, A. Saywell, M. Malfois, J. N. O'Shea, P. H. Beton, A. L. Thompson, and H. L. Anderson, "Vernier-Templated Synthesis, Crystal Structure, and Supramolecular Chemistry of a 12-Porphyrin Nanoring," *Chemistry - A European Journal*, vol. 20, pp. 12826–12834, 9 2014.

[77] D. V. Kondratuk, L. M. A. Perdigão, A. M. S. Esmail, J. N. O'Shea, P. H. Beton, and H. L. Anderson, "Supramolecular nesting of cyclic polymers," *Nature Chemistry*, vol. 7, no. 4, pp. 317–322, 2015.

[78] A. Saywell, A. J. Britton, N. Taleb, M. del Carmen Giménez-López, N. R. Champness, P. H. Beton, and J. N. O'Shea, "Single molecule magnets on a gold surface: in situ electrospray deposition, x-ray absorption and photoemission," *Nanotechnology*, vol. 22, p. 075704, 2 2011.

[79] S. Kahle, Z. Deng, N. Malinowski, C. Tonnoir, A. Forment-Aliaga, N. Thontasen, G. Rinke, D. Le, V. Turkowski, T. S. Rahman, S. Rauschenbach, M. Ternes, and K. Kern, "The quantum magnetism of individual manganese-12-acetate molecular magnets anchored at surfaces," *Nano Letters*, vol. 12, no. 1, pp. 518–521, 2012.

[80] K. Handrup, V. J. Richards, M. Weston, N. R. Champness, and J. N. O'Shea, "Single molecule magnets with protective ligand shells on gold and titanium dioxide surfaces: In situ electrospray deposition and x-ray absorption spectroscopy," *The Journal of Chemical Physics*, vol. 139, p. 154708, 10 2013.

[81] P. Erler, P. Schmitt, N. Barth, A. Irmler, S. Bouvron, T. Huhn, U. Groth, F. Pauly, L. Gragnaniello, and M. Fonin, "Highly Ordered Surface Self-Assembly of Fe_4 Single Molecule Magnets," *Nano Letters*, vol. 15, pp. 4546–4552, 7 2015.

[82] J. C. Swarbrick, J. B. Taylor, and J. N. O'Shea, "Electrospray deposition in vacuum," *Applied Surface Science*, vol. 252, pp. 5622–5626, 5 2006.

[83] A. Saywell, J. K. Sprafke, L. J. Esdaile, A. J. Britton, A. Rienzo, H. L. Anderson, J. N. O'Shea, and P. H. Beton, "Conformation and Packing of Porphyrin Polymer Chains Deposited Using Electrospray on a Gold Surface," *Angewandte Chemie International Edition*, vol. 49, pp. 9136–9139, 11 2010.

[84] S. Park, Y. Lee, and Y. Yi, "Vacuum-integrated electrospray deposition for highly reliable polymer thin film," *Review of Scientific Instruments*, vol. 83, p. 105106, 10 2012.

[85] J. Laskin, P. Wang, and O. Hadjar, "Soft-landing of peptide ions onto self-assembled monolayer surfaces: an overview," *Physical chemistry chemical physics*, vol. 10, no. 8, pp. 1079–90, 2008.

[86] Z. Deng, N. Thontasen, N. Malinowski, G. Rinke, L. Harnau, S. Rauschenbach, and K. Kern, "A close look at proteins: Submolecular resolution of two- and three-dimensionally folded cytochrome c at surfaces," *Nano Letters*, vol. 12, no. 5, pp. 2452–2458, 2012.

[87] J.-N. Longchamp, S. Rauschenbach, S. Abb, C. Escher, T. Latychevskaia, K. Kern, and H.-W. Fink, "Imaging proteins at the truly single-molecule level," vol. 114, no. 7, pp. 1–6, 2015.

[88] G. Rinke, S. Rauschenbach, L. Harnau, A. Albarghash, M. Pauly, and K. Kern, "Active conformation control of unfolded proteins by hyperthermal collision with a metal surface," *Nano Letters*, vol. 14, no. 10, pp. 5609–5615, 2014.

[89] E. Fornari, C. J. Roberts, R. H. Temperton, and J. N. O'Shea, "Electrospray deposition in vacuum as method to create functionally active protein immobilization on polymeric substrates," *Journal of colloid and interface science*, vol. 453, pp. 252–9, 2015.

[90] N. Hauptmann, C. Hamann, H. Tang, and R. Berndt, "Soft-landing electrospray deposition of the ruthenium dye N3 on Au(111)," *Journal of Physical Chemistry C*, vol. 117, no. 19, pp. 9734–9738, 2013.

[91] G. Dubey, R. Urcuyo, S. Abb, G. Rinke, M. Burghard, S. Rauschenbach, and K. Kern, "Chemical modification of graphene via hyperthermal molecular reaction," *Journal of the American Chemical Society*, vol. 136, no. 39, pp. 13482–13485, 2014.

[92] R. H. Temperton, J. N. O'Shea, and D. J. Scurr, "On the suitability of high vacuum electrospray deposition for the fabrication of molecular electronic devices," *Chemical Physics Letters*, vol. 682, pp. 15–19, 8 2017.

[93] R. Temperton, A. Gibson, K. Handrup, and J. O'Shea, "Adsorption and charge transfer interactions of bi-isonicotinic acid on Ag(111)," *Journal of Chemical Physics*, vol. 147, no. 5, 2017.

[94] A. Einstein, "On a Heuristic Point of View Concerning the Production and Transformation of Light," in *The Collected Papers of Albert Einstein, Volume 2 (English): The Swiss Years: Writings, 1900-1909. (English translation supplement)*, p. 149, 1905.

[95] S. D. Kevan, "Design of a high-resolution angle-resolving electron energy analyzer," *Review of Scientific Instruments*, vol. 54, no. 11, pp. 1441–1445, 1983.

[96] M. Dogan, M. Ulu, G. G. Gennarakis, and T. J. M. Zouros, "Experimental energy resolution of a paracentric hemispherical deflector analyzer for different entry positions and bias," *Review of Scientific Instruments*, vol. 84, no. 4, 2013.

[97] P. Guttmann and C. Bittencourt, "Overview of nanoscale NEXAFS performed with soft X-ray microscopes," *Beilstein Journal of Nanotechnology*, vol. 6, pp. 595–604, 2 2015.

[98] M. P. Seah and W. A. Dench, "Quantitative electron spectroscopy of surfaces: A standard data base for electron inelastic mean free paths in solids," *Surface and Interface Analysis*, vol. 1, pp. 2–11, 2 1979.

[99] J. N. O'Shea, *Photoelectron spectroscopy of Alkali-doped Ni(110)-O surfaces*. PhD thesis, University of Cardiff, 1998.

[100] C. Fadley, "Basic Concepts of X-Ray Photoelectron Spectroscopy," in *Electron Spectroscopy: Theory, Techniques, and Applications* (C. R. Brundle and A. D. Baker, eds.), vol. 2, pp. 62–66, Published by Academic Press Inc (1978), 1978.

[101] M. Ruiz-Osés, D. G. De Oteyza, I. Fernández-Torrente, N. Gonzalez-Lakunza, P. M. Schmidt-Weber, T. Kampen, K. Hom, A. Gourdon, A. Arnau, and J. E. Ortega, "Non-covalent interactions in supramolecular assemblies investigated with electron spectroscopies," *ChemPhysChem*, vol. 10, no. 6, pp. 896–900, 2009.

[102] I. E. Brumboiu, L. Ericsson, R. Hansson, E. Moons, O. Eriksson, and B. Brena, "The influence of oxygen adsorption on the NEXAFS and core-level XPS spectra of the C_{60} derivative PCBM," *The Journal of Chemical Physics*, vol. 142, p. 054306, 2 2015.

[103] M. H. Richter, D. Friedrich, and D. Schmei?er, "Valence and Conduction Band States of PCBM as Probed by Photoelectron Spectroscopy at Resonant Excitation," *BioNanoScience*, vol. 2, pp. 59–65, 3 2012.

[104] J. Stöhr, *NEXAFS Spectroscopy*. Springer Series in Surface Sciences, Springer Berlin Heidelberg, 2013.

[105] P. Woodruff, *Modern Techniques of Surface Science*. Cambridge University Press, 2016.

[106] F. R. Elder, A. M. Gurewitsch, R. V. Langmuir, and H. C. Pollock, "Radiation from Electrons in a Synchrotron," *Physical Review*, vol. 71, pp. 829–830, 6 1947.

[107] W. Gelletly, "Daresbury Laboratory," *Measurement Science and Technology*, vol. 3, pp. 239–242, 2 1992.

[108] J. P. Long, B. S. Itchkawitz, and M. N. Kabler, "Photoelectron spectroscopy of laser-excited surfaces by synchrotron radiation," *Journal of the Optical Society of America B*, vol. 13, no. 1, p. 201, 1996.

[109] P. Willmott, *An introduction of synchrotron radiation: Techniques and applications*. 2011.

[110] P. Elleaume, "Insertion devices for the new generation of synchrotron sources: A review," *Review of Scientific Instruments*, vol. 63, no. 1, pp. 321–326, 1992.

[111] A. Maxwell, P. Brühwiler, D. Arvanitis, J. Hasselström, and N. Mårtensson, "C 1s ionisation potential and energy referencing for solid C_{60} films on metal surfaces," *Chemical Physics Letters*, vol. 260, no. 1-2, pp. 71–77, 1996.

[112] D. A. Shirley, "High-Resolution X-Ray Photoemission Spectrum of the Valence Bands of Gold," *Physical Review B*, vol. 5, pp. 4709–4714, 6 1972.

[113] S. Tougaard, "Quantitative analysis of the inelastic background in surface electron spectroscopy," *Surface and Interface Analysis*, vol. 11, pp. 453–472, 6 1988.

[114] M. Schmid, H. P. Steinrück, and J. M. Gottfried, "A new asymmetric Pseudo-Voigt function for more efficient fitting of XPS lines," *Surface and Interface Analysis*, vol. 46, no. 8, pp. 505–511, 2014.

[115] J. M. Hollas, *Modern Spectroscopy*. Wiley, 2004.

[116] J. C. Riviere and S. Myhra, *Handbook of Surface and Interface Analysis: Methods for Problem-Solving, Second Edition*. CRC Press, 2009.

[117] G. Henderson, D. Neuville, and R. Downs, *Spectroscopic Methods in Mineralogy and Material Sciences*. Reviews in Mineralogy & Geochemistry, De Gruyter, 2014.

[118] J. J. Yeh and I. Lindau, "Atomic subshell photoionization cross sections and asymmetry parameters:," *Atomic Data and Nuclear Data Tables*, vol. 32, no. 1, pp. 1–155, 1985.

[119] D. E. Parry, "Atomic calculation of photoionization cross-sections and asymmetry parameters," *Rapid Communications in Mass Spectrometry*, vol. 8, no. 7, p. 579, 1994.

[120] J. Söderström, N. Mårtensson, O. Travnikova, M. Patanen, C. Miron, L. J. Sæthre, K. J. Børve, J. J. Rehr, J. J. Kas, F. D. Vila, T. D. Thomas, and S. Svensson, "Nonstoichiometric intensities in core photoelectron spectroscopy," *Physical Review Letters*, vol. 108, no. 19, pp. 1–4, 2012.

[121] D. F. Mitchell, K. B. Clark, J. A. Bardwell, W. N. Lennard, G. R. Massoumi, and I. V. Mitchell, "Film thickness measurements of SiO2 by XPS," *Surface and Interface Analysis*, vol. 21, pp. 44–50, 1 1994.

[122] J. E. Martin, A. A. Herzing, W. Yan, X.-q. Li, B. E. Koel, C. J. Kiely, and W.-x. Zhang, "Determination of the Oxide Layer Thickness in Core-Shell Zerovalent Iron Nanoparticles," *Langmuir*, vol. 24, pp. 4329–4334, 4 2008.

[123] J. Schnadt, J. O'Shea, L. Patthey, J. Krempaský, N. Mårtensson, and P. Brühwiler, "Alignment of valence photoemission, x-ray absorption, and substrate density of states for an adsorbate on a semiconductor surface," *Physical Review B*, vol. 67, no. 23, p. 235420, 2003.

[124] R. Nyholm, J. N. Andersen, U. Johansson, B. N. Jensen, and I. Lindau, "Beamline I311 at MAX-LAB: A VUV/soft X-ray undulator beamline for high resolution electron spectroscopy," *Nuclear Instruments and Methods in Physics Research, Section A: Accelerators, Spectrometers, Detectors and Associated Equipment*, vol. 467-468, pp. 520–524, 2001.

[125] K. A. Selanger, J. Falnes, and T. Sikkeland, "Fluorescence lifetime studies of Rhodamine 6G in methanol," *The Journal of Physical Chemistry*, vol. 81, pp. 1960–1963, 10 1977.

[126] S. R. Mabbett, L. W. Zilch, J. T. Maze, J. W. Smith, and M. F. Jarrold, "Spectrometry : Application to Weighing Electrosprayed Droplets," vol. 79, no. 22, pp. 8431–8439, 2007.

[127] S. D. Fuerstenau and W. H. Benner, "Molecular weight determination of megadalton DNA electrospray ions using charge detection time-of-flight mass spectrometry," *Rapid communications in mass spectrometry : RCM*, vol. 9, pp. 1528–38, 1 1995.

[128] J. W. Smith, E. E. Siegel, J. T. Maze, and M. F. Jarrold, "Image Charge Detection Mass Spectrometry : Pushing the Envelope with Sensitivity and Accuracy," pp. 950–956, 2011.

[129] J. T. Maze, T. C. Jones, and M. F. Jarrold, "Negative droplets from positive electrospray," *The journal of physical chemistry. A*, vol. 110, pp. 12607–12, 11 2006.

[130] T. Fukuda, K. Takagi, T. Asano, Z. Honda, N. Kamata, K. Ueno, H. Shirai, J. Ju, Y. Yamagata, and Y. Tajima, "Bulk heterojunction organic photovoltaic cell fabricated by the electrospray deposition method using mixed organic solvent," *Physica Status Solidi-Rapid Research Letters*, vol. 5, no. 7, pp. 229–231, 2011.

[131] S. Rauschenbach, R. Vogelgesang, N. Malinowski, J. W. Gerlach, M. Benyoucef, G. Costantini, Z. Deng, N. Thontasen, and K. Kern, "Electrospray ion beam deposition: soft-landing and fragmentation of functional molecules at solid surfaces," *ACS nano*, vol. 3, pp. 2901–10, 10 2009.

[132] J. Bailey and J. S. Sharp, "Thin film polymer photonics: Spin cast distributed Bragg reflectors and chirped polymer structures," *European Physical Journal E*, vol. 33, no. 1, pp. 41–49, 2010.

[133] C. E. Mora-Huertas, H. Fessi, and A. Elaissari, "Polymer-based nanocapsules for drug delivery," *International Journal of Pharmaceutics*, vol. 385, no. 1-2, pp. 113–142, 2010.

[134] J. Bailey, R. Havelund, A. G. Shard, I. S. Gilmore, M. R. Alexander, J. S. Sharp, and D. J. Scurr, "3D ToF-SIMS imaging of polymer multilayer films using argon cluster sputter depth profiling," *ACS Applied Materials and Interfaces*, vol. 7, no. 4, pp. 2654–2659, 2015.

[135] K. Schulze, C. Uhrich, R. Schüppel, K. Leo, M. Pfeiffer, E. Brier, E. Reinold, and P. Bäuerle, "Efficient vacuum-deposited organic solar cells based on a new low-bandgap oligothiophene and fullerene C_{60}," *Advanced Materials*, vol. 18, no. 21, pp. 2872–2875, 2006.

[136] M. Grätzel, "Dye-sensitized solar cells," *Journal of Photochemistry and Photobiology C: Photochemistry Reviews*, vol. 4, no. 2, pp. 145–153, 2003.

[137] J. N. O'Shea, J. B. Taylor, L. C. Mayor, J. C. Swarbrick, and J. Schnadt, "Molecular damage in bi-isonicotinic acid adsorbed on rutile $TiO_2(110)$," *Surface Science*, vol. 602, pp. 1693–1698, 5 2008.

[138] C. Enkvist, S. Lunell, B. Sjögren, S. Svensson, P. A. Brühwiler, A. Nilsson, A. J. Maxwell, and N. Mårtensson, "C1s shakeup spectrum of C_{60}: Global charge-transfer satellites and their relation to the x-ray threshold singularities in macroscopic systems," *Physical Review B*, vol. 48, pp. 14629–14637, 11 1993.

[139] I. Cebula, H. Lu, M. Zharnikov, and M. Buck, "Monolayers of trimesic and isophthalic acid on Cu and Ag: the influence of coordination strength on adsorption geometry," *Chemical Science*, vol. 4, no. 12, p. 4455, 2013.

[140] H. Li, B. Xu, D. Evans, and J. E. Reutt-Robey, "Isonicotinic acid molecular films on Ag(111): I. XPS and STM studies of orientational domains," *Journal of Physical Chemistry C*, vol. 111, no. 5, pp. 2102–2106, 2007.

[141] J. O'Shea, Y. Luo, J. Schnadt, L. Patthey, H. Hillesheimer, J. Krempasky, D. Nordlund, M. Nagasono, P. Brühwiler, and N. Mårtensson, "Hydrogen-bond induced surface core-level shift in pyridine carboxylic acids," *Surface Science*, vol. 486, pp. 157–166, 7 2001.

[142] O. Adak, G. Kladnik, G. Bavdek, A. Cossaro, A. Morgante, D. Cvetko, and L. Venkataraman, "Ultrafast Bidirectional Charge Transport and Electron Decoherence at Molecule/Surface Interfaces: A Comparison of Gold, Graphene, and Graphene Nanoribbon Surfaces," *Nano Letters*, vol. 15, pp. 8316–8321, 12 2015.

[143] J. Maibach, E. Mankel, T. Mayer, and W. Jaegermann, "The band energy diagram of PCBM–DH6T bulk heterojunction solar cells: synchrotron-induced photoelectron spectroscopy on solution processed DH6T:PCBM blends and in situ prepared PCBM/DH6T interfaces," *Journal of Materials Chemistry C*, vol. 1, no. March, p. 7635, 2013.

[144] J. Kettle, H. Waters, Z. Ding, M. Horie, and G. Smith, "Chemical changes in PCPDTBT:PCBM solar cells using XPS and TOF-SIMS and use of inverted device structure for improving lifetime performance," *Solar Energy Materials and Solar Cells*, vol. 141, pp. 139–147, 10 2015.

[145] H. Wei, L. Scudiero, and H. Eilers, "Infrared and photoelectron spectroscopy study of vapor phase deposited poly (3-hexylthiophene)," *Applied Surface Science*, vol. 255, pp. 8593–8597, 7 2009.

[146] K. Kanai, T. Miyazaki, H. Suzuki, M. Inaba, Y. Ouchi, and K. Seki, "Effect of annealing on the electronic structure of poly(3-hexylthiophene) thin film," *Phys. Chem. Chem. Phys.*, vol. 12, no. 1, pp. 273–282, 2010.

[147] M. Manceau, J. Gaume, A. Rivaton, J.-L. Gardette, G. Monier, and L. Bideux, "Further insights into the photodegradation of poly(3-hexylthiophene) by means of X-ray photoelectron spectroscopy," *Thin Solid Films*, vol. 518, pp. 7113–7118, 9 2010.

[148] H. O. Seo, M.-G. Jeong, K.-D. Kim, D. H. Kim, Y. D. Kim, and D. C. Lim, "Studies of degradation behaviors of poly(3-hexylthiophene) layers by X-ray photoelectron spectroscopy," *Surface and Interface Analysis*, vol. 46, pp. 544–549, 8 2014.

[149] A. Tada, Y. Geng, Q. Wei, K. Hashimoto, and K. Tajima, "Tailoring organic heterojunction interfaces in bilayer polymer photovoltaic devices," *Nature Materials*, vol. 10, pp. 450–455, 6 2011.

[150] Q.-D. Yang, H.-W. Li, Y. Cheng, Z. Guan, T. Liu, T.-W. Ng, C.-S. Lee, and S.-W. Tsang, "Probing the Energy Level Alignment and the Correlation with Open-Circuit Voltage in Solution-Processed Polymeric Bulk Heterojunction Photovoltaic Devices," *ACS Applied Materials & Interfaces*, vol. 8, pp. 7283–7290, 3 2016.

[151] J. S. Kim, W. S. Chung, K. Kim, D. Y. Kim, K. J. Paeng, S. M. Jo, and S. Y. Jang, "Performance optimization of polymer solar cells using electrostatically sprayed photoactive layers," *Advanced Functional Materials*, vol. 20, no. 20, pp. 3538–3546, 2010.

[152] S. E. Park, J. Y. Hwang, K. Kim, B. Jung, W. Kim, and J. Hwang, "Spray deposition of electrohydrodynamically atomized polymer mixture for active layer fabrication in organic photovoltaics," *Solar Energy Materials and Solar Cells*, vol. 95, no. 1, pp. 352–356, 2011.

[153] M. Ali, M. Abbas, S. K. Shah, R. Tuerhong, A. Generosi, B. Paci, L. Hirsch, and R. Gunnella, "Realization of solution processed multi-layer bulk heterojunction organic solar cells by electro-spray deposition," *Organic Electronics: physics, materials, applications*, vol. 13, no. 10, pp. 2130–2137, 2012.

[154] Y. Kim, G. Kim, J. Lee, and K. Lee, "Morphology controlled bulk-heterojunction layers of fully electro-spray coated organic solar cells," *Solar Energy Materials and Solar Cells*, vol. 105, pp. 272–279, 2012.

[155] X. Y. Zhao, X. Wang, S. L. Lim, D. Qi, R. Wang, Z. Gao, B. Mi, Z. K. Chen, W. Huang, and W. Deng, "Enhancement of the performance of organic solar cells by electrospray deposition with optimal solvent system," *Solar Energy Materials and Solar Cells*, vol. 121, pp. 119–125, 2014.

[156] Y. Yi, J. E. Lyon, M. M. Beerbom, and R. Schlaf, "Characterization of indium tin oxide surfaces and interfaces using low intensity x-ray photoemission spectroscopy," *Journal of Applied Physics*, vol. 100, p. 093719, 11 2006.

[157] M. P. Seah, I. S. Gilmore, and G. Beamson, "XPS: binding energy calibration of electron spectrometers 5 - Re-evaluation of the reference energies," *Surface and Interface Analysis*, vol. 26, pp. 642–649, 8 1998.

[158] C.-Q. Sheng, P. Wang, Y. Shen, Y.-J. Li, W.-H. Zhang, F.-Q. Xu, J.-F. Zhu, G.-Q. Lai, and H.-N. Li, "Electronic structure of PCBM," *Chinese Physics B*, vol. 21, no. 1, p. 017102, 2012.

[159] P. A. Brühwiler, A. J. Maxwell, C. Puglia, A. Nilsson, S. Andersson, and N. Mårtensson, "Pi* and sigma* excitons in C 1s absorptino of graphite," *Physical Review Letters*, vol. 74, pp. 614–617, 1 1995.

[160] L. Kjeldgaard, T. Kaambre, J. Schiessling, I. Marenne, J. N. O'Shea, J. Schnadt, C. J. Glover, M. Nagasono, D. Nordlund, M. G. Garnier, L. Qian, J.-E. Rubensson, P. Rudolf, N. Martensson, J. Nordgren, and P. A. Bruhwiler, "Intramolecular vibronic dynamics in molecular solids: C_{60}," *Physical Review B*, vol. 72, p. 205414, 11 2005.

[161] T. Schwieger, X. Liu, H. Peisert, B. Adolphi, N. Kiriy, and M. Knupfer, "Electronic properties of interfaces between different sexithiophenes and gold," *Journal of Applied Physics*, vol. 97, p. 123712, 6 2005.

[162] H. Hintz, H.-J. Egelhaaf, H. Peisert, and T. Chasse, "Photo-oxidation and ozonization of poly(3-hexylthiophene) thin films as studied by UV/VIS and photoelectron spectroscopy," *Polymer Degradation and Stability*, vol. 95, pp. 818–825, 5 2010.

[163] E. A. Kraut, R. W. Grant, J. R. Waldrop, and S. P. Kowalczyk, "Precise Determination of the Valence-Band Edge in X-Ray Photoemission Spectra: Application to Measurement of Semiconductor Interface Potentials," *Physical Review Letters*, vol. 44, pp. 1620–1623, 6 1980.

Appendix A

Electrospray compatible solvents and solutes

A.1 Solvent information

The following is a list of solvents we have successful used to deposit molecules from using electrospray:

- Methanol - general go to solvent for electrospray deposition
- Acetone - second favourite choice
- IPA
- Toluene (with ∼10 % methanol added)
- Chlorobenzene (with ∼10 % methanol or acetone added)
- Ethylene glycol (it does spray but reducing the viscosity by mixing with methanol was useful)
- Citrate buffer
- Phosphate buffer (with ∼10 % methanol added)
- Water (difficult - can mix with methanol if required)
- Acetonitrile

A.2 Solute information

The following is a list of some of the molecules we have successfully deposited in vacuum using electrospray along with the solvent used:

- Fluorescein dye (methanol)
- Rhodamine 6G and 6B (methanol)
- N3 dye (methanol)
- SQ2 dye (methanol)
- RK1 dye (methanol)
- Gold nanoparticles (citrate buffer)
- PEO(methanol)
- PEG (water with methanol added)
- PLGA (acetone)
- PVP (methanol)
- Polystrene (toluene with water added)
- Fibronectin (Phosphate buffer with methanol added)
- C_{60} (Toluene with methanol added)
- PCBM (Toluene/Chlorobenzene with Methanol/Acetone added)
- P3HT (Toluene/Chlorobenzene with Methanol/Acetone added)
- PEDOT:PSS (water with methanol added)
- Iron centred organometallic dye complexes (Acetonitrile)